Thesis Title

Assessing crop water requirements and irrigation scheduling at different spatial scales in Mediterranean orchards using models, proximal and remotely sensed data

MATTEO IPPOLITO

Tutors

Ch.mo. Prof. Giuseppe Provenzano†
Dipartimento Scienze Agrarie, Alimentari e Forestali (SAAF), Università degli Studi di Palermo, Viale delle Scienze, Bld. 4, 90128, Palermo, Italy

Ch.mo. Prof. Vincenzo Bagarello
Dipartimento Scienze Agrarie, Alimentari e Forestali (SAAF), Università degli Studi di Palermo, Viale delle Scienze, Bld. 4, 90128, Palermo, Italy

Co-Tutors

Ing. Mario Minacapilli
Dipartimento di Ingegneria, Università degli Studi di Palermo, Viale delle Scienze, Bld. 8, 90128, Palermo, Italy

Ch.mo. Prof. Giuseppe Ciraolo
Dipartimento di Ingegneria, Università deli Studi di Palermo, Viale delle Scienze, Bld. 8, 90128, Palermo, Italy

External reviewers

Prof. Leonor Rodriguez Sinobas
Escuela Técnica Superior de Ingeniería Agronómica, Alimentaria y Biosistemas Departamento de Ingeniería Agroforestal, Universitat Politècnica de Madrid, Calle Ramiro de Maeztu, 28040 Madrid, España

Prof. Manzano Juarez, Juan
Escuela Técnica Superior de Ingeniería Agronómica y del Medio Natural Departamento de Ingeniería Hidráulica y Medio Ambiente, Universitat Politècnica de València, Camino de Vera, s/n, 46022 Valencia, España

Università degli Studi di Palermo

AREA QUALITÀ, PROGRAMMAZIONE E SUPPORTO STRATEGICO
SETTORE STRATEGIA PER LA RICERCA
U. O. DOTTORATI

Dottorato di ricerca in Scienze Agrarie Alimentari e Forestali
Dipartimento di Scienze Agrarie Alimentari e Forestali
Settore Scientifico Disciplinare AGR/08

Assessing crop water requirements and irrigation scheduling at different spatial scale in Mediterranean orchards using models, proximal and remotely sensed data

Il Dottorando
Ing. Matteo Ippolito

Il Coordinatore
Ch.mo Prof. Vincenzo Bagarello

Tutors
Ch.mo Prof. Giuseppe Provenzano †

Co-Tutors
Ing. Mario Minacapilli

Ch.mo Prof. Vincenzo Bagarello

Ch.mo. Prof. Giuseppe Ciraolo

CICLO – XXXV
A.A. 2022-2023

Ippolito, M.

"Assessing crop water requirements and irrigation scheduling at different spatial scales in Mediterranean orchards using models, proximal and remotely sensed data"
Università degli Studi di Palermo, Dipartimento di Scienze Agrarie Alimentari e Forestali (SAAF)
Dottorato di Ricerca in Scienze Agrarie Alimentari e Forestali – XXXV Ciclo (2019-2023)

Cover picture: Giuseppe Antonio Provenzano (2006) – Storie di un massacro "Immagini e racconti da Burundi per non dimenticare"

In memory of my tutor
Ch.mo. Prof. Giuseppe Antonio Provenzano

Acknowledgments

This thesis was developed in the framework of the INtegrated Computer modeling and monitoring for Irrigation Planning in ITaly (INCIPIT) project conducted at the Department of Agricultural, Food and Forestry Sciences of the University of Palermo (Italy).

I want to thank my co-tutors Ing. Mario Minacapilli and Prof. Giuseppe Ciraolo for their valuable advice, support and practical help throughout the entire PhD especially during the final period.

Many thanks to the Spanish reviewers Prof. Leonor Rodriguez Sinobas and Prof. Manzano Juarez, Juan for accurate revision and useful suggestions that certainly have been improved the quality of the final result.

A huge thank you to my colleagues/friends Dario De Caro and Vincenzo Alagna, because during my PhD I had the good fortune to get to know not only two professionals but two very special people, with whom I spent beautiful but also difficult moments together. I hope we can continue to work together in the world of research.

Last but not least, I would thank my family, Laura and her family for their constant love encouragement especially in the most difficult moments. nothing I would have done without them.

Finally, I would like to dedicate this thesis to my tutor, Prof. Giuseppe Antonio Provenzano, who has been a scientific and life point of reference for me. For these reasons, his memory will live in me forever.

Abstract:

Accurate estimations of crop water requirements are necessary to improve water use in agriculture and to optimize the use of available freshwater resource. To this aim, the Agro-Hydrological models represent useful tools to quantify the crop actual evapotranspiration.

To define the upper boundary condition of the Agro-Hydrological models it is essential to assess the atmospheric water demand, expressed as crop reference evapotranspiration, *ETo*. In literature several methods, different in terms of input data requirement and climate variables combinations, have been developed to estimate *ETo*. Among these methods it is commonly used the well-known FAO56 Penman-Monteith (FAO56-PM) thermodynamic approach. Implementing this method requires access to climate data usually measured by ground weather stations. Unfortunately, these instruments are not always available, in this case recent climate reanalysis databases are useful solution to overcome this limitation.

Direct measurements of actual evapotranspiration, ET_a, are important to validate the results of the model's application. These measurements, especially for large scale use, can be time consuming and economically expensive. Moreover, improper installation of the sensors or incorrect calibrations could cause outliers in time series or compromise the continuity of the data time series. Recently Machine Learning (ML) algorithm have been developed to predict and fill the gaps in time series of ET_a.

The joint use of Agro-Hydrological models with proximity and remotely sensed data is one of the possible ways to accurately estimate crop water requirements. The remote observations of the land surface represent a reliable strategy to identify the spatial distribution of vegetation biophysical parameters, such as, crop coefficient K_c under actual field conditions.

The general objective of the research was to assess the crop water requirements in two typical crops (citrus and olive) of the Mediterranean region, using FAO56 Agro-Hydrological model based on functional relationships K_c(VIs) between crop coefficient, K_c, and Vegetation Indices (VIs) calibrate using in situ measurements and VIs obtained by multispectral remotely sensed data. Moreover, it was evaluated the reliability of the reanalysis climate variables provided by ERA5-Land database to assess *ETo* in Sicily (Italy).

The performance of the ERA5-Land reanalysis weather data to estimate *ETo*, was assessed considering 39 ground weather station distributed in

Sicily region. The *ETo* values estimated on the basis of climate variables from ERA5-L database encourage the use of reanalysis database to assess *ETo*. In general, the results were in agreement with those obtained from ground measurement, with average Root Mean Square Error (RMSE) equal to 0.73 mm d^{-1} and corresponding Mean Bias Error (MBE) equal to -0.36 mm d^{-1}.

The research activities were carried out in two experimental fields.

The first experimental field is a citrus orchard located near the Villabate town whereas the second one was the irrigation district 1/A, managed by "Consorzio di Bonifica della Sicilia" ex "Consorzio di Bonifica Agrigento 3", Castelvetrano, Sicily (Italy), characterized mainly by olives orchards.

The time series of ET_a, acquired by the Eddy Covariance (EC) tower installed in the citrus experimental field was processed using the Gaussian Process Regression (GPR) algorithm in order to fill the gaps. The performances were evaluated in terms of Nash Sutcliffe Efficiency (NSE) coefficient and RMSE. The values of NSE ranging between 0.74 and 0.88, whereas the RMSE values lower or equal to 0.55 mm d^{-1} confirm the suitability of the GPR model, to predict time ET_a series.

FAO56 Agro-Hydrological model was applied for the irrigation seasons 2018, 2019 and 2020 (Villabate) and for the irrigation seasons 2018 and 2019 (Castelvetrano). For each study areas, using VIs obtained from Sentinel-2 Multi Spectral Images (MSI) level 2A, a K_c(VIs) relationship was developed and then implemented in the model. The model was used to estimates spatial and temporal variability of the actual evapotranspiration, soil water content (SWC), in the root zone, crop coefficient and stress coefficient, as well as, to irrigation scheduling.

For the citrus orchard a non-linear K_c(VIs) relationship was identified after assuming that the sum of two VIs, such as Normalized Difference Vegetation Index (NDVI), and Normalized Difference Water Index (NDWI), is suitable to represent the spatio-temporal dynamics of the investigated environment. The application of the FAO56 Agro-Hydrological model indicated that the estimated ET_a was characterized by RMSE, and MBE, of 0.48 and -0.13 mm d^{-1} respectively, while the estimated SWC, were characterized by RMSE = 0.01 cm^3 cm^{-3} and the absence of bias, then confirming that the suggested procedure can produce highly accurate results in terms of dynamics of SWC and ET_a under the investigated field conditions.

In the Castelvetrano irrigation district 1/A, a linear K_c(VI) relationship was identified following the Allen and Pereira (A&P) procedure which was based on the height of the canopy and the fraction of vegetation cover, the last was estimated by the NDVI. The differences between simulated and measured seasonal values was encouraging for the 2018, with value equal to 3%, while for the 2019 it was equal to 17%. These results highlight that the proposed model, with further improvements, and more accurate information such as the effective depth of root zone and the real volumes delivered by the hydrants, can be a useful tool for supporting the decision in the management of the irrigation demands in the irrigation district.

Keywords: Remote sensing, FAO56 Agro-Hydrological model, crop coefficient, actual evapotranspiration, irrigation scheduling, reanalysis database, machine learning algorithm.

Contents:

List of Figures XVII

List of Tables XXV

List of symbols XXIX

List of acronyms XXXV

Chapter 1: Introduction 1

1.1 Water uses in agriculture: General overview 1

1.2 Strategies for sustainable water use in agriculture 3

1.3 Models and remotely sensed data to assess crop water requirements 4

1.4 Thesis objectives 7

1.5 Thesis Structure 8

Chapter 2: Theoretical background 13

2.1 Crop water requirement assessment in agriculture: General overview 13

2.2 Soil-Plant-Atmosphere (SPA) system: Energy and Soil water balance approach 15

2.3 Water exchange modelling in the SPA system: FAO56 Agro-hydrological model 17

2.3.1 Crop coefficient estimation based on spectral data 21

2.3.2 Estimation of basal crop coefficient based on fraction ground cover and crop height 26

2.4 Monitoring of SPA system components 27

2.4.1 Techniques for soil water status monitoring 27

2.4.2 Techniques for plant water status monitoring 30

2.4.3 Techniques for crop reference evapotranspiration monitoring 38

2.4.4 Techniques for potential and actual evapotranspiration monitoring 40

2.4.5 Machine learning algorithms to assess actual evapotranspiration 42

Chapter 3: Materials 47

3.1 Climate data 47

3.2 Experimental field – Villabate 49

3.3 Irrigation District 1A – Castelvetrano 52

3.3.1 Experimental field – Castelvetrano 57

Chapter 4: Methods 61

4.1 FAO56 Penman-Monteith equation to estimate crop reference evapotranspiration 61

4.2 Estimation of actual evapotranspiration based on Gaussian Process Regression (GPR) algorithm 62

4.3 Experimental field – Villabate 65

4.3.1 Evaluation of vegetation indices 65

4.3.2 Calibration of crop coefficient - vegetation indices functional relationship to estimate actual evapotranspiration by means FAO56 Agro-Hydrological model 65

4.4 Irrigation district 1A – Castelvetrano 67

4.4.1 Estimation of basal crop coefficient based on fractional cover and canopy height 67

4.4.2 Implementing the spatially distributed FAO56 model 70

4.5 Statistical indicators for model validation 72

Chapter 5: Results and Discussion 77

5.1 Comparison between ground weather stations (SIAS) and ERA5-Land reanalysis climate variables 77

5.1.1 Crop reference evapotranspiration, estimated from SIAS and ERA5-Land climate variables 81

5.1.2 Sensitivity analysis of FAO56-Penman-Monteith equation 83

5.2 Estimation of actual evapotranspiration by means machine learning algorithm 85

5.2.1 Input variables: In situ data 85
5.2.2 Input variables: remotely sensed data 90
5.2.3 Predicted actual evapotranspiration values in the Villabate experimental field..... 92
5.2.4 Predicted actual evapotranspiration values in the Castelvetrano experimental field..... 96
5.3 ET estimation on the Villabate experimental field..... 97
5.3.1 In situ measurements: Climatic characterization..... 97
5.3.2 Remote sensing data: Temporal dynamics of vegetation indices 104
5.3.3 Predictive relationship K_c (VIs)..... 105
5.3.4 Application of FAO56 Agro-Hydrological model 108
5.4 ET estimation at the Irrigation District 1A – Castelvetrano.... 113
5.4.1 In situ measurements: Climatic characterization..... 113
5.4.2 Analysis of irrigation volumes database 116
5.4.3 Remote sensing data: Temporal dynamics of vegetation indices 118
5.4.4 Estimation of the basal crop coefficient for olive orchards, based on fraction cover and height crops 120
5.4.5 Applications of FAO56 model in Water Uses Mode (WUM) 123
5.4.6 Application of FAO56 model in Water Requirement Mode (WRM) 127
5.4.7 Irrigation depth estimates by FAO56 Agro-Hydrological model and irrigation delivered to hydrants..... 131
Chapter 6: Conclusion..... 137
6.1 Future research line 141
References 143
Sitography 163
Annexes **..... 167**

List of Figures

Figure 2.1: Schematic representation of the two main approaches used to schematize the SPA system. The red box shows the energy balance components, while the blue box shows the hydrological balance terms. The intersection of the box indicates the evapotranspirative component, which is common to the two approaches. 16

Figure 2.2: schematization of the SPA system in the FAO56 Agro-hydrological model (Rallo et al., 2008)..... 17

Figure 2.3: Temporal dynamic of the basal crop coefficient K_{cb} for a dry bean crop (Allen et al., 1998). 19

Figure 2.4: Relationship between water stress coefficient K_s and soil water content (SWC) (Allen et al., 1998) readapted. 21

Figure 2.5: Conceptual schematization of the interaction between incident energy E_i and a generic surface S (Lechi Giovanmaria, 2001). 22

Figure 2.6: Typical vegetation spectral signature (Moroni et al., 2019). .. 23

Figure 2.7: Vegetation spectral signature in different water status condition: absence of stress (line 11), high water stress (line 17) (Bal et al., 2021). . 24

Figure 2.8: Sentek™ "Drill & Drop" probe to measure soil water content and temperature (https://sentektechnologies.com/products/soil-data-probes/)..... 29

Figure 2.9: Scholander chamber for measurements of leaf water potential (https://www.skyeinstruments.com/digital-system/) and (Awad-Allah, 2020). 30

Figure 2.10: Schematization of functioning of passive a) and active b) remote sensors (M Boyer et al., 1988). 31

Figure 2.11: Example of relative spectral response of the band 1 (costal aerosol) characteristic of the operational land imager (OLI) sensor installed on the Landsat 8 and Landsat 9 mission (https://landsat.gsfc.nasa.gov/article/preliminary-spectral-response-of-the-operational-land-imager-in-band-band-average-relative-spectral-response/). 33

Figure 2.12: Comparison between images characterized by different radiometric resolution from 1 to 8 bit..... 33

Figure 2.13: Geometric representation of field of view (FOV) and instantaneous field of view (IFOV) for optical system. 34

Figure 2.14a, b: Geostationary orbit (a) and sun-synchronous orbit (b) (https://www.esa.int/ESA_Multimedia/Images/2020/03/Geostationary_orbit). 35

Figure 2.15: Sentinel satellite constellation (https://atmosphere.copernicus.eu/copernicus-moves-forward-monitoring-human-carbon-dioxide-emissions). 36

Figure 2.16: Spectral resolution referred to spatial resolution 10 m, 20 m and 60 m of the data acquired by the multispectral sensor (de Marinis et al., 2019) readapted. 37

Figure 2.17: Standard weather station for the measure of clime variables (https://www.campbellsci.de/wxpro). 38

Figure 2.18: Overall vision of the ERA5 a) (https://cds.climate.copernicus.eu/cdsapp#!/dataset/reanalysis-era5-single-levels?tab=overview) and ERA5-Land b) hourly database (https://cds.climate.copernicus.eu/cdsapp#!/dataset/reanalysis-era5-land?tab=overview). 40

Figure 2.19: Example of Eddy covariance (EC) installation with net radiometer a) sonic anemometer b) and gas analyzer c) (https://ibis.geog.ubc.ca/~achristn/infrastructure/oakridge.html) readapted. 41

Figure 2.20: Example of feedforward artificial neural network (ANN).... 43

Figure 3.1: Map of Sicily with the position of SIAS weather stations and the grid of ERA5-Land database. 47

Figure 3.2: Experimental field with location of the weather station (WS), flux tower (EC) and soil water content sensors, the spatial resolution of Sentinel-2 (L2A/L2B) multispectral images is also shown. 49

Figure 3.3: Scene N0207_R079_T33SUB (a) and N0208_R122_T33SUC (b) in true colors with identification of the study area, related to the acquisition dates 2-06-2018 and 3-06-2018. 51

Figure 3.4: Irrigated areas of ex “Garcia-Arancio” district and study area irrigation district 1A (in red). 53

Figure 3.5: Irrigation district 1A. 54

Figure 3.6: Pedologic map of the study area (Bono et al., 1998). 54

Figure 3.7: Example of the paper sheet referred to one user. 56

Figure 3.8: Scene N0207_R079_T33SUB in true colors with identification of the study area. 57

Figure 3.9: Map of the experimental field with the position of the EC tower and the SIAS weather station; the MODIS (MCD43A v006) pixel containing the experimental field is also shown. 58

Figure 4.1: Polygons used for calibration (red areas) and validation (blue areas). 68

Figure 4.2: Example of plot with 25% of canopy surface vectorised, used for calibration of predictive relationship fc-NDVI. 68

Figure 4.3: Functional relationship K_{cb}(NDVI) calculation flow chart. 70

Figure 4.4: Example of the farm encoding. 70

Figure 4.5: Schematization of spatially distributed FAO56 Agro-Hydrological model. 71

Figure 4.6: Spatial distribution of 67 olives orchards divided in calibration (blue) and validation (green) surfaces. 72

Figure 5.1: Scatterplots of daily climate variables (T_{min}, T_{max}, R_s, RH_{min}, RH_{max}, U_{10}) retrieved from ERA5 dataset (E, y-axis) and measured on ground by SIAS (S, x-axis) by the weather stations of Canicattì (ID 208). 78

Figure 5.2: Scatterplot between *ETo* estimated using ERA5-Land climate variables and corresponding ground measurement for the best a) Canicatti (ID= 208) and the worst b) Lentini (ID= 292) weather station. 83

Figure 5.3: Mean values of sensitivity coefficient for each variable and weather stations referred to the analysis period (2006-2015). 84

Figure 5.4: Temporal dynamics of a) daily global solar radiation, R_s, c) average air temperature, T_{avg}, e) average air relative humidity, RH_{avg}, and g) wind speed, U_2, registered by weather station (black line) and ERA5-Land data (blue dots); b), d), f) and h) shows the scatterplot from the two sources. The color bar indicates the day of the year (DOY). 87

Figure 5.5: Temporal dynamics of daily average soil water content (black line), SWC, and precipitation, P in the citrus orchard. SWC profile from 0 to 0.5 m depth is also shown at the bottom of the figure..... 88

Figure 5.6: Temporal dynamics of actual crop evapotranspiration (red dots), ET_a, and precipitation (blue bars), P, for the citrus orchard a) and olive orchard b). 90

Figure 5.7: Temporal dynamics of average NDVI (green line) and NDWI (blue line), retrieved from Sentinel-2 satellites for the citrus orchard..... 91

Figure 5.8: Comparison between the temporal dynamics of NDVI (a) and NDWI (b) retrieved from Sentinel-2 satellites (black line) and MODIS (red line) products for the olive orchard. The corresponding scatterplots of NDVI and NDWI obtained by Sentinel-2 versus the corresponding MODIS are also shown on the right (c, d). 92

Figure 5.9: Temporal dynamic of simulated (black line), $ET_{a\text{-}sim}$, and measured (red dots), $ET_{a\text{-}meas}$, daily actual evapotranspiration obtained for the citrus orchard when considering the complete dataset and assuming the best (a) and the worst (b) combination of the mean and kernel covariance functions. The corresponding scatterplots of estimated versus measured ET_a are also shown (c, d)..... 93

Figure 5.10: Temporal dynamics of simulated (black line), $ET_{a\text{-}sim}$, and measured (red dots), $ET_{a\text{-}meas}$, referred to the three different combinations of the input variables. The corresponding scatterplots of estimated versus measured ET_a are also shown. 97

Figure 5.11: Daily temporal dynamics of maximum and minimum air temperatures a), relative air humidity b) solar radiation c), wind speed d), crop reference evapotranspiration e) and precipitation f) for the three years of observation (2018-2020). 99

Figure 5.12: Temporal dynamic of crop reference evapotranspiration, ETo, precipitation, P, and amount of irrigation, I, from 2018 to 2020. Available values of actual crop evapotranspiration, ET_a, are also shown. The light box

indicates the irrigation season, while the dark box identifies the period of application of water stress. 100

Figure 5.13: Cumulative precipitation, ΣP, crop reference evapotranspiration, ΣETo, and irrigation, ΣI, distributions during 2018–2020. The light box indicates the irrigation season, while the dark box identifies the period of application of water stress. 101

Figure 5.14: Map of the experimental plot showing the EC tower footprint. The inner box shows the scatterplot between hourly ($H+LE$) and ($R_n - G_0$) fluxes measured in 2019 (black dots) and 2020 (grey dots). 102

Figure 5.15: Values of the ratio between measured ET_a and ETo, K_c, in 2019 and 2020. The light box indicates the irrigation season, while the dark one identifies the period of water deficit application. Red arrows indicate the days in which weeds were cut down. 103

Figure 5.16: Temporal dynamic of average NDVI and NDWI, precipitation, P, and the amount of irrigation, I, for the investigated period (2018-2020). The light box indicates the irrigation season, while the dark box identifies the period of application of water stress. Red arrows indicate the days in which weeds were cut down. 104

Figure 5.17: Predictive relationship to estimate the crop coefficient, K_c, from the sum of NDVI+NDWI. 106

Figure 5.18: Maps of NDVI and NDWI obtained from Sentinel-2 acquisitions and corresponding K_c estimated from eq. (5.1) in two days characterized by the absence (June 20, 2019, upper row) and the presence of transpirating cover weeds (December 4, 2019, lower row) on the soil surface. 106

Figure 5.19: Comparison between crop coefficient estimated with eq. 5.1 and the corresponding curves suggested by Allen et al. (2009) and Rallo et al. (2021). The colours associated with the experimental values depend on the combination of NDVI and NDWI. The light grey box indicates the irrigation season (IS), while the dark grey identifies the period of application of water deficit (DI). Precipitation, P, and Irrigation events, I, are indicated in the secondary axes. 107

Figure 5.20: Examples of maps of simulated soil water content, SWC_{sim}, and actual evapotranspiration, ET_a, obtained in the absence (a, June 20, 2019)

and presence (b, December 4, 2019) of active weeds among the tree rows. 109

Figure: 5.21: Temporal dynamics of average and standard deviation of measured SWC_{meas} and corresponding simulated, SWC_{sim}, precipitation, *P*, amount of irrigation, *I* (upper row) and detail of soil water contents measured each 10 cm depth in the layer 0-50 cm (second row); temporal dynamics of crop reference evapotranspiration, *ETo*, and of measured, ET_{a_meas}, and simulated actual evapotranspiration, ET_{a_sim}, (third row); temporal dynamics of measured and estimated K_c^* (lower row) for the simulated periods of 2018, 2019 and 2020..... 111

Figure 5.22: Daily temporal dynamics of maximum and minimum air temperatures a), relative air humidity b) solar radiation c), wind speed d), crop reference evapotranspiration e) and precipitation f) for the three years of observation (2018-2020). 114

Figure 5.23: Temporal trend of the cumulative values of reference crop evapotranspiration and rainfall over the three-year period 2018-2020. .. 115

Figure 5.24: Trend between total pluviometric deficit and total volume delivered within the irrigation district 1A. 117

Figure 5.25: Monthly water supply measured in the irrigation district 1A referred to the olives orchards during the irrigation seasons 2018, 2019 and 2020. 118

Figure 5.26:Spatial distribution of NDVI, over the irrigation district 1A (11/08/2018). 119

Figure 5.27: Spatial distribution of the NDVI over the 1A.9_002 farm relative to the acquisition date 22-07-2018. 119

Figure 5.28: Temporal dynamic of the NDVI during the analysis period (2018-2020). 120

Figure 5.29: Mean and standard deviation of the canopy surface with the increase of the number of the plants in the plot..... 121

Figure 5.30: Scatterplot between fraction cover and NDVI. 122

Figure 5.31: Predictive relationship to estimate the basal crop coefficient, K_{cb}, from the NDVI vegetation index. 123

Figure 5.32: Perimeter of the 1A.9_002 farm. 124

Figure 5.33: Temporal dynamics of average and standard deviation of simulated, SWC, precipitation, *P*, amount of irrigation, *I* (upper row); temporal dynamics of crop reference evapotranspiration, *ETo*, and simulated actual evapotranspiration, ET_a, (second row); temporal dynamics of estimated K_c (third row);temporal dynamics of estimated K_s (fourth row) for the simulated period (01-04-2018 to 30-09-2018)..... 125

Figure 5.34: Perimeter of the 1.16_003 farm. 128

Figure 5.35: Examples of maps of simulated soil water content, SWC, (upper row) and actual evapotranspiration, ET_a, (lower row) for the dates (07/05/2018), (24/06/2018) and (23/07/2018) representative of three different conditions after rain event, after drying period and after irrigation intervention, respectively. 129

Figure 5.36: Temporal dynamics of average of simulated, SWC, precipitation, *P*, amount of irrigation, *I* (upper row); temporal dynamics of crop reference evapotranspiration, *ETo*, and simulated actual evapotranspiration, ET_a, (second row); temporal dynamics of estimated K_c (third row);temporal dynamics of estimated K_s (fourth row) for the simulated period (01-04-2018 to 30-09-2018) 130

Figure 5.37: Comparison between measured and simulated daily irrigation depth for the two irrigation seasons examined (2018 and 2019), the rainfall events are also shown. 132

Figure 5.38: Monthly irrigation depth estimated by FAO56 model (mm) (grey bars) *vs*. monthly irrigation depth supplied at hydrants (mm) (black bars), during irrigation seasons 2018 a) and 2019 b). Monthly rain and crop reference evapotranspiration are also indicated in the secondary axis.... 133

Figure 5.39: Comparison between measured and simulated cumulative irrigation volumes during irrigation seasons 2018 a) and 2019 b)..... 134

List of Tables

Table 3.1: Identification code (ID), name of SIAS climatic station, geographic coordinates and number of available records in the period 2006-2015 48

Table 3.2: Size distribution of the soil within the irrigation district 1A 55

Table 3.3: Soil water retention curve coefficients estimate by means "ROSETTA" software 56

Table 4.1: Different combinations of input variables 64

Table 4.2: Values for the variables used for FAO56 model simulations. . 67

Table 4.3: Clear-sky Sentinel-2 available scenes and date of GEP aerial image referred to the study area 69

Table 4.4: Values of variable used to run the A&P procedure 69

Table 5.1: Values of RMSE and MBE associated to the climate variables calculated for all the weather stations. **79**

Table 5.2: Statistical indices associated to *ETo* values estimated with SIAS and ERA5-Land database. 82

Table 5.3: Statistical indicators associated with the GPR model implemented with the best *m(x)* and *k(x,x')* functions and the five combinations of the input variables, for the citrus orchard. 94

Table 5.4: Statistical indicators associated with the GPR model implemented with the best *m(x)* and *k(x,x')* functions and the three combinations of the input variables, for the olive orchard. 96

Table 5.5: Cumulated annual precipitation, ΣP amount of irrigation, ΣI , crop reference evapotranspiration, ΣETo , and pluviometric deficit $\Sigma(P - ETo)$, in the three years before, during and after irrigation seasons 102

Table 5.6: Results of the statistical analysis to check the FAO56 model performance 112

Table 5.7: Cumulated values of crop reference evapotranspiration, rainfall and pluviometric deficit annual and during the irrigation season (01/06 - 30/09) 116

Table 5.8: Pluviometric deficit and water supply within the irrigation district 1A for the period 2009-2020 116

Table 5.9: Farmer's irrigation management parameters..... 126

Table 5.10: Values for the variables used for FAO56 model simulations. 127

List of symbols

Symbol	Unit	Description
c_p	[J kg^{-1} K^{-1}]	Specific heat of air at constant pressure
∂ETo		variation of reference evapotranspiration caused by the change associated to the variable
∂vi		Change associated to the variable v_i
b		Slope of the regression line
C		Total capacity
e_a	[kPa]	Actual vapour pressure
E_a		Absorbed energy
E_i		Incident electromagnetic energy
E_i		Individual error of each variable
E_r		Reflected energy
e_s	[kPa]	Saturation vapour pressure
E_t		Transmitted energy
ET_a	[mm]	Actual evapotranspiration
ET_c	[mm]	Potential avapotranspiration
ETo	[mm]	Crop reference evapotranspiration
F_a		Frequency measured by the sensor in air
F_s		Frequency measured by the sensor in the soil
F_w		Frequency measured by the sensor in the water
F	[V/m]	Electric field
$f(x)$		Gaussian process
f_c		Fraction of ground cover
F_r		Correction parameter representative of the vegetation stomatic control
f_w		Fraction of soil wetted not covered by the vegetation
G_0	[MJ m−2 d^{-1}]	Soil heat flux
g_f		Constant that depends on the geometric configuration of the electrode
H	[MJ m−2 d^{-1}]	Sensible heat flux
h_{crop}	[m]	Height of the crop
$k(x,x')$		Covariance kernel

Symbol	Unit	Description
K_c		Crop coefficient
K^*_c		Actual crop coeffient
K_{cb}		Basal crop coefficient
$K_{cb(tab.)}$		Basal crop coefficient tabulated
$K_{cbcover}$		value of crop coefficient referred to the ground cover, in absence of weeds
K_{cbfull}		Basal crop coefficient referred to intermediate phase of the phenological cycle of the plant
K_d		Density coefficient
K_e		Soil water evaporation coefficient
K_h		Indicate the effects due by the height of the crop
K_r		Reduction dimensionless coefficient
K_s		Stress coefficient
L		Inductance
$m(x)$		Mean of the Gaussian process
M_L		Corrective coefficient on fraction of ground cover
N		Number of groups in which the database is randomly divided
n		Coefficient of the soil water retention curve
p		Depletion factor
P_{int}	[mm]	Canopy interception
P_n	[mm]	Net precipitation
P_r	[dB]	Received power
P_s	[dB]	Emitted power
p_{tab}		Depletion factor tabulated
R^2		Coefficient of determination
r_{ah}	[s m^{-1}]	Aerodynamic resistance
r_c	[s m^{-1}]	Canopy stomatal resistance
rl	[s m^{-1}]	Leaf resistance
RH_{min}	[%]	Minimum relative air humidity
RH_{max}	[%]	Maximum relative air humidity
R_n	[MJ m−2 d^{-1}]	Net radiation
R_{oi}	[mm]	Surface runoff
R_s	[MJ m−2 d^{-1}]	Global solar radiation

Symbol	Unit	Description
S	[m^2]	Generic surface
S	[m]	Flight altitude or earth-sensor distance
SF		Scaled frequency
S_c		Sensitivity coefficient
T_a	[°C]	Air temperature
T_{avg}	[°C]	Average air temperature
T_{min}	[°C]	Minimum air temperature
T_{max}	[°C]	Maximum air temperature
T_{dew}	[°C]	Dew-point temperature
T_p	[mm]	Potential transpiration
U	[m s^{-1}]	Wind speed
U_{v_10}	[m s^{-1}]	Vertical component of wind speed at 10 meter above the soil
U_{H_10}	[m s^{-1}]	Vertical component of wind speed at 10 meter above the soil
U_{10}	[m s^{-1}]	Wind speed at 10 meter above the soil
U_2	[m s^{-1}]	Wind speed at 2 meter above the soil
v_i		Generic variable
$\overline{x}$		Mean of measured data
z_r	[m]	Root depth
α		Transmittance
α		Coefficient of the soil water retention curve
γ	[kPa $°C^{-1}$]	Air psychrometric constant
Δ	[kPa $°C^{-1}$]	Slope of vapor pressure curve
ε		Noisy observations of the true function expressed as a normal distribution characterized by a mean equal to zero and variance estimated from the data
θ^*	[cm^3 cm^{-3}]	Critical threshold of soil water content
θ_{fc}	[cm^3 cm^{-3}]	Soil water content at field capacity
θ_{wp}	[cm^3 cm^{-3}]	Soil water content at wilting point
λ	[nm]	Wavelength
λET	[MJ m−2 d^{-1}]	Latent heat flux
ρ	[Kg m^{-3}]	Air density
ρ		Reflectance
σ_n^2		Variance

Symbol	Unit	Description
σ_{Wq}	[g m^{-2} s^{-1}]	Covariance between vertical wind speed and the water vapor density
σ_{WT}	[m K s^{-1}]	Covariance between vertical wind speed and air temperature
τ		Absorbance
ε_b		Dielectric constant
σ^0	[dB]	Backscattering coefficient
A	[m]	Swath width
$y(x)$		Random variable underlying the observations
Ψ_{md}	[Mpa]	Midday leaf water potential
Ψ_{pd}	[Mpa]	Pre-dawn leaf water potential
Ψ_s	[Mpa]	Soil water potential

List of acronyms

Acronym	Description
A&P	Allen and Pereira
ANBI	Associazione Nazionale Bonifiche Irrigazioni
ANNs	Artificial Neural Networks
bit	BInary digiT
BOA	Bottom Of Atmosphere
C3S	Copernicus Climate Change Services
CR	Capillary Rise
CR	Closure Ratio
CWR	Crop Water Requirement
DEM	Digital Elevation Model
DI	Deficit Irrigation
DN	Digital Numbers
DOY	Day Of the Year
DP	Dep Percolation
DSR	Downward Shortwave Radiation
E	Evaporation
EB	Energy Balance
EC	Eddy Covariance
ECMWF	European Centre for Medium-Range Weather Forecasts
EM	Electromagnetic
ERA5-L	ERA5-Land
ESA	European Space Agency
ET	Evapotranspiration
EVI	Enhanced Vegetation Index
FAO56-PM	FAO56 Penman-Monteith
FDR	Frequency Domain Reflectometry
FOV	Field Of View
GEP	Google Earth Pro
GLASS	Global LAnd Surface Satellite
GPR	Gaussian Process Regression
IFOV	Instant Field Of View

Acronym	Description
IPCC	Intergovernmental Panel on Climate Change
JAXA	Japan Aerospace Exploration Agency
LAI	Leaf Area Index
LIDAR	LIght Detection And Ranging
LST	Land Surface Temperature
LSWI	Land Surface Water Index
MAE	Mean Absolute Error
MBE	Mean Bias Error
ML	Machine learning
MLP	Multilayer Perceptron
MODIS	MODerate resolution Imaging Spectroradiometer
MSI	Multi Spectral Images
NASA	National Aeronautics and Space Administration
NCPE	National Centers for Environmental Prediction
NDVI	Normalized Difference Vegetation Index
NDWI	Normalized Difference Water Index
NIR	Near-Infrared
NSE	Nash Sutcliffe Efficiency
OLI	Operation Land Imager
PAR	Photosynthetically Active Radiation
PBIAS	Percent BIAS
PM	Penman-Monteith
QGis	Quantum Gis
RAW	Readily Available Water
RDI	Regulated Deficit Irrigation
RF	Random Forest
RMSE	Root Mean Square Error
RS	Remote Sensing
SAR	Synthetic Aperture Radar
SAVI	Soil Adjusted Vegetation Index
SDI	Subsurface Drip Irrigation
SIAS	Servizio Informativo Agrometeorologico Siciliano
SIMS	Satellite Irrigation Management Support
SPA	Soil-Plant-Atmosphere
SVM	Support Vector Machine

Acronym	Description
SVR	Support Vector Regression
SWB	Soil Water Balance
SWC	Soil Water Content
SWIR	Short-Wave-Infrared
T	Transpiration
TAW	Total Available Water
TDR	Time Domain Reflectometry
UNESCO	United Nations Educational, Scientific and Cultural Organization
USDA	Unite State Department of Agriculture
VIS	Visible
VIs	Vegetation Indices
WD	WatchDog
WMS	Web Map Service
WRM	Water Requirements Mode
WUM	Water Use Mode

Chapter 1: Introduction

1.1 Water uses in agriculture: General overview

The increase of the global surface temperature caused by global warming and climate change, is having important ecological consequences, such as changing of the precipitation regime and the distribution of the vegetation species. The evidence and the scenarios shown in the Intergovernmental Panel on Climate Change (IPCC) reports, indicate that the surface temperature has increased of about 1°C from 1850 to the first two decades of the 21st century (2001–2020) (IPCC, 2022). These data are alarming; especially for the possible effect that, climate change may have on ecosystems, on populations and on economic sectors that depend by the climate conditions such as the agro-food sector. According to the World Population Prospects 2022 (UN DESA/POP, 2022), recently released by United Nations Educational, Scientific and Cultural Organization (UNESCO), although in the 2020 the growth rate of the global population fell under 1%, the projections suggest that world's population could grow to around 8.5 billion in 2030 until to reach a peak of 10.40 billion during the 2080. This produces an increase of natural resource use, such as food and fresh water. The freshwater resources are not infinite, especially for the water used in agriculture which represents about 70% of the available freshwater (UNESCO, 2021).

Italy is among the European countries with the highest demand on irrigation. In the irrigation season 2009-2010, 11,618 Mm^3 were used about 2,489,914.70 ha (ISTAT, 2014). However, irrigation efficiency is low and about 50% of the water is wasted (ISTAT, 2014). For this reason, is very important to develop strategies to increase water use efficiency and reduce water demand. The optimization of water use efficiency is one of the main challenges of the 21st century, as discussed at the global level by politicians and the scientific community.

Agriculture 4.0 is the last advancement in farming technology, based on four main pillars: increasing productivity, sustainable use of natural resources, resilience to climate change and reducing food waste (Zhai et al., 2020). Technological innovation in irrigation aims to improve the use of water in

agriculture thus, irrigation systems are characterized by devices that ensure high uniformity of distribution and reduce water demand. If from one on side the technological innovation contributes to reducing water and energy consumption, on the other side it is necessary to implement political actions finalized to regulate the pricing policies, in order to guarantee to farmers an efficient service.

Water management for irrigation generally involves many different professional figures distributed on several levels and connected to each other by a dense network of structures and offices distributed throughout the territory.

In Italy, the irrigation distribution is managed by the "Associazione Nazionale Bonifiche Irrigazioni miglioramenti fondiari" (ANBI) through 141 territorial structures named "reclamation consortium", which covers a surface equal to 59% of the total national surface characterized by different agricultural systems suitable for the different climate conditions. The main activities of the reclamation consortiums are building and management of defence and hydraulic regulation structures, as well as the distribution and pricing of water for irrigation scope.

In Sicily (D.P.R n. 467 of 12/09/2017) locate two actual reclamation consortiums named "Consorzio di Bonifica della Sicilia Occidentale" and "Consorzio di Bonifica della Sicilia Orientale", that incorporating the previous 11 consortiums divided as 5 (Trapani 1, Palermo 2, Agrigento 3, Caltanissetta 4, Gela 5) and 6 (Enna 6, Caltagirone 7, Ragusa 8, Catania 9, Siracusa 10, Messina 11), respectively. The main crops in both areas are those typical of the Mediterranean basin such as olives, citrus, vineyards and open field vegetables and arable fields, with the sporadic presence of floriculture plants.

Water supply is conveyed by pressure pipes in almost the totality of the "Consorzio di Bonifica della Sicilia Occidentale", while in the "Consorzio di Bonifica della Sicilia Orientale" they alternate with open channels. The last, need more control and maintenance activities than the other in order to guarantee sustainable distribution efficiency.

1.2 Strategies for sustainable water use in agriculture

Managing the water resources in a sustainable way means finding new equilibriums among human needs, technological progress, and environment quality. The improvement of water use efficiency, by innovative technologies and irrigation techniques, will reduce water waste. It can represent a reliable solution to optimize water use and increase production, especially in areas where water resources are limited, and water scarcity characterizes most part of the year climate.

Low pressure localized irrigation can be a reasonable choice to achieve high water use efficiency levels. In this field, Subsurface Drip Irrigation (SDI) may provide an improvement in irrigation water use efficiency. Ayars et al. (2015) identified the SDI main advantages such as: increased yield, improved crop quality, reduction in applied water and reduced agronomic costs for weed control, fertilization, and tillage. Furthermore, the pipeline's position under the soil surface avoids the contact between irrigation water with operators and products; this allows the use of reclaimed wastewater for irrigation purposes (Palacios-Díaz et al., 2009). On the one hand SDI is a suitable method to optimize water use efficiency, on the other hand, the significant initial installation cost, suggests that the application of SDI can be really advantageous if the system efficiency is guaranteed for at least 15-20 years (Lamm et al., 2015). The possibility to automate the system, combined with the capacity to apply small volumes, allow the adoption of Deficit Irrigation (DI) strategies.

The latter consists in applying an amount of water less than the total plant water needs. When DI is applied during specific phases of crop growth, the DI strategy is named Regulated Deficit Irrigation (RDI) (Chalmers et al., 1981). This strategy has been studied by several authors (Castel, 2000; Gonzalez-Altozano and Castel, 2000; Rallo et al., 2017; Puig-Sirera et al., 2021), asserting that the application of RDI during the stage II of crop growth allows the water-saving without determining significant effects on crop yield. However, the application of DI strategies requires monitoring of soil and plant water status to determine the amount of irrigation necessary to fulfil the actual plant water requirement and to avoid severe crop water stress, which can produce a decline in crop yield and/or irreversible effects on crop growth.

1.3 Models and remotely sensed data to assess crop water requirements

To estimate crop water requirements over large spatial scales, quasi-continuous over-time and spatially distributed meteorological information are necessary.

Several gridded weather and climate dataset have been generated and are freely downloadable at global scale. These offer different temporal resolution and moderately high spatial resolution. The European Centre for Medium-Range Weather Forecasts (ECMWF), coupling weather forecast models and data assimilation systems, periodically 'reanalyse' available past observations to create global data sets of atmospheric and land surface variables represented in 'maps' without gaps. Reanalysis data, based on data assimilation, are among the most used to study weather and climate (Parker, 2016). Reanalysis method combines model and data based on past observations from across the world, for monitoring and forecasting climate change, for research, education, and commercial applications.

The latest ERA5-Land (ERA5-L) product released in 2019 as the evolution of previous ERA5 dataset, aimed at enhancing the resolution of the spatial grid to 0.1° latitude and 0.1° longitude. The usability of ERA-L to assess *ETo*, was studied by Pelosi et al. (2021), who found that in absence of ground weather data the ERA5-L database is a suitable resource to replace missing weather data. Recently also Araújo et al. (2022), using the air temperature, T_a, (°C) retrieved from ERA5-L, found that in some zone of Pernambuco state where ground weather data are not always available, the reanalysis database represents a good alternative.

Based on the evaluation of sensitivity coefficients, S_c, sensitivity analysis allows us to understand the effect on the model's output because of changing the value of the inputs. Several applications of sensitivity analysis are described in literature considering different reanalysis database, different theoretical approaches, and weather condition (Gong et al. 2006; Liang et al. 2008; Koudahe et al. 2018; Anderton et al. 2002). This approach allows to identify which variables need greater precision in measurement or estimation.

The results with the above-mentioned methods depend on the quality and the continuity of the available data time series. The occurrence of acquisition

gaps of one or more sensors compromises the continuity of the records; anomalies are generally due to failure, improper installation of the sensors or incorrect calibration, as well as the poor maintenance of sensors or data logger. Moreover, the occurrence of outliers in time series can also compromise the output quality and could generate inconsistent results mainly when model simulations are applied.

Machine learning (ML) techniques have recently been proposed as suitable methods for time series gap-filling. Bellido-jiménez et al. (2021) assessed the performance of three different ML models such as MultiLayer Perceptron (MLP), Support Vector Machine (SVM) and Random Forest (RF), to fill the gaps in daily rainfall series. Moreover, ML models have been often used in agriculture applications to simulate crop reference evapotranspiration (Chen et al., 2022; Kim et al., 2020) with Root Mean Square Error (RMSE) values ranging between 0.28 to 1.14 mm d^{-1} as well as a Mean Absolute Error (MAE) between 0.18 to 0.87 mm d^{-1}.

Among other ML models, the Gaussian Process Regression (GPR) associated with Sentinel-2 Multi Spectral Images (MSI) level 2A has been used to investigate the possibility to assess the Leaf Area Index (LAI) at the field scale and support farmers' management (Amin et al., 2021). The GPR is a non-parametric model based on statistical Bayesian theory, characterized by a mean and a kernel function, that can be used to solve supervised multivariate regression and classification issues such as high-dimensional, small-sample, and nonlinear problems (Rasmussen et al., 2006; Murphy, 2012).

Despite several authors have been investigated the suitability of ML models to predict daily actual evapotranspiration, in most cases; they have the availability of long temporal series of data for training and validating the models. However, when the availability of training data is limited, the GPR model can allow to retrieval of synthetic temporal series (Rasmussen et al., 2006), representing a reasonable choice to fill gaps in the considered time series of actual evapotranspiration. Moreover, the use of reanalysis climate data as well as Remote Sensing (RS) data, to estimate ET_a, can be a useful solution to predict ET_a in those areas where ground measurements are not available.

The monitoring of the soil and plant water status is crucial to estimates the crop water requirement of the plant. A widely accepted practical approach

to estimate crop water requirement is the FAO56 (Allen et al. 1998), in which crop potential evapotranspiration, ET_c, is calculated as the product of crop reference evapotranspiration, *ETo*, and a single or dual crop coefficient (K_c or $K_{cb} + K_e$), where *ETo* represents the meteorological evaporative demand (Allen et al. 1998). The standard method to estimate *ETo* is the FAO56 Penman–Monteith (PM) equation (Allen et al. 1998). Due to its simplicity, the FAO56 approach has been widely applied to various crops to estimate water requirements and to compute all the terms of Soil Water Balance (SWB) in the root zone, based on a simplified reservoir scheme. Actual crop evapotranspiration, ET_a, can be, therefore, estimated as the product of *ETo* and the term ($K_{cb} K_s + K_e$), where K_s is the stress coefficient. Based on the first publication of the tabulated values of crop coefficients (Allen et al. 1998), in the last decade, the scientific community has revised the crop coefficients values considering the specific crop varieties or climate conditions and adding K_c values for crops not originally considered (Pereira et al. 2015; Rallo et al. 2021). However, these coefficients are generally referred to specific conditions, such as the presence or the absence of active ground cover or weeds, and are assumed valid during the entire irrigation season, without including the possibility of time-variable conditions.

Despite the RS technique has not been considered in the FAO56 method, it represents an useful tool to quantify various vegetation parameters such as albedo, surface temperature, crop coefficients, and LAI, with the advantage to capture their spatial and temporal variability at different scales. Regarding the crop coefficient K_c, two different RS techniques have been proposed in literature. The first one is analytical, and based on the direct application of the PM equation in which input data for crop characterization (LAI, height and albedo) are estimated using multispectral images operating in the Visible and Near-Infrared (VIS–NIR) domain (D'Urso, 2001; Minacapilli et al. 2008); the second technique is based on a Vegetation Indices (VIs) approach, based on the assumption of a direct relationship between K_c(VIs) and various vegetation spectral indices (i.e., NDVI, SAVI, EVI, etc.) derived from reflectances in the VIS–NIR, domain (Alam et al., 2018; Er-Raki et al., 2013; Gontia and Tiwari, 2010; Kamble et al., 2013). An overview of the RS data and missions mostly used to implement the K_c(VIs) approaches, running from satellite missions with long imagery archives to new satellite programs and constellations, has been recently proposed by

Pocas et al. (2020). The main advantage of the K_c(VIs) approach is that the VIs operating in the VIS–NIR domain are readily available; on the other hand, the K_c(VIs) approach is based on crop-specific statistical regressions, whose assessment requires calibration and validation procedures.

1.4 Thesis objectives

The planning of irrigation water uses through strategies that meet environmentally sustainable policies is one of the main challenges of the 21st century.
The availability of climate and RS data characterized by accurate spatial and temporal resolution, joint with the innovative proximity represents reliable support to achieve the environmental sustainability objectives planned by the governments. The general objective of the thesis was to assess crop water requirements using models based on proximal and remotely sensed data at different spatial scales. In two study areas, characterized by typical Sicilian crops and Mediterranean climate, the temporal and spatial variability of the VIs has been used to compute functional relationship between crop coefficient and VIs. While the atmospheric evaporative request was evaluated through the main climate variables, retrieved from ground weather station and reanalysis data.
The specific objectives of this thesis work can be summarized in four main lines:

- Evaluate the ERA5-L climate variables quality, to predict daily crop reference evapotranspiration in Sicily, Italy, and by means of sensitivity analysis identify the main variables that most influence the estimation of *ETo* by the FAO56 Penman-Monteith (FAO56-PM) equation.

- Assess the suitability of the ML algorithm, based on proximal and RS data, to fill gaps in daily time series of actual evapotranspiration acquired in Mediterranean citrus and olive orchards.

- Estimate, for typical Sicilian crops (citrus and olives) reliable crop coefficient K_c values with VIs retrieved by remotely sensing using a specific relationship K_c(VIs).

- Evaluate the suitability of the proposed K_c(VIs) relationship combined with the FAO56 Agro-Hydrological model to estimate soil water contents(SWC) and actual crop evapotranspiration.

Regarding the first point, the scope of the analysis allows to assess the quality of the ERA5-L climate variables in a region like Sicily characterized by a heterogeneous morphology and the presence of the sea that could influence the climate variable; likewise, it identifies which climate variables need to be estimated more accurately.
Finally, the second point allows to test the prediction capability of the GPR algorithm when the availability of training data is limited.
The third and fourth points focus the attention on the estimation of crop water requirements based on predictive relationships K_c(VIs). In the literature this approach has been applied for herbaceous crops that uniformly cover the soil surface, while only a few investigations have been carried out on sparse vegetation; for these cases, experimental research is still necessary to develop reliable predictive relationships K_c(VIs), especially for sparse tree crops such as citrus and olives orchards, characterized by sporadic presence of active ground weeds that can temporarily spread over the soil surface.

1.5 Thesis Structure

The thesis is organised into 6 chapters, the first and the last ones report the introduction and conclusion of the thesis work. The other chapters are subdivided in four main parts: ii) theoretical background, iii) materials, iv) methods, v) results and discussion.

Chapter 1: Introduction

This chapter is divided into five parts: the first summaries the importance of the water saving in agriculture and the institutions responsible of the agricultural water management at national (Italy) and regional (Sicily) levels. The second part explains the advantages in terms of water use

efficiency and water saving achievable using innovative systems and unconventional irrigation strategies. The third part reports the contribution of the remotely sensed data joint with the Agro-Hydrological models to assess crop water requirements. The fourth and fifth parts report the objectives and the thesis structure.

Chapter 2: Theoretical Background

The second chapter describes the theoretical background. It is divided into four main sections. The first outlines the concept of the crop water requirement in agriculture, whereas the second part describes the schematization of the energy and mass balances approaches in the Soil-Plant-Atmosphere (SPA) system. The third section shows the theoretical basis of the FAO56 Agro-Hydrological model implemented in the thesis work. Moreover, the section 2.3.1 explores the possibility to derive the crop parameters by means the analysis of the vegetation spectral response. The last part describes the techniques to monitor the different components of the SPA system.

Chapter 3: Materials

The third chapter initially describes the position of the 39 weather stations, managed by the "Servizio Informativo Agrometeorologico Siciliano" (SIAS), and the variables considered for the further analysis. The second and the third section describes the citrus orchard located near to the Villabate town and the irrigation district 1\A managed by "Consorzio di Bonifica della Sicilia Occidentale", located in Castelvetrano, Sicily (Italy), respectively. Overall, the chapter three describes instruments and tools used for the research activities in both the case studies, such as weather station, Eddy Covariance (EC) flux towers and RS satellite images.

Chapter 4: Methods

This chapter reports the methodologies used in the research application, as well as the models and the algorithms implemented. The first and second sections report the FAO56-PM equation to estimate crop reference evapotranspiration, *ETo*, and the GPR algorithm to predict actual

evapotranspiration, ET_a. The third and fourth parts describe the approaches used to calibrate the functional relationships K_c(VIs) and the boundary condition set to run the FAO56 Agro-Hydrological model, respectively for the citrus orchard and the irrigation district 1\A. In particular, the fourth part describes the possibility to use the FAO56 Agro-Hydrological model in two different modes: Water Use Mode (WUM) and Water Requirement Mode (WRM). Finally, the last section details the statistical indicators used to quantify the quality of the results obtained.

Chapter 5: Results and Discussion

In this part, results are outlined and critically analysed. The chapter focuses mainly on the application of the ERA5-L climate variables to estimate crop reference evapotranspiration, *ETo*, the use GPR algorithm to predict actual evapotranspiration, ET_a, and on the assessment of crop water requirements and irrigation scheduling using the FAO56 Agro-Hydrological model in a spatially distributed way. The result obtained by the application of FAO56 Agro-Hydrological model in the citrus orchard are compared to flux tower and SWC measurements, whereas in the irrigation district the results are compared to the irrigation volumes delivered by the hydrants.

Chapter 6: Conclusion

The chapter summarizes main results obtained in the thesis work. The potentials and limits of the applied methodology are highlighted. Moreover, future developments in this researcher line are suggested.

Chapter 2: Theoretical background

2.1 Crop water requirement assessment in agriculture: General overview

The correct quantification of the water resource availability becomes largely important for agricultural, civil and industrial activities. Under the evident reduction in water availability the competition among the different demanding sectors, drastically increases. In the Mediterranean regions, irrigation practices are the highest water consume activities especially during the irrigation season. Therefore, accurate assessments of Crop Water Requirement (CWR) are necessary to improve and optimize the irrigation water use in agricultural.
The CWR in absence of irrigation can be summarized as the difference between evapotranspiration (ET) and net precipitation (P_n).

$$\mathrm{CWR} = ET - P_n \tag{2.1}$$

The net precipitation, P_n can be easily calculated, as reduction of the gross precipitation of the canopy interception, by means empirical methods (Braden, 1985). While the ET represents the sum of two different components: Evaporation (E) from the soil and Transpiration (T) from the plant canopy. Evaporation explains the physical process in which liquid water is converted to vapor and removed from the evaporating surface.
The transpiration describes the process of vaporization of water contained in plant tissue, converted from the liquid state to vapor.
The assessment of the amount of water loss from the soil (through evaporation) and vegetation (through transpiration) (Pereira et al., 2015), in fact, is fundamental to improve agricultural water irrigation saving.
The evaporation and transpiration process are simultaneous and difficult to be distinguished (Allen et al., 1998), therefore is necessary to use theoretical schematization to simplify the complex environmental systems.
One of the early approaches to estimate the amount of the evapotranspiration fluxes was developed by Penman (1948) with the “big-leaf” approach, for surfaces characterized by wet surface-atmosphere interface. This approach

was further elaborate by Penman (1956), introducing the concept of stomatal resistance, r_s (s m^{-1}), representative of the resistance of the stomata to the flux vapour, joint with the aerodynamic resistance, r_{ah} (s m^{-1}).
The up scaling from leaf to canopy of the conceptualization provided by Penman (1956) was realised by Monteith (1965) introducing the big-leaf approach. The approach is based on hypothesis that the canopy is modelled as a single large leaf placed at a fixed height inside the crop, where the latent heath flux or evapotranspiration, λET, is expressed by the know formulation named Penman-Monteith (PM) equation:

$$\lambda ET = \frac{\Delta(R_n - G_0) + \rho c_p \frac{(e_s - e_a)}{r_{ah}}}{\Delta + \gamma\left(1 + \frac{r_c}{r_{ah}}\right)} \tag{2.2}$$

Where: Δ(kPa °C^{-1}) is the slope of vapor pressure curve, R_n (MJ m^{-2} d^{-1}) is the net radiation at the crop surface, G_0 (MJ m^{-2} d^{-1}) is the soil heat flux density, ρ (kg m^{-3}) is the air density, c_p (J kg^{-1} K^{-1}) is the specific heat of air at constant pressure, e_s and e_a (kPa) are the saturation and actual vapor pressure, r_{ah} and r_c (s m^{-1}) are aerodynamic and canopy stomatal resistance, γ (kPa °C^{-1}) is the air psychrometric constant.
The above approach, although very rigorous, is complex due to the need of estimations of crop-specific r_{ah} and r_c. In order to provide a solution to this limitation, Allen et al. (1998), introduced the concept of crop reference evapotranspiration, *ETo*. This quantity is defined as "the rate of evapotranspiration from a hypothetical reference crop, characterized by height of 0.12 m, surface resistance of 70 s m^{-1} and albedo of 0.23, closely resembling the evapotranspiration from an extensive surface of green grass of uniform height, actively growing, well-watered, and completely shading the ground".
To compute the value of potential evapotranspiration, ET_c for every crop type, in well-watered unstressed condition, Allen et al. (1998) introduced the concept of crop coefficient, K_c. This coefficient represents an integration of the effects of the main characteristics that distinguish the crop reference from a generic crop (Allen et al., 1998).
The K_c can be defined as the ratio between, ET_c and *ETo*.

$$K_c = \frac{ET_c}{ET_o} \tag{2.3}$$

For several crop these values are cataloged in specific table in the FAO56 paper (Allen et al., 1998) and recently updated by Rallo et al. (2021). Moreover, in the FAO56 paper, there is the methodology to adapt the K_c values to different weather conditions.
Combining ET_c from eq. (2.3) and replacing ET_c in eq. (2.1) it is possible to obtain the crop water requirement for every crop type.

$$\text{CWR} = (ET_o K_c) - P_n \tag{2.4}$$

Therefore, in agricultural applications and for irrigation purposes, CWR can be estimated using equation (2.4). When more accurate estimates are needed, it is necessary to consider approaches based on the physical resolution of complex environmental systems.

2.2 Soil-Plant-Atmosphere (SPA) system: Energy and Soil water balance approach

The schematization of the complex environmental systems is based on the identification of blocks named "compartments" these can be ideal or real regions of the space. An environmental system is defined by the interconnection between different compartments (Vismara, 1992).
In agricultural ecosystems, Philip (1957) suggests that hydraulic interactions can be conceptualized with the SPA system.
The hydraulic relationships in the SPA system can be studied by resolving the Energy Balance (EB) or SWB. Whose terms are shown in figure 2.1.
In the EB, the R_n, is in part transferred in the soil, G_0, while the main amount is transformed in sensible, H, (W m^{-2}) and latent, L, (W m^{-2}) heat or (evapotranspiration).
In the EB approach, ET is obtained as residual term of EB

$$\lambda ET = R_n - H - G_0 \tag{2.5}$$

Where: λET is latent heat flux or evapotranspiration, R_n is net radiation, H is sensible heat flux and G_0 soil heat flux.

The models based on the resolution of the EB, in general use two different schematizations: the first is the "one source" or "big leaf" (Monteith, 1965), this consider the vegetation as an homogeneous, semi-transparent surface in which the phenomena of soil evaporation and plant transpiration are considered jointly. On the other hand, the second approach known as "two-layer" or "two-source" considers the two previous phenomena separated through a partition between energy fluxes in the soil and energy fluxes in the canopy alone (Shu'itleworth and Wallace, 1985).

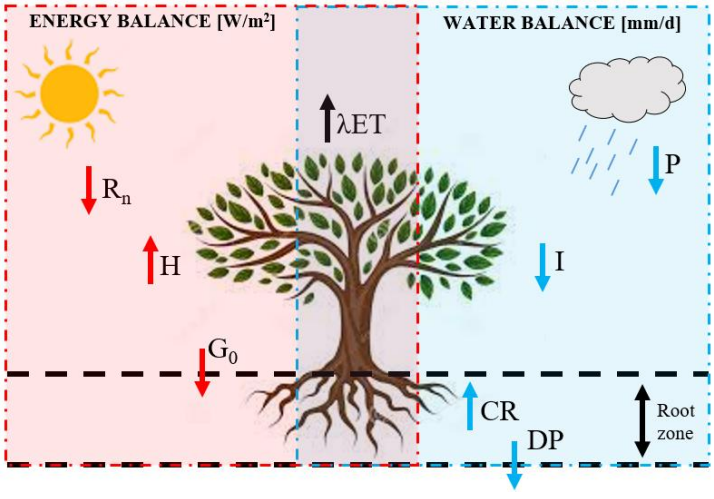

Figure 2.1: Schematic representation of the two main approaches used to schematize the SPA system. The red box shows the energy balance components, while the blue box shows the hydrological balance terms. The intersection of the box indicates the evapotranspirative component, which is common to the two approaches.

The resolution of the WB between the incoming flux (precipitation, P, irrigation, I and capillary rise, CR) and exiting (ET_a, and dep percolation, DP), allows to estimate, the SWC dynamic, in the SPA system.

$$\Delta \mathrm{SWC} = P + I + CR - ET - DP \tag{2.6}$$

The WB models can be divided in two categories: the first, considers the SPA system as a single reservoir in which the terms of the SWB are described through simple schematizations often based on empirical equations.

The other category is based instead on a more complex schematization that uses physics-based laws for the study of water fluxes in unsaturated systems coupled with equations or models describing root drawdown in the soil.
For both categories, in case of fully availability of water in soil, potential crop evapotranspiration, ET_c can be calculated as product between crop coefficient K_c and crop reference evapotranspiration, *ETo*.
The first category of models, includes the FAO56 Agro-hydrological model presented in FAO56 paper (Allen et al., 1998), while in the second one are included HYDRUS-2D/3D, SWAP, ACRUS etc. models, in which the equations that describes physical phenomena are solved to compute the balance terms.

2.3 Water exchange modelling in the SPA system: FAO56 Agro-hydrological model

In the FAO56 Agro-hydrological model (Allen et al., 1998) the soil is considered as a bucket characterized by a specific capacity, that depend by root depth and the hydraulic soil proprieties (fig. 2.2).

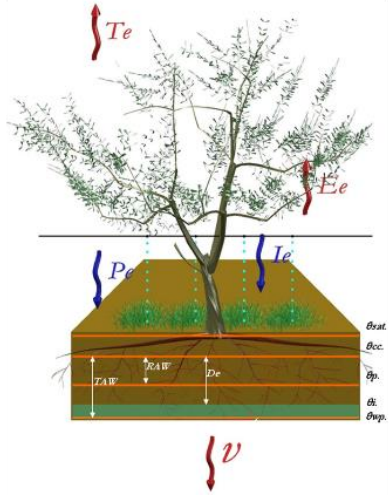

Figure 2.2: schematization of the SPA system in the FAO56 Agro-hydrological model (Rallo et al., 2008).

Specifically, in this model the SWC dynamic is expressed through an exhaustion function.

$$D_i = D_{i-1} - (P_i - Ro_i) - I_i - CR_i + ET_{a,i} + DP_i \quad (2.7)$$

where: D_i and D_{i-1} (mm) are the root zone depletions at the end of the day i and i-1, P_i (mm) is the net precipitation, R_{oi} (mm) is the surface runoff, I_i (mm) is the irrigation depth, CR (mm) is the capillary rise from underground aquifer, ET_{ai} (mm) is the actual crop evapotranspiration, and DP_i (mm) is the deep percolation of water moving out of the root zone.
The depletion function domain ranges between zeros, corresponding to the field capacity, θ_{fc} to a maximum value expressed by the Total Available Water (TAW) (mm).

$$\mathrm{TAW} = 1000(\theta_{fc} - \theta_{wp})z_r \quad (2.8)$$

where θ_{fc} ($cm^3\ cm^{-3}$) and θ_{wp} ($cm^3\ cm^{-3}$) are the SWC at field capacity and at wilting point, respectively, and z_r is the root depth (m).
As proposed by Allen et al. (1998) the FAO56 model can be implemented following the single or dual crop coefficient approach. Specifically in the single crop coefficient approach the relationship between daily potential evapotranspiration, ET_c, and daily crop reference evapotranspiration is described trough the crop coefficient, K_c.

$$ET_c = K_c ET_o \quad (2.9)$$

where ET_c is the potential evapotranspiration referred a hypothetic surface cultivated in well-watered condition in absence of stress condition.
In the dual crop coefficient approach the K_c is separate into the basal crop coefficient, K_{cb}, and soil water evaporation coefficient, K_e, including a corrective coefficient, K_s, expressive of actual crop water stress condition.

$$ET_a = (K_{cb}K_s + K_e)ET_o \quad (2.10)$$

where: ET_a and ETo are expressed in mm d^{-1}.
The K_{cb} coefficient is representative of the ratio between the potential transpiration T_p, and ETo. The K_{cb} coefficient considers the factors referred to the ground cover condition, crop characteristics and r_{ah}. In particular, K_{cb} depends on the height of the crop, h_{crop}, which influences the r_{ah}, as well as, on the albedo, α, on which the amount of available solar radiation for

transpiration processes and finally on the r_c, on which the exchanges of water vapor between plant and atmosphere.
In the table 17 of the FAO56 paper are reported typical values of K_{cb} referred to many crops in specific environmental conditions with minimum relative air humidity, RH_{min} (%) at least equal to 45% and wind speed at 2 meter above the soil, U_2, equal to 2 (m s^{-1}). Therefore, when the real conditions are different from the theoretical ones it is necessary to correct the values using the following expression.

$$K_{cb} = K_{cb(tab.)} + [0.04(U_2 - 2) - 0.004(RH_{min} - 45)]\left(\frac{h_{crop}}{3}\right)^{0.3} \quad (2.11)$$

where $K_{cb(tab.)}$ is the basal crop coefficient tabulated.
The temporal dynamic of K_{cb} changes according to the phenological cycle of the crops, for this reason, the authors of the FAO56 paper suggest a division of the phenological cycle into four periods, each with different specific duration for the crop considered.

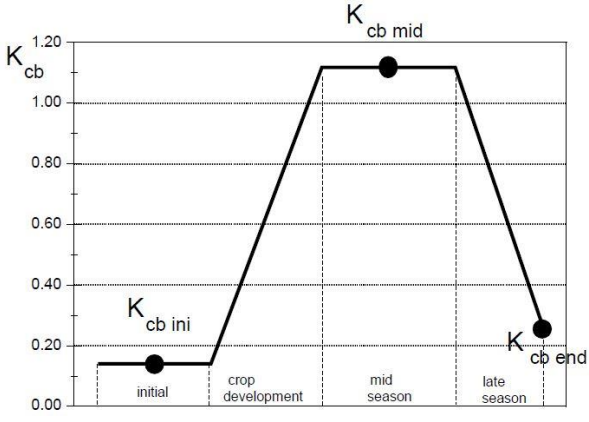

Figure 2.3: Temporal dynamic of the basal crop coefficient K_{cb} for a dry bean crop (Allen et al., 1998).

Such as an example, figure 2.3 shows the K_{cb} temporal dynamic during the four phenological phases, for a dry bean crop.
The water stress coefficient, K_s, is representative to the real SWC condition, therefore the actual transpiration, T_a, can be obtained as product between K_s and potential transpiration T_p.

$$T_a = T_p K_s \tag{2.12}$$

Figure 2.4 shows the relationship between K_s and SWC, as well as, the relation between the K_s values and matrix potential, expressed as the height of the water column, obtained considering the soil retention curve.
The relationship between K_s and SWC, numerically can be evaluated through a linear relation.

$$K_s = \frac{\mathrm{TAW} - D_i}{\mathrm{TAW} - \mathrm{RAW}} \tag{2.13}$$

where: D_i is the depletion at i-th day and Readily Available Water (RAW). The RAW is expressed as the product between TAW and the depletion factor, p.

$$\mathrm{RAW} = p\ \mathrm{TAW} \tag{2.14}$$

where the depletion factor, p, is the rate of TAW that a crop can extract from the root zone without suffering water stress, to which corresponds a value of SWC > critical threshold of soil water content, θ^*, ($cm^3\ cm^{-3}$) while when the SWC< θ^* the K_s value is under the unit. Values of p are listed in table 22 of the FAO56 and are specific for the different crops, they generally varies from 0.30 (crops with shallow roots) to 0.70 (deep rooted crops) is possible considering a value equal to 0.50 for many crops (Allen et al., 1998). When the atmospheric water demand conditions are different from those where the listed values were obtained, the authors of the FAO56 paper suggest a linear correction relationship in function of the crop reference evapotranspiration.

$$p = p_{tab} + 0.04(5 - ET_o) \tag{2.15}$$

where p_{tab} is the depletion factor tabulated and ETo is the crop reference evapotranspiration.

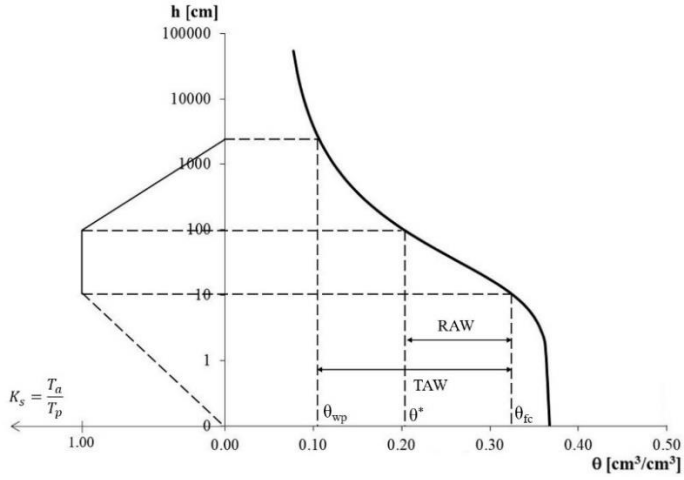

Figure 2.4: Relationship between water stress coefficient K_s and soil water content (SWC) (Allen et al., 1998) readapted.

The evaporative coefficient, K_e, represent the potential evaporation E_p, and *ETo* ratio.
This coefficient depends on the SWC condition and can be evaluated numerically as minimum of two functions.

$$K_e = min\{K_r(K_{c\_max} - K_{cb}); f_w K_{c\_max}\} \quad (2.16)$$

where K_r is a dimensionless reduction coefficient ranging between 0, when the soil is dry, and 1 during the periods after rain or irrigation events; K_{c_max} is the maximum value of the sum $K_{cb} + K_e$ and f_w is the fraction of soil wetted not covered by the vegetation.

2.3.1 Crop coefficient estimation based on spectral data

It is possible to conceptualize in three components the energetic interactions between a generic surface, *S*, to the incident Electroagnetic (EM) energy: E_i, reflected energy, E_r, absorbed energy, E_a, and transmitted energy E_t (fig. 2.5).

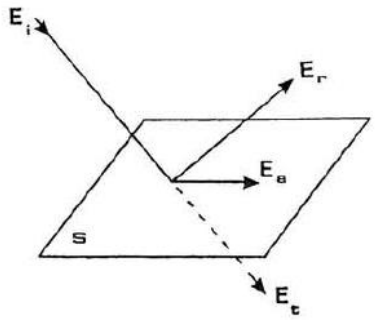

Figure 2.5: Conceptual schematization of the interaction between incident energy E_i and a generic surface S (Lechi Giovanmaria, 2001).

The ratio between each component and E_i, defines three different optical properties: reflectance, ρ, absorbance α and transmittance, τ, specific for every material and dependent only on the chemical-fiscal proprieties of the surface of the material. The sum of these components expresses the principle of energy conservation.

$$\rho + \tau + \alpha = 1 \tag{2.17}$$

The values of the three coefficients, for the same surface change in function of the wavelength, λ, of the incident EM energy, E_i. The reflectance, ρ, variation in function of the different wavelengths of the solar spectrum, λ, is represented in a graph called spectral signature. Based on the analysis of the spectral signature acquired from a vegetated surface (fig.2.6) (Moroni et al., 2019), it is possible to observe different regions of the EM spectrum representative of the plant water status.
In the region of the VIS spectrum (400-750 nm) almost the energy is absorbed especially by the chlorophyll, in fact, there are two evident minimums values of ρ in correspondence the pigment absorption peaks (420-490 nm) and in the red region (660 nm). While in correspondence of the 540 nm and 690-720 nm wavelengths, there are two peaks named green peak and red edge, respectively. The region of the NIR (750-1350 nm) is characterized by high values of ρ representative of the morph-anatomical characteristics of the leaf (M. Boyer et al., 1988).

Moreover, in the 970 nm and 1200 nm wavelengths, there are two minimums due to the absorption of water (Jacquemoud et al., 2003). Other characteristic peaks of absorption of water can be seen in the Short-Wave-Infrared (SWIR) region (1400-2500 nm) centred around the 1450 nm, 1940 nm and 2200 nm.

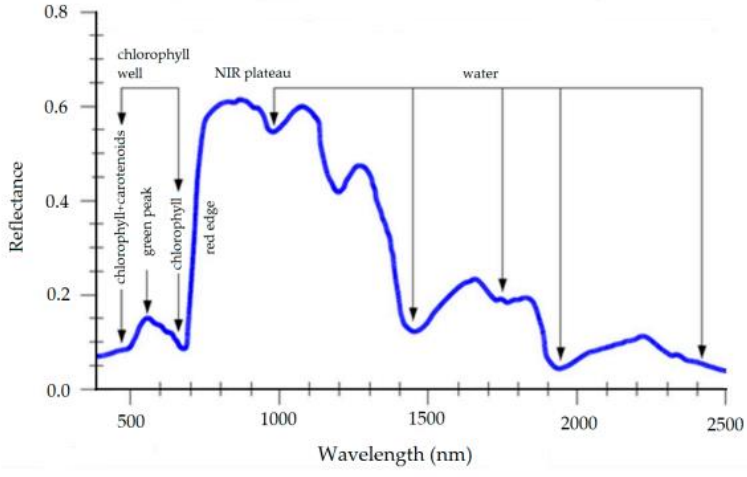

Figure 2.6: Typical vegetation spectral signature (Moroni et al., 2019).

The analysis of the vegetation spectral signature can provide information about the plant's health state and water status (Rallo et al., 2014; Sims and Gamon, 2003).

In the NIR region, high values of reflectance can indicate healthy vegetation (Moroni et al., 2019). With reference to the analysis of the plant water status, Bal et al. (2021) observed that in the VIS region the reflectance values were more accentuated in the vegetation with high degree of desiccation (line 17), rather than in the well-watered vegetation (line 11) (fig 2.7).

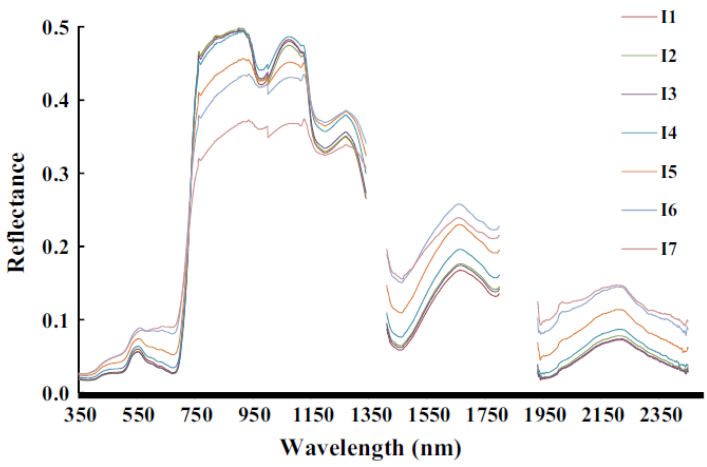

Figure 2.7: Vegetation spectral signature in different water status condition: absence of stress (line 11), high water stress (line 17) (Bal et al., 2021).

The spectral signature analysis can be supported introducing VIs (Moroni et al., 2013). Regarding the plant water status detection, the stressing agents affect reflectances in certain wavelengths representative to the physiological characteristics of plants, the appropriate combination of these bands allows to monitor plant's health state (Moroni et al., 2019). The VIs tries to assess the possible changes in reflectances values in specific bands of the EM spectrum, as these can be a symptom of biological alteration. Many VIs has been empirically obtained combining bands associated to specific wavelengths of the vegetation spectral signature. Xue and Su, (2017) published an interesting review of VIs available in the literature, showing their specific application field according to the vegetation of interest and environmental condition. Among the VIs based on the variation of the biochemical and morpho-anatomical characteristics the Normalized Difference Vegetation Index (NDVI) (Rouse et al., 1974) is commonly used to monitor plant vigour, amount of green biomass, plant stress, photosynthetic and agricultural crop yield (Asrar et al., 1984; Moriondo et al., 2007; Sellers, 1987).

$$\mathrm{NDVI} = \frac{\rho_{860} - \rho_{640}}{\rho_{860} + \rho_{640}} \tag{2.18}$$

where ρ_{860} and ρ_{640} are the reflectance of the NIR and red, respectively. The reflectance in the red wavelength, ρ_{640}, is representative of the absorption of light by chlorophyll, while the wavelength of the NIR, ρ_{860}, is sensitive to changes in the internal structure of the leaves (Petropoulos and Kalaitzidis, 2012). Usually, NDVI assume values ranging between -1 to +1. In general, water surface has typical values less than 0, bare soils between 0 to 0.30 and vegetation over 0.35 until 0.75 -0.80 (Kriegler et al., 1969).
However, when a specific vegetated surface is fully covered and chlorophyll content is saturated, NDVI is not able to describe the real amount of chlorophyll and increase of this variable does not result in proportional increase of the NDVI (Huete et al., 1997).
The VIs can be useful also to monitor the surface humidity; in this way, the Normalized Difference Water Index (NDWI) is sensitive to monitor the surface humidity (Gao, 1996).

$$\mathrm{NDWI} = \frac{\rho_{860} - \rho_{1240}}{\rho_{860} + \rho_{1240}} \tag{2.19}$$

where ρ_{860} and ρ_{1240} are the wavelengths of NIR and SWIR respectively. Ceccato et al., 2001) demonstrated that NDWI is able to remove the variation caused by leaf internal structure and leaf dry matter content, improving the reliability in assessing the vegetation water content.
The evident similarities between the temporal patterns of K_c and VIs encouraged the scientific communities to find alternative approaches to estimate the crop coefficients.
The onset of approaches based on predictive relationship K_c(VIs) are described in pioneering studies (Bausch, 1993; Neale et al., 1989; Bausch and Neale, 1987). Calera et al. (2017) and Pôças et al. (2020) in recent studies highlighted that K_{cb} is most correlated, through linear or non-linear K_{cb}(VIs) functional relationships, with VIs based on VIS and NIR wavelengths, such as NDVI and SAVI.

2.3.2 Estimation of basal crop coefficient based on fraction ground cover and crop height

The Allen and Pereira (A&P) approach, proposed in Allen and Pereira (2009) estimates K_{cb} by means observed fraction of ground cover, f_c, and crop height, h_{crop}.

$$K_{cb} = Kcb_{cover} + K_d \left(\max \left[Kcb_{full} - Kcb_{cover}, \frac{Kcb_{full} - Kcb_{cover}}{2} \right] \right) \quad (2.20)$$

where: $K_{cbcover}$ is the value of K_{cb} referred to the ground cover and, in absence of weeds, can be assumed equal to zero, K_d is the density coefficient, K_{cbfull} is the basal crop coefficient referred to intermediate phase of the phenological cycle of the plant.
To implement the equation 2.20 is necessary to compute K_{cbfull} and K_d. For K_{cbfull} it is possible to use the following formula.

$$Kcb_{full} = F_r \left(\begin{array}{c} \min\left(1 + K_h\, h_{crop}, 1.20\right) + \\ +[0.04(U_2 - 2) - 0.004(RH_{min} - 45)] \left(\frac{h_{crop}}{3}\right)^{0.3} \end{array} \right) \quad (2.21)$$

where F_r is a correction parameter representative of the vegetation stomatic control; K_h indicates the effects due by the height of the crop by means the sum ($1+K_h\, h_{crop}$), for tree crops K_h can be assumed equal to 0.10 while for herbaceous crops equal to 0.20; h_{crop} represents the crop height; U_2 is the wind speed at 2 m above the soil and RH_{min} is the average minimum relative air humidity and h_{crop} is the height of the crop.
The F_r parameter changes according to the type of crop analyzed and can be evaluated as suggested in the FAO56 paper (Allen et al., 1998)

$$F_r \approx \frac{\Delta + \gamma(1 + 0.34\, U_2)}{\Delta + \gamma\left(1 + 0.34\, U_2 \frac{r_l}{100}\right)} \quad (2.22)$$

where: Δ(kPa°C^{-1}) is the slope of vapor pressure curve, γ (kPa°C^{-1}) is the psychrometric constant, r_l (s m^{-1}) is the mean leaf resistance for the vegetation considered.

The values of density coefficient, K_d, can be calculated as suggested in the A&P approach.

$$K_d = \min\left(1, M_L\, f_c, f_c^{\left(\frac{1}{1+h_{crop}}\right)}\right) \quad (2.23)$$

where: M_L is a corrective coefficient on f_c describing the effect of canopy density on shading and on maximum relative ET per fraction of ground shaded (the values suggest in the A&P approach ranging 1.5 to 2), and h_{crop}, is the height of the canopy.
The A&P approach was validated by Pereira et al. (2020) by ground and RS data. Specifically, the authors used f_c, retrieved by RS data, to define a K_d coefficient that was used to directly estimate annual K_c and K_{cb} values for perennial crops. The same authors for perennial crops (peach and wine grapes) used the K_{cb} values, retrieved by RS, to estimate, ET_c, that was compared with $ET_{c\text{-}SIMS}$ obtained from Satellite Irrigation Management Support (SIMS). The comparison shows values of slope of regression line, b, and determination coefficient, R^2, equal to 1.08 and 0.91, respectively. These results show the utility of the A&P approach joined with RS data for eventual application in irrigation scheduling and management. However, the authors specify that it is opportune to test the A&P approach for a variety of herbaceous and tree species with a specific attention on the parameterization of the A&P equations.

2.4 Monitoring of SPA system components

2.4.1 Techniques for soil water status monitoring

To understand the dynamics in the compartments of the SPA system, it is necessary to identify the appropriate physical indicators and accurate monitoring techniques.
Several techniques are available to monitoring SWC status, based on the direct or indirect measurements of physical quantities correlated to SWC. The thermo-gravimetric method is the most frequently applied direct method since it is simple and allows precise measurements of water content (Topp and Ferré, 2002). Indirect methods instead are based on the measurements of the physical or chemical properties of the analysed soil

(e.g., dielectric constant, electrical conductivity, heat capacity, content of hydrogen atoms).
Among the indirect methods to measure SWC in continuous, the most recognized are those based on the Time Domain Reflectometry (TDR) and Frequency Domain Reflectometry (FDR) (Robinson et al., 2008).
The first method is based on the measurement of the soil's dielectric constant ε_b, knowing this value through empirical methods or conceptual models is possible to obtain the SWC value (Roth et al., 1990), referred to the sensor installation point. Such as an example, Topp and Reynolds (1998) based on the value of ε_b suggested an empirical expression to derive the SWC values in soil with different textures.
In the FDR method, the soil is considered as a portion of a capacitor, in which the dipoles in the dielectric medium are polarized under the action of an electric field, *F*. The capacitive probes allow the measure of ε_b that depends on the amount of water in the soil. In particular, an high value of water content in the soil corresponds to an high value of dielectric constant and consequently a low frequency of oscillation of the *F*, measured by the sensor (Williams et al., 2003). Therefore, given the frequency and the electrode configuration, the relation between dielectric constant ε_b and total capacity, *C* can be expressed as follow:

$$C = g_f \, \varepsilon_b \tag{2.24}$$

where g_f is a constant that depends on the geometric configuration of the electrode (size, shapes, and distance between the electrode).
The frequency of oscillation of the *F*, for a fixed value of inductance, *L*, depends only on the *C*, of the capacitor identified by the electrode-field system.

$$F = \left(2\pi\sqrt{L\,C}\right)^{-1} \tag{2.25}$$

specifically, *F* is proportional only to the ratio of air and water present in the soil. The values of *F* are stored in a datalogger, and processed using a normalized equation to obtain a Scaled Frequency (SF):

$$\mathrm{SF} = \frac{F_a - F_s}{F_a - F_w} \tag{2.26}$$

where F_a, F_s and F_w are the frequency measured by the sensor in air, soil and water respectively. Finally, the values of SF are converted in SWC through a calibration equation, specific to each type of soil.
Among the commercially available sensors based on the FDR technique to evaluate SWC, the "Drill & Drop" probes (fig. 2.8) manufactured and commercialized by Sentek™ Sensor Technologies, Australia, are one of the most used.

Figure 2.8: Sentek™ "Drill & Drop" probe to measure soil water content and temperature (https://sentektechnologies.com/products/soil-data-probes/).

The Sentek™ Drill & Drop probes are fully sealed soil probes, designed for insertion into the ground, to measure SWC, temperature and optionally, salinity. To involve water intrusion the sensors are encapsulated with a resin in the probe plastic. To allow the perfect contact between soil and probe, the shape of the probe is tapered, with a diameter equal to 2.5 cm at the bottom and 3.0 cm at the top.
The probes come in different lengths from 30 cm (3 sensors) to 120 cm (12 sensors), one sensor for each 10 cm of depth (SENTEK, 2001), with the first sensor centred at 5 cm from the top of the device. The number of sensors inside the probe allows monitoring the dynamic of the SWC profile.
The measurement of the dielectric constant acquired by the probes can be affected by the presence of roots or air gaps between soil and the sensors. These two effects were recently studied by Dainese et al. (2022), who concluded that, among the two problems, the major is the formation of air gaps between the probe and the soil. Specifically, they found that the presence of air gaps between the probe and sensors can cause an overestimation in the SWC measurement equal to 2.2 mm, which in some cases when is requested high precision, it is not acceptable.

2.4.2 Techniques for plant water status monitoring

The plant water status can be monitored by using direct and indirect methods (Turner and Thomas, 1998). A reliable direct method to assess plant water status is the measure of leaf or stem water potential (Jones, 1990; Koide et al., 1989). These measurements allow to consider at the same time environmental conditions (e.g., SWC and evaporative demand) and plant physiological processes (e.g., root water uptake, lymph transport and stomatal regulation) (Jain et al., 2021). The Scholander pressure chamber is the classical instrument to measure the leaf or water potential (fig. 2.9).

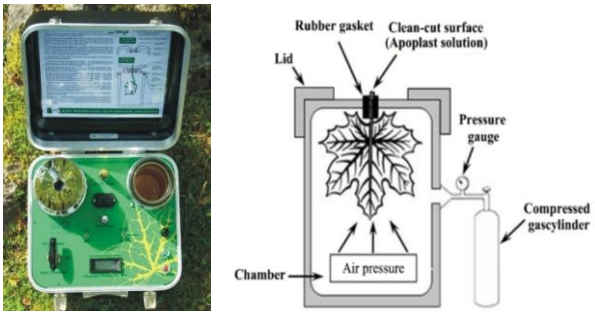

Figure 2.9: Scholander chamber for measurements of leaf water potential (https://www.skyeinstruments.com/digital-system/) and (Awad-Allah, 2020).

The pressure chamber is equipped with a steel cylinder connected to a pressure gauge and a tank of inert gas (nitrogen). The operator inserts inside the steel cylinder, from the side of the cutting surface, the vegetation material for conduct the trial, then close hermetically the cylinder and begins to introduce inert gas (nitrogen). The leaf water potential measurement is equal to the pressure value that occurs when the lymph flux returns to the severed ends.

For the plant water status based on the water potential measurements, it is possible use the parts of the canopy that allows observing the cutting surface. The most used parts are the single leaves or small twigs. The dynamic of leaf water potential shows a daily temporal variability according to the environmental request. Several authors have studied, in different crops, the possibility to monitoring the plant water status by using "pre-dawn", Ψ_{pd}, (MPa) and "midday", Ψ_{md}, (MPa) leaf water potential values

(Jones, 2004; Tuccio et al., 2019). Specifically, the Ψ_{pd} is representative of the soil water potential, Ψ_s, assuming that during the night the plant transpiration is close to zero (Rallo and Provenzano, 2013), while the Ψ_{md} measured on a non-transpiring steam mainly depends on the soil water status (Begg' And and Turner, 1970). Despite the leaf water potential is considered an affordable variable for direct determinations of plant water status, these measurements require specific skills of the operators, are destructive and expensive in terms of time consuming (Rallo et al., 2017).

The study of the plant's optical properties can be considered a useful solution for indirect evaluations of plant's water status (Garnon and Qiu, 1999). Depending on the distance between sensor and target (land surface o plant) is possible identify two different data acquisition systems proximal and RS. Moreover, the manner to acquire electromagnetic signals can distinguish active and passive sensors.

An example of passive proximity sensor, for plant water status detection is the spectroradiometer; these instruments return the values of reflectance referred to the wavelength interval ranging between 350-2500 nm. This instrument is most used for research purposes at plant or leaf scale, but over large areas, the spectroradiometric measurements are labour-intensive and time-consuming, due to the large number of observations necessary to characterize a single plot. Moreover, the high cost of the instruments and the necessity of proper calibration limit their usability.

As already highlighted, the techniques of monitoring through remote sensors are also based on passive and active sensors (fig.2.10).

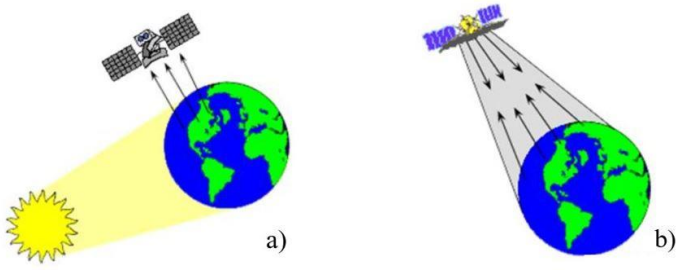

Figure 2.10: Schematization of functioning of passive a) and active b) remote sensors (M Boyer et al., 1988).

A typical active remote sensor is the RADAR, that measures the amount of energy or backscattering coefficient, σ^0, reflected by the target hit by the EM wave generated by the sensor.

$$\sigma^0 = 10 \log \frac{P_r}{P_s} \tag{2.27}$$

where P_r and P_s are the received and emitted power, respectively. In some cases, P_r can have a very low value, for this reason, σ^0 is expressed in (dB) and the working wavelength range is in the microwave range (17.2-0.4 GHz).

Light detection and ranging (LIDAR) system is also an active sensor that provide information about the concentration of chemical species in atmosphere, as well as the Synthetic Aperture Radar (SAR) systems that provide accurate measurements of altitude useful for interferometric application.

Passive sensors use solar radiation and measure the amount of energy reflected from the earth surface. These sensors, usually acquire the EM energy in the range of VIS, NIR and sometimes in SWIR region of the EM spectrum.

The passive remote sensors are installed on the specific satellites named "payloads"; which play a significant role in the sense of the number of information that a single satellite can provide. The first RS systems were based on a single sensor, but with new technology and computers advancement processes, the multisensory platform has become more affordable and economically advantageous (Nagai et al., 2009; Paparoditis et al., 2012).

The characteristics and the quality of the RS data depends by the spectral resolution, radiometric resolution, spatial resolution, and temporal resolution.

The spectral resolution indicates, for fixed wavelength range, the number of spectral bands available from a given sensor. The spectral band is an area of the EM spectrum centred in a specific wavelength. The sensitivity of a single spectral band is defined by the relative spectral response function (fig. 2.11). Based on the number of spectral bands present in the sensors, this can be identified as hyperspectral or multispectral sensor. The ability of the sensor

to discriminate the energy differences between different surfaces depends by the radiometric resolution.

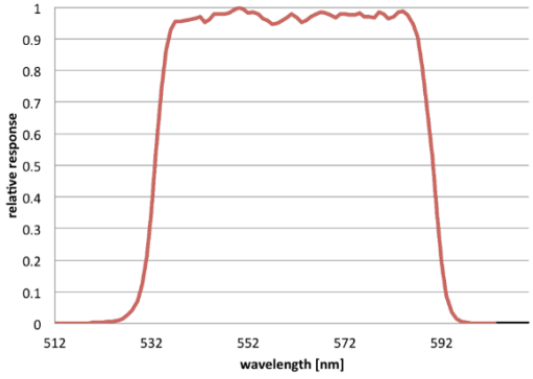

Figure 2.11: Example of relative spectral response of the band 1 (costal aerosol) characteristic of the operational land imager (OLI) sensor installed on the Landsat 8 and Landsat 9 mission (https://landsat.gsfc.nasa.gov/article/preliminary-spectral-response-of-the-operational-land-imager-in-band-band-average-relative-spectral-response/).

The most sensitive sensors are those able to detect the small differences in reflected energy. The memory space storage express in terms of Binary digiT (bit) depends also by the radiometric resolution. Remotely sensed data are represented by positive Digital Numbers (DN) which vary from 0 to a fixed power of 2. This range corresponds to the number of bit used for coding numbers in binary format. Each bit records an exponent of power 2. The maximum number of radiance levels detectable depends on the number of bits used in representing the energy recorded. If a sensor uses an 8 bits coding to record the data, this means that there are 256 DN values, ranging from 0 to 256 to represent the different energy levels. Figure 2.12 shows the comparison between images characterized by different radiometric resolution from 8- bit to 1- bit image.

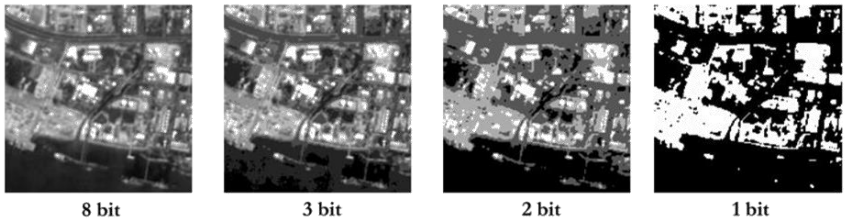

Figure 2.12: Comparison between images characterized by different radiometric resolution from 1 to 8 bit.

There is an evident difference in the level of detail discernible between 8-bit and 1-bit image which is dependent on their radiometric resolutions.
The spatial resolution represents the portion of geographical area interested in the survey, also known as pixel. In RS application, the spatial resolution is defined using angular characteristics: Field Of View (FOV) and Instant Field Of View (IFOV) (fig. 2.13).

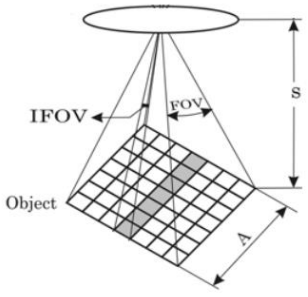

Figure 2.13: Geometric representation of field of view (FOV) and instantaneous field of view (IFOV) for optical system.

The FOV is defined as an angle of vision of the whole swath width A

$$A = S \cdot \mathrm{FOV} \tag{2.28}$$

where S is the flight altitude or earth-sensor distance, and IFOV is the angle of vision of one pixel expressed as Ground Simple Distance (GSD).

$$\mathrm{GSD} = S \cdot \mathrm{IFOV} \tag{2.29}$$

The value of IFOV for a specific band defines the amount of reflected energy that the sensor can acquire. In the VIS region, the amount of available reflected energy is greater than in the SWIR region, thus the spatial resolution in this region will be worse than in the VIS region.
Temporal resolution represents the frequency with which a sensor revisits the same part of the earth's surface. This value depends on the design of the satellite sensor and its orbit pattern. For earth observation purposes, there are two main types of orbits geostationary and sun-synchronous (fig. 2.14a,b)
(https://www.esa.int/Enabling_Support/Space_Transportation/Types_of_orbits).

The satellites with a geostationary orbit are synchronous with the earth's rotation. In particular, the satellites that need to stay constantly above a specific zone, such as telecommunication, weather or radar, use this kind of orbit. Whereas the satellites with sun-synchronous orbit travel past earth from north to south, synchronous with the sun. Thus, the satellite always visits the same zone at the same local time.

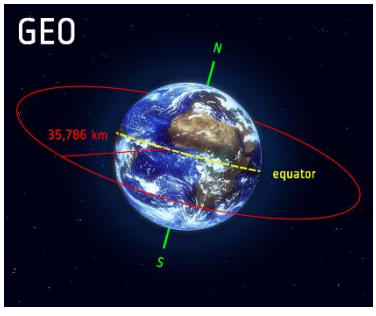

a)

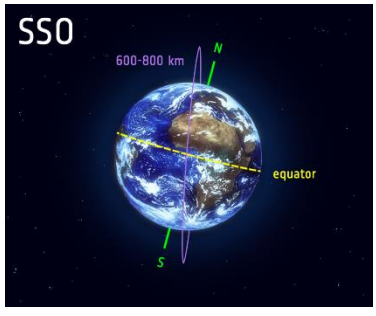

b)

Figure 2.14a, b: Geostationary orbit (a) and sun-synchronous orbit (b) (https://www.esa.int/ESA_Multimedia/Images/2020/03/Geostationary_orbit).

The time interval between one acquisition and the next one is the temporal resolution. The possibility to monitor the same place at different time instant is very important to detect the possible changes in the environment. For this reason, the satellites for earth observation and environmental applications are generally sun synchronous.

Earth observation, through satellite platforms, begins about 50 years ago, with the Landsat-1 launched by National Aeronautics and Space Administration (NASA) in 1972, with the intent to monitor the landmasses, until the last earth observation mission Landsat 9 launched by NASA in 2021. The "eoPortal" (https://directory.eoportal.org/web/eoportal/home) is an useful database developed by ESA aimed at providing detailed information, on the number of earth observation missions, currently in operation, and also on the historical missions.

The choice of the best available RS products, for a specific purpose is a very important question. Many satellites provide RS products characterized da different performances in terms of spatial, temporal, spectral and radiometric resolution.

In the frame of the Copernicus, (https://www.copernicus.eu) programme, managed by the European Commission, aimed to offer information about

satellite earth observation and in-situ data. Sentinel-2A and Sentinel-2B together with other six satellites complete the Sentinel satellite constellation (fig. 2.15) (https://www.esa.int/Applications/Observing_the_Earth/Copernicus/The_Sentinel_missions).
The objective of the Sentinel-2 mission is provide global acquisition of MSI with high spatial and temporal resolution, to allow land monitoring and detection of environmental changes.
The twin satellites Sentinel-2A and Sentinel-2B launched by European Space Agency (ESA) in June 2015 and in March 2017, respectively, operate simultaneously, phased at 180° to each other, in a sun-synchronous orbit at a mean altitude of 786 km from the earth's surface.

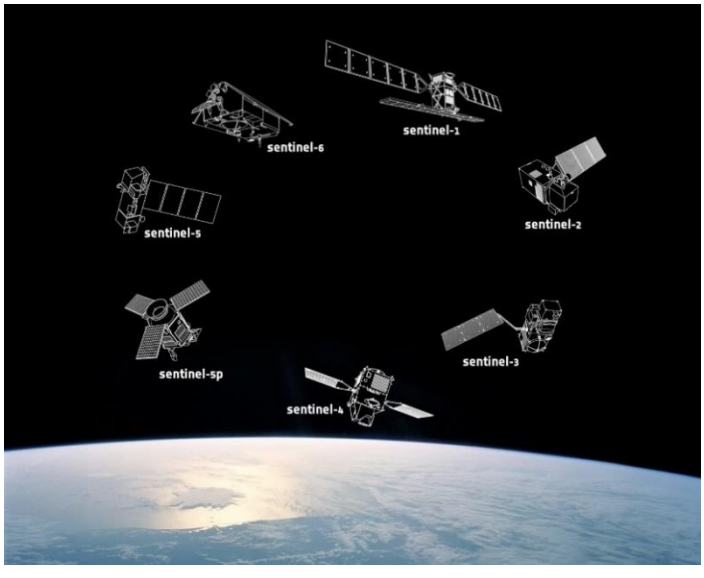

Figure 2.15: Sentinel satellite constellation (https://atmosphere.copernicus.eu/copernicus-moves-forward-monitoring-human-carbon-dioxide-emissions).

The temporal resolution referred to each single satellite is 10 days, while combined the two satellites is 5 days. Both satellites are equipped with a passive multispectral sensor that allows a swath width equal to 290 km, with a radiometric resolution of 12-bit, able to acquire light intensity (radiance) values ranging between 0 to 4095.

The data are acquired on 13 bands distributed between VIS and SWIR. The spatial resolution depends on the specific spectral band (fig. 2.16).
Specifically, as showed in fig. 2.16, there are four bands with spatial resolution equal to 10 m, centred on wavelengths equal to 490 nm (B2), 560 nm (B3), 665 nm (B4) and 842 nm (B8). Six bands with spatial resolution equal to 20 m, centred on wavelengths equal to 705 nm (B5), 740 nm (B6), 783 nm (B7), 865 nm (B8a), 1610 nm (B11) and 2190 nm (B12) and three bands at 60 m, centred on wavelengths equal to 443 nm (B1), 945 nm (B9) and 1 375 nm (B10).
The last product MSI level 2A, acquired by twin satellites Sentinel-2A and Sentinel-2B, released by ESA and free downloaded through the open access hub portal (https://scihub.copernicus.eu/dhus/#/home), provides bottom of atmosphere (BOA) reflectance atmospheric corrected (Main-Knorn et al., 2017), orthorectified and georeferenced with cartographic geometry (UTM/WGS84 EPSG:32633).

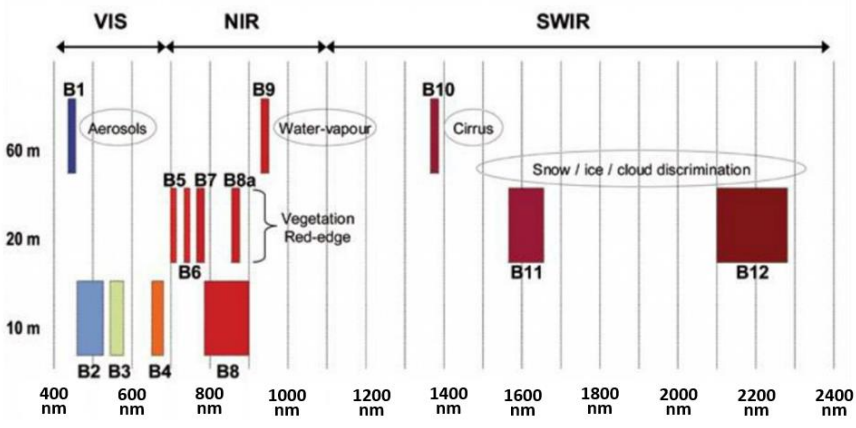

Figure 2.16: Spectral resolution referred to spatial resolution 10 m, 20 m and 60 m of the data acquired by the multispectral sensor (de Marinis et al., 2019) readapted.

Thanks to the high spatial resolution joint with the good revisiting time, this product is able to monitor, at large scale, eventual quick changes in the plant chemical-physical system, as well as, to monitor and estimate plant water status and crop water requirement (el Hachimi et al., 2022; Rozenstein et al., 2018).

2.4.3 Techniques for crop reference evapotranspiration monitoring

The measurement of *ET* can be performed by means empirical models or thermodynamic based models, as well as trough micrometeorological system. Crop reference evapotranspiration, *ETo*, can be considered a climate parameter and represent the atmospheric water demand referred to a water unlimited evaporative surface.
The estimation of *ETo* needs climate variables acquired by standard weather station, properly installed (fig. 2.17).
The climate variables, generally measured by standard weather station, are T_a, relative air humidity, *RH*, (%) wind speed, *U*, (m s^{-1}) and global solar radiation, R_s, (MJ $m^{-2}d^{-1}$).
In literature there are several computational methods to estimate *ETo*, different in terms of input data requirement and climate variables combinations (Djaman et al., 2015).

Figure 2.17: Standard weather station for the measure of clime variables (https://www.campbellsci.de/wxpro).

Among these methods, it is commonly used the thermodynamic approach proposed by Monteith (1965) and subsequently modified by Allen et al. (1998) where *ETo* depends only on climate variables. The latter method is considered as one of the most accurate and assumed as the reference to calibrate other more simplified procedures (Gavilán et al., 2006; Jensen et al., 1990; Ravelli and Rota, 1999; Zhao et al., 2005).

$$ET_o = \frac{0.408\Delta(R_n - G_0) + \gamma \frac{900}{(T_{avg}+273)} U_2 (e_s - e_a)}{\Delta + \gamma(1 + 0.34U_2)} \quad (2.30)$$

where: G_0 (MJ m^{-2} d^{-1}) is the soil heat flux density, T_{avg} (°C) is the average daily air temperature at 2 m height, e_s and e_a (kPa) are the saturation and actual vapor pressure, Δ (kPa °C^{-1}) is the slope of vapor pressure curve and, finally, γ (kPa °C^{-1}) is the air psychrometric constant. For daily *ETo* estimations the heat flux density, G_0, can be neglected, because the magnitude is relatively small (Allen et al., 1998). To assess *ETo* the FAO56-PM equation (2.30) can be used by means hourly or daily climate variables. When hourly climate variables are available, it is recommended obtaining daily *ETo* as sum of hourly *ETo* values, in this way, is considered the hourly variability of the climate variables involved.

An alternative source of the ground weather data is represented by the reanalysis database. Several gridded weather and climate database, with relatively high spatial resolution but different temporal resolution have been generated and are freely downloadable at global scale. The European center for medium-range weather forecasts (ECMWF), coupling weather forecast models and data assimilation systems, periodically 'reanalyse' available past observations to create global data sets of atmospheric and land surface variables represented in 'maps without gaps. Reanalysis data, based on data assimilation are among the most used to study weather and climate variables (Parker, 2016).

Reanalysis method monitors and forecasts climate change by combing model data based on past observations from across the world for monitoring and forecasting climate change, for research, education, and commercial applications.

ERA5 and ERA5-L, provided by the ECMWF, are the last generation of the global reanalysis climate database. These databases are freely downloadable from the portal https://cds.climate.copernicus.eu/#!/home. The first dataset, ERA5, covers the entire globe from 1959 with a spatial resolution of 0.25° latitude and 0.25° longitude (about 30 km depending on the latitude) (fig. 2.18a).

The ERA5 reanalysis dataset, replacing the previous version of ERA5-Interim, produced by the Copernicus Climate Change Services (C3S). Among the available variables an estimate of the uncertainty of the database

is also available from the Copernicus program under the products "ensemble mean" and "ensemble spread" having a spatial resolution of 60 km and temporal resolution of three hours.
The second dataset, ERA5-L released in 2019 as the evolution of ERA5 dataset, aimed at enhancing the resolution of the spatial grid to 0.1° latitude and 0.1° longitude (fig. 2.18b) with a temporal cover from 1950 to present.

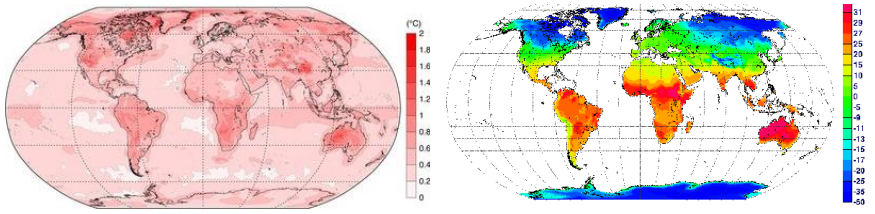

a) b)

Figure 2.18: Overall vision of the ERA5 a) (https://cds.climate.copernicus.eu/cdsapp#!/dataset/reanalysis-era5-single-levels?tab=overview) and ERA5-Land b) hourly database (https://cds.climate.copernicus.eu/cdsapp#!/dataset/reanalysis-era5-land?tab=overview).

This new version is obtained by correcting the simulated ERA5 land atmospheric variables (T_a, air humidity and pressure) using atmospheric forcing (i.e., air temperature, air humidity and atmospheric pressure) influenced by direct observations, as well as of the difference between the altitude of the forcing grid and the altitude of the higher ERA5-L resolution grid. For this new database, the uncertainty estimates are not available and then the values indicated in the original ERA5 dataset must be considered.

2.4.4 Techniques for potential and actual evapotranspiration monitoring

The potential evapotranspiration, ET_c, can be directly measured trough lysimetric techniques. This instrument simulates, at small scale, the cultivation system studied. The evapotranspirative flux measurements joint to the application of the balance mass equation allows to monitor the crop water consumption. Despite these measurements can be expensive and time consuming, historically they are considered a reliable method to obtain direct measurement of ET_c (Aboukhaled et al., 1982; Tanner, 1967). The estimation of actual evapotranspiration, ET_a, can be supported by micro-

weather measurements, provide by EC method. The EC method allows measuring the exchanges of heat, mass and momentum between a horizontal homogeneous surface and the overlying atmosphere (Foken Thomas and Aubinet, 2012).
Historically, the method was proposed by Montgomery, (1948), Swinbank, (1951), and Obukhov, (1951) under the hypothesis that the net transport between surface and atmosphere is one-dimensional and can be calculate as covariance between turbulent fluctuations of the vertical wind and the quantity if interest (water vapor, T_a, carbon dioxide, etc.).
The essential instruments necessary for an EC tower are a gas analyzer and a tridimensional sonic anemometer. In general, in a flux tower two auxiliary instruments such as 4-components net radiometer and self-calibrated soil heat flux plates are also installed (fig. 2.19).

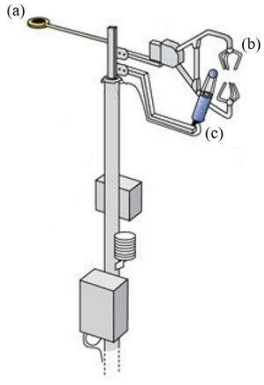

Figure 2.19: Example of Eddy covariance (EC) installation with net radiometer a) sonic anemometer b) and gas analyzer c) (https://ibis.geog.ubc.ca/~achristn/infrastructure/oakridge.html) readapted.

Gas analyzer and tridimensional sonic anemometer provide high frequency (10-20 Hz) measurements of the concentration of water vapor and carbon dioxide in atmosphere and three components of wind speed and sonic temperature, respectively. While the 4-components net radiometer and self-calibrated flux plates provide the low frequency measurements (one data every 30 min) of net radiation, R_n (W m^{-2}), and soil heat flux, G_0 (W m^{-2}), respectively. Starting from the high frequency raw data, at the end of a long data processing, the data available are the sensible, H, (W m^{-2}) and the latent, λET (W m^{-2}) heat fluxes expressed as:

$$H = \rho c_p \sigma_{WT} \tag{2.31}$$

$$\lambda ET = \lambda \sigma_{wq} \tag{2.32}$$

where: ρ (g m^{-3}) is the air density, c_p (J g^{-1} K^{-1}) is the air specific heat capacity at constant pressure and σ_{WT} (m s^{-1} K) is the covariance between vertical wind speed and air temperature, λ (J g^{-1}) is the latent heat of vaporization and σ_{wq} (g m^{-2} s^{-1}) is the covariance between vertical wind speed and the water vapor density.
Before using EC data, it is necessary to assess the quality and reliability of these data (Masseroni et al., 2013). The EB closure ratio (CR) is the method widely used for EC data quality assessment (Cammalleri et al., 2013b; Ippolito et al., 2022; Prueger et al., 2005; Wilson et al., 2002). The CR can be computed as:

$$\mathrm{CR} = \frac{H+LE}{R_n-G_0} \tag{2.33}$$

where (H+LE) are the turbulent fluxes and (R_n-G_0) is the available energy. The CR represents the slope of the regression line passing through the origin in the scatterplot between the turbulent heat fluxes, H+LE, and available energy, R_n-G_0. Ideal closure is represented by a slope equal to one, but in literature are considered acceptable CR values higher than 0.80 (Autovino et al., 2016; Er-Raki et al., 2009; Kustas et al., 1999; Saitta et al., 2020). The quality of these measurements can be compromised by anomalies generally due improper installation of the sensors or incorrect calibration, as well as the poor maintenance of sensors or data logger. Moreover, the occurrence of outliers in time series can also compromise the output quality and could generate inconsistent results mainly when model simulations are applied.

2.4.5 Machine learning algorithms to assess actual evapotranspiration

In the informatics application the ML algorithms are based on the principle of simulating human learning activities. Artificial neural networks (ANNs) are a typical ML models that can be used to solve classification and

prediction problems. The neurons are the primary element of the ANNs; these are distributed on different layers. Generally, in the ANNs there is an input and an output layer, and among these, there are the hidden layer. Based on the types of connection between neuros in the layers the ANNs can be distinguished as feedback and feedforward architecture (fig. 2.20).

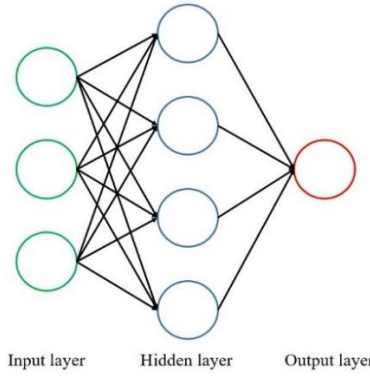

Figure 2.20: Example of feedforward artificial neural network (ANN).

In the feedback, architectures allowed the connection among the neurons of the same layer or between neurons of the previous layer. In the feedforward, architectures allowed the connections only to the neurons belonging to the next layer. Independently of the type of the ANN, three preliminary steps precede the implementation of an ANN. In the first step, choose the data that will be used as training data. In the second, choose the structure and type of the ANN and in the third the training of the ANN. To train the ANNs there are two main methods supervised and unsupervised. The supervised method compares the outputs from the ANN with a part of the data used as input; trying to minimize the difference between the network outputs and the measured target (Palani et al., 2008). Differently the previous method, in the unsupervised method, the network outputs are compared with a synthetic target.

Recently, several authors have been studied the possibility to assess ET_a using ML algorithms (Izadifar and Elshorbagy, 2010; Mosre and Suárez, 2021; Walls et al., 2020; Wang et al., 2023, 2022). For example, Izadifar et al. (2010) modelled ET_a using ANN and GP-based models in a Canadian landscape covered by spontaneous vegetation; consequently, their study does not analyze water requirements in a specific crop. The use of artificial

intelligence has also been proposed to estimate ET_a in ecosystem studies. For example, in wetland conservation for valuable and vulnerable ecosystems (Granata et al., 2020), or for studying the terrestrial water cycle in grassland ecosystems (Zhang et al., 2021). The possibility to estimate ET_a in tree crops, trough ML models, was assessed by Rojas et al. (2021), the authors estimated ET_a trough the Operational Simplified Surface Energy Balance Model (SSEBop) using as input LST with a spatial resolution of 10 m, obtained from the downscaling of the Landsat-8 LST, by means two different ML models (cubist and RF).
Among other ML models, the GPR can make predictions relying on a few parameters. The model establishes a relation between the independent input variables, x_i and the dependent variable, *y*. Specifically, the regression model can be expressed by the following relation:

$$y(x) = f(x) + \varepsilon \tag{2.34}$$

where *y(x)* is the random variable underlying the observations, *f(x)* is the Gaussian process and ε is the noisy observations of the true function expressed as a normal distribution characterized by a mean equal to zero and variance σ_n^2 estimated from the data.
The $f(x)$ can be defined by its mean *m(x)* and covariance kernel *k(x,x')* functions, represented respectively by a vector and a matrix in the form:

$$m(x) = E[f(x)] \tag{2.35}$$

$$k(x, x') = E[(f(x) - m(x))(f(x') - m(x'))] \tag{2.36}$$

The mean function of the GPR model can be assumed constant, with a value set to zero, equal to the mean of the training dataset, or using a linear function. On the other hand, the covariance kernel function can be assumed as quadratic rational, squared exponential, exponential, or using a Matern kernel value equal to 3/2 or 5/2. More details on the GPR model can be found in (Rasmussen and Williams, 2006). The best combination of *m(x)* and *k(x,x')* functions can be evaluated using the N-fold cross-validation (Mosteller and Tukey, 1968). Cross-validation is a statistical method in which the database is randomly divided into N different groups, each one containing the records corresponding to the natural number closest to 1/N.

Model validation follows an iterative procedure in which a group is used as a test set, while the other N-1 groups are used for training. The procedure is stopped after N iterations and, therefore, after using each group as the test set. This iterative statistical analysis reduces the possibility of overfitting problems (Nguyen et al., 2021) occurring when the model fits well the training data but fails in the prediction phase due to the noise or random fluctuations in the training data affecting negative the performance of the model (Namasudra et al., 2021). Thus, the model seems to make suitable predictions with the training data, while significant errors in the test data can be observed, due to the unsuitability of the model to predict new data.

Chapter 3: Materials

3.1 Climate data

The analysis was carried out considering a database of climate variables registered by a network of 39 spatially distributed ground weather stations operated by the SIAS (http://www.sias.regione.sicilia.it/) (fig. 3.1), in the decade from January 1st, 2006 to December 31st 2015, was considered, as well as corresponding data available in the ERA5-L database.

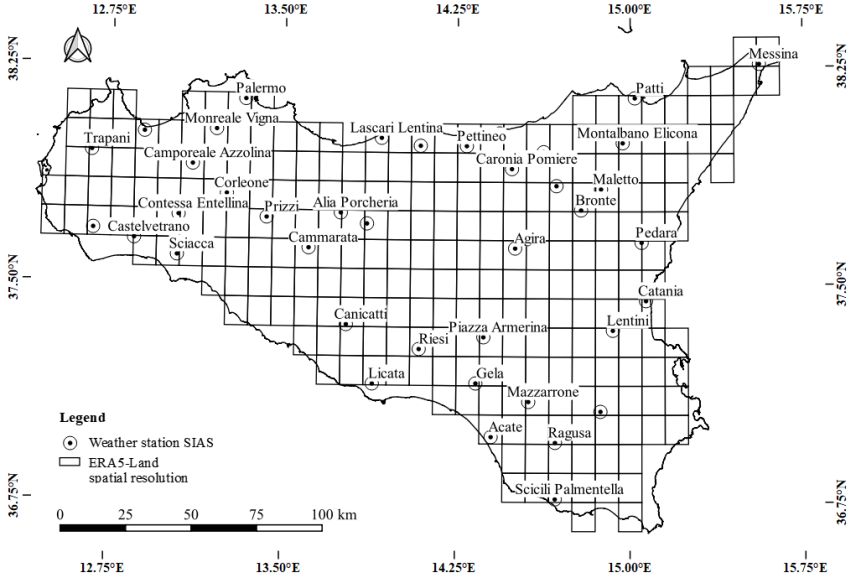

Figure 3.1: Map of Sicily with the position of SIAS weather stations and the grid of ERA5-Land database.

The data were recorded by weather stations located in positions geographically representative of different environmental conditions. This database contains all the climate variables required for the application of the FAO-56 PM equation and, specifically, daily values of minimum and maximum air temperature T_{min}, T_{max}, (°C), RH_{min}, maximum relative air humidity, RH_{max}, (%), R_s and U_2. Only 27 of the 39 weather stations contained the records of wind speed at 10 m height, U_{10}, (m s^{-1}).

For each ground weather station, table 3.1 reports the identification code (ID), the name of the station as indicated in the original database, the geographic coordinates and the elevation.

Table 3.1: Identification code (ID), name of SIAS climatic station, geographic coordinates and number of available records in the period 2006-2015.

ID	Climate station	Latitude (°N)	Longitude (°E)	Elevation (m a.s.l.)
206	Cammarata	37.6205	13.6085	350
208	Canicatti	37.3580	13.7740	475
209	Licata	37.1550	13.8888	80
213	Sciacca	37.5913	13.0398	90
216	Gela	37.1580	14.3340	70
220	Riesi	37.2750	14.0890	300
222	Sclafani_Bagni (*)	37.7050	13.8600	497
224	Bronte (*)	37.7550	14.7870	424
228	Catania	37.4430	15.0680	10
231	Maletto	37.8271	14.8732	1040
232	Mazzarrone	37.0954	14.5617	300
235	Pedara (*)	37.6436	15.0492	810
242	Piazza Armerina	37.3170	14.3670	540
245	Caronia Pomiere (*)	37.8961	14.4866	1470
246	Cesarò Vignazza	37.8380	14.6800	820
251	Messina (*)	38.2581	15.5611	421
257	Patti	38.1405	15.0195	70
258	Pettineo	37.9740	14.2900	210
259	San Fratello (*)	37.9547	14.6239	1040
262	Alia Porcheria	37.7418	13.7460	560
264	Camporeale Azzolina (*)	37.9046	13.1010	460
265	Castelbuono (*)	37.9741	14.0897	430
267	Contessa Entellina (*)	37.7299	13.0436	200
268	Corleone	37.8040	13.2510	450
271	Lascari Lentina	38.0001	13.9201	55
275	Monreale Vigna	38.0249	13.2031	630
276	Palermo	38.1300	13.3280	50
282	Acate	36.9740	14.4010	60
286	Ragusa	36.9550	14.6770	650
288	Scicili Palmentella	36.7606	14.6768	30
292	Lentini	37.3410	14.9250	50
298	Palazzolo Acreide	37.0620	14.8720	640
301	Castellammare del Golfo (*)	38.0139	12.8896	90
302	Castelvetrano	37.6470	12.8530	120
305	Mazara del Vallo	37.6791	12.6750	30
308	Trapani	37.9470	12.6620	180
309	Montalbano Elicona (*)	37.9860	14.9670	1250
311	Prizzi (*)	37.7240	13.4250	990
312	Agira	37.6230	14.5020	467

(*) climate stion without the measurement of wind speed at 10 m height

For the same period, the ERA5-L database includes the entire climate variables mentioned above, except *RH* and U_2.
To maintain the coherency between the two databases hourly data of T_a, R_s, dew-point temperature, T_{dew} (°C), and the two components (vertical and horizontal) of wind speed at 10 m height U_{v_10}, U_{H_10}, (m s^{-1}) were downloaded.

3.2 Experimental field – Villabate

The experimental field is located in a citrus orchard of about 0.40 ha close to Palermo, Sicily (38°4′ 53.4'' N, 13° 25′ 8.2'' E) (fig. 3.2). The citrus orchard (*Citrus reticulata Blanco,* cv. Mandarino Tardivo di Ciaculli) is characterized by a planting spacing of 5.0 × 5.0 m (density of 400 trees ha^{-1}, fraction cover of 48%), with plant rows roughly oriented from North-East to South-West. The trees are characterized by an average height of about 2.50 m and a maximum rooting depth of 0.50 m, with the highest root density at around 0.30 m depth. The study was carried out for the period 2018-2020.

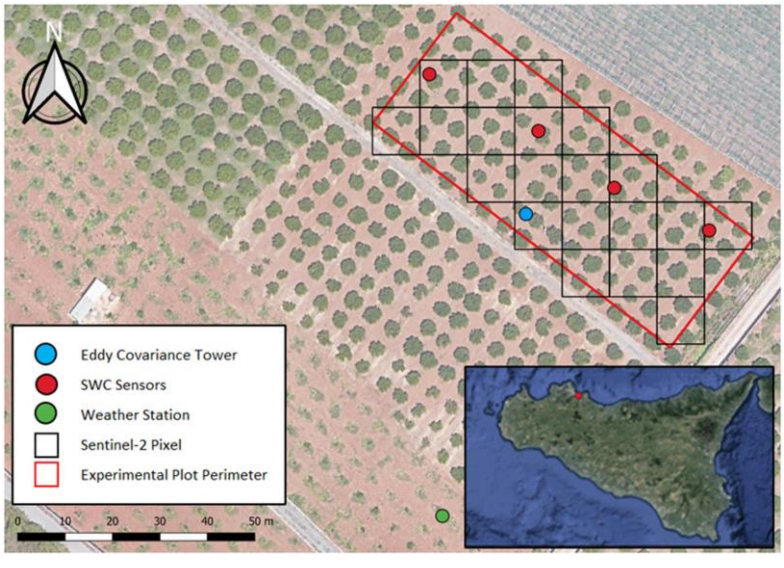

Figure 3.2: Experimental field with location of the weather station (WS), flux tower (EC) and soil water content sensors, the spatial resolution of Sentinel-2 (L2A/L2B) multispectral images is also shown.

The climate of the investigated area is the typical Mediterranean, with annual rainfall ranging between 600 and 800 mm, most of which is concentrated in fall and winter, and with cumulated crop reference evapotranspiration generally higher than 1000 mm. The average daily air temperature ranges from about 4°C in winter to a maximum of around 35°C in summer. The dominant textural class of the top soil is sandy-clay-loam with average clay, silt and sand content of 22.2%, 18.0% and 59.8%, respectively. Soil water contents at field capacity, θ_{fc}, and permanent wilting point, θ_{wp}, are equal to 0.28 cm^3cm^{-3} and 0.15 cm^3cm^{-3}, respectively. During the irrigation seasons, generally after the rainfall events, the field was characterized by the presence of temporary ground weeds (mainly *Cynodon Dactylon*, and *Boerhavia Coccinea*).

The temporal dynamic of SWC was monitored with four 0.60 m long "drill & drop" probes (Sentek Pty Ltd, Stepney, Australia), installed at a distance of 0.80 m from the tree trunks and 30 cm far from an emitter (fig. 3.2). These sensors, based on the FDR technique let to monitor SWC and temperature at 0.10 m depth intervals, up to 0.60 m, with a time-step of about 30 min. The average SWC values between the soil surface and 0.50 m depth was assumed representative of the entire root domain.

Agrometeorological data were collected by a WatchDog (WD) 2000 series weather station (Spectrum Technologies, Inc., Aurora, IL, USA) installed nearby the experimental field (fig. 3.2), which contained the sensors to measure (with a time-step of 30 min) air temperature, R_s, relative air humidity, wind speed and direction at 2 m height, and rainfall.

In 2019, an EC flux tower was also installed in the field to measure actual evapotranspiration, ET_a (fig. 3.2). The tower was equipped with a 4-component net radiometer (CNR4, Campbell Scientific Inch., Logan, Utah) installed at 3.0 m height to measure low-frequency (30 min) R_n, (W m^{-2}), a three-dimensional sonic anemometer (CSAT3-D, Campbell Scientific Inch., Logan, Utah) to measure high-frequency (20 Hz) wind speed 3D components, and an infrared open patch gas analyzer (Li-7500, Li-cor bioscience inch., Lincoln, Nebraska) to measure H_2O and CO_2 concentrations, respectively (at 20 Hz). High and low-frequency data were collected in a CR3000 datalogger (Campbell Scientific Inch., Logan, Utah) equipped with a 2 GB memory card.

Irrigation season in the area starts at the end of May and finishes around the end of September, during periods with scarce or absent precipitations. The field is irrigated with a subsurface drip system with two pipes per plant row, one on each side of the tree, at 1.1 m from the trunks. The lateral pipes contain co-extruded emitters discharging 2.3 l h^{-1} at a pressure of 100 kPa with a spacing of 1.0 m (i.e., 10 emitters/tree). The adopted irrigation strategy, accounting for the actual climate conditions, was designed to define moderate crop water stress only during phase II of vegetative growth (initial fruit enlargement phase), generally between July 1 and August 15. A total of three watering of about 56 m^3 ha^{-1} were scheduled per week, except for the period of water restrictions, in which only two irrigation events per week were scheduled.

An extended database of high-resolution MSI retrieved from the Sentinel-2 twin satellites (L2A/L2B) were acquired (https://scihub.copernicus.eu/dhus/#/home) to monitor, over the study area, the spatio-temporal variability of NDVI and NDWI VIs. The scenes downloaded containing the whole experimental site were N0208_R079_T33SUC and N0208_R122_T33SUC (fig. 3.3a,b).

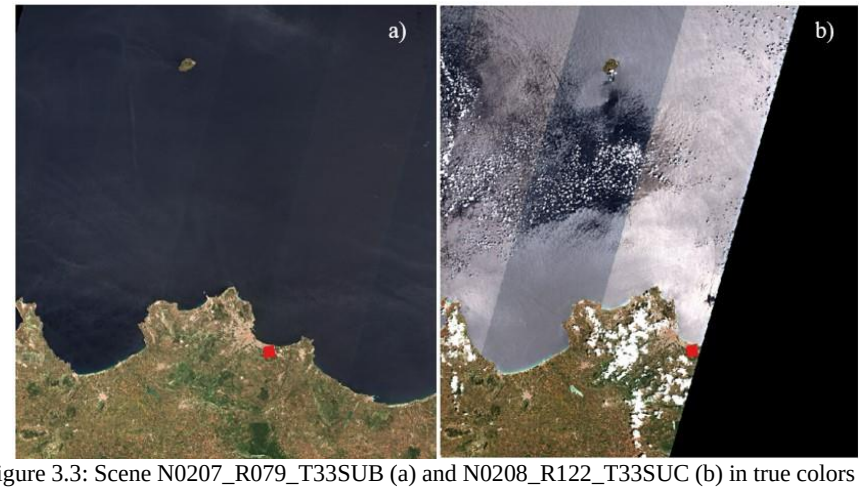

Figure 3.3: Scene N0207_R079_T33SUB (a) and N0208_R122_T33SUC (b) in true colors with identification of the study area, related to the acquisition dates 2-06-2018 and 3-06-2018.

These products are calibrated in reflectance at the Bottom of the Atmosphere (BoA), orthorectified and corrected for the atmospheric effects (Main-

Knorn et al., 2017). The images have a spatial resolution of 10 m in the VIS–NIR regions and 20 m in the SWIR region, with a temporal resolution of approximately 5 days when considering both satellites (2A and 2B satellites). For the three years, a total of 193 scenes were selected under clear-sky conditions, downloaded, and preprocessed using the R library named "sen2r" (Ranghetti et al., 2020).

3.3 Irrigation District 1A – Castelvetrano

From a climate standpoint, the study area of Castelvetrano is characterized by a wet season from September to April and a dry season from April to September. On average, the total annual rainfall is variable between 450 and 1000 mm concentrated during the autumn-winter period and the duration of the dry season is about five months, from the second half of April to the beginning of September. The typical values of annual *ETo* are slightly higher than 1000 mm. The study area is represented by the irrigation district 1A of the Garcia-Arancio district (fig.3.4) managed by the "Consorzio di Bonifica Sicilia Occidentale" (ex Consorzio di Bonifica Agrigento 3) which includes the territories of municipalities of Sambuca di Sicilia, Sciacca, Menfi, Santa Margherita Belice, Partanna and Castelvetrano. The waters used for irrigation purposes are those stored in the artificial reservoirs Garcia and Arancio, which are characterized by a reservoir capacity of 61.0 and 24.2 Mm^3, respectively. The two tanks are interconnected by an adduction pipeline with an overall length of about 46 km, which allows the transfer of volumes from Lake Garcia to the Arancio reservoir by gravity. From the Garcia-Arancio tank split up two distribution pipes called "Diramazione Est" and "Diramazione Ovest", with a diameter of Ø 1600 mm and Ø 2000 mm, respectively, these supply the header tanks by gravity or pumping, which supply the irrigated areas divided according to altimetry zone.
The district 1A (fig. 3.5), falls on the northern side of the irrigated area and covers a surface of about 2745 ha. To deliver water from reservoir to hydrants a dense pipe-network extending approximately 214 km was implemented. The network is divided into main, secondary, and tertiary pipelines with different materials steel, glass fiber reinforced plastic (PRFV), asbestos cement and polyvinyl chloride (PVC). Irrigation network is fed, by gravity, by two loading reservoirs, the first of which named 1/A1

has a volume about 24,000 m^3 located at about 240 m a.s.l., the second, named 1A/2, placed at 190 m a.s.l. characterized by a volume of about 27,000 m^3. Water derived from the main adductor of the Garcia lake is pumped into two reservoirs by a set of pumps working with variable speed drive installed at the "Zangara" pumping station.

The distribution network servers 139 sectors for more than 2,000 water users. In each irrigation sector, water distribution is performed by turns, that means that the whole flow is diverted to the hydrants follow a fixed turn. Hydrant discharge equals to 15 l s^{-1}, with a minimum pressure of 2.5 bar. Volumetric water consumptions in each sector are controlled and registered by a central control unit. The most common farm distribution system in sprinkler and drip irrigation.

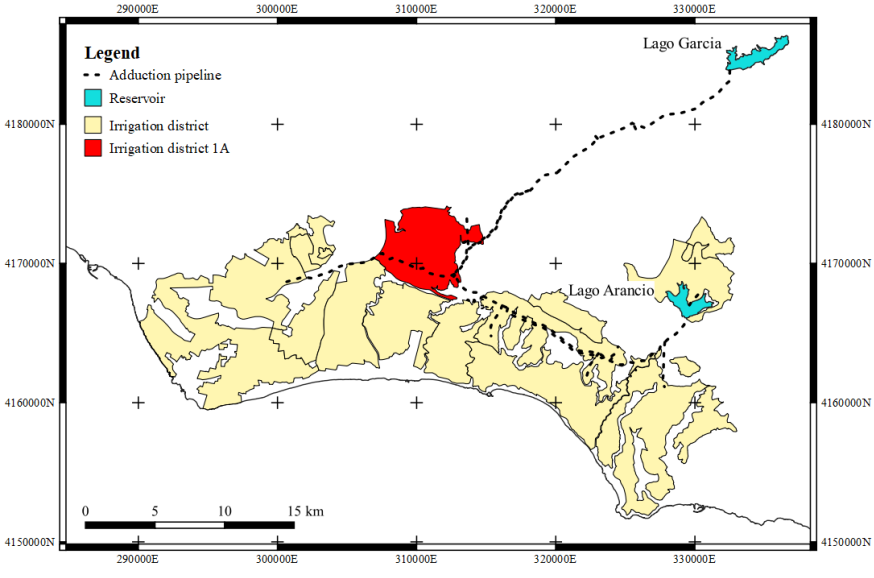

Figure 3.4: Irrigated areas of ex "Garcia-Arancio" district and study area irrigation district 1A (in red).

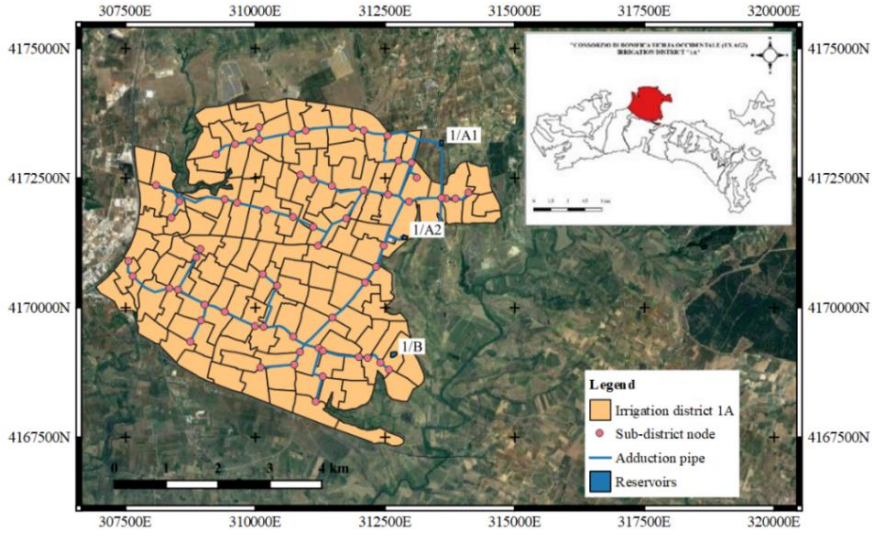

Figure 3.5: Irrigation district 1A.

The area is predominantly cultivated with olive (cv. "*Nocellara del Belice*") orchards (70%), vineyards (24%) with sporadic presence of citrus (2.6%) being other horticultural (3.4%) crops sporadic. The soil characterization was carried out using the pedological map Bono, (1998) (fig.3.6), in which are indicated the pedological types.

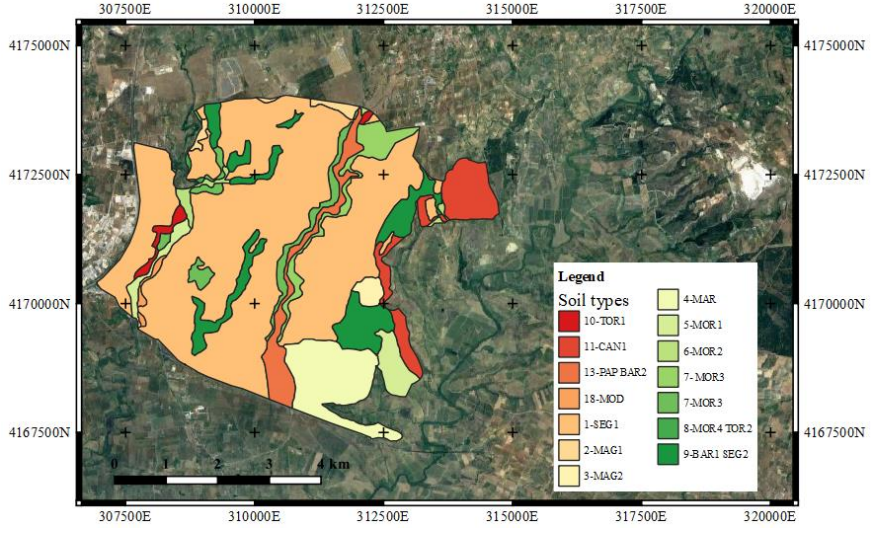

Figure 3.6: Pedologic map of the study area (Bono et al., 1998).

The prevalent type of soil is “Seggio (SEG1)” that covers 1786 ha, about the 60 % of the total area.

Table 3.2 shows the soils granulometric composition and the depth of the different soils type. According to the Unite State Department of Agriculture (USDA), the prevalent types of soil are characterized by medium mixture sand-clay with an average depth of about 0.85 m. The soil depth where the root are main developed was variable from 0.30 m to 1.25 m. Based on the soil texture, the coefficient α and *n* of the soil water retention curve are shown in table 3.3. These were obtained by means the pedo-transfer function implemented in the software “ROSETTA” (Schaap et al., 2001) using the soil granulometric composition showed in table 3.2.

Within the perimeter of the irrigation district 1A is located a weather station (ID 302 Castelvetrano) (fig. 3.5) managed by the SIAS. This station registers at hourly time step, data of the main climate variables, such as air temperature, R_s, relative air humidity, wind speed and direction at 2 m and 10 m height, and rainfall. The station is equipped with a CR1000 datalogger (Campbell Scientific Inch., Logan, Utah), two wind speed sensors Gill Windsonic (Gill Instruments Limited, Lymington, Hampshire, UK) installed at 2 m and 10 m above the soil and a thermo-hygrometer HMP45 (Vaisala Oyj, Helsinki, Finland).

Table 3.2: Size distribution of the soil within the irrigation district 1A.

SOIL	TEXTURE	PARTICULAR SIZE DISTRIBUTION			DEPTH
		Clay [%]	Silty [%]	Sand [%]	[cm]
Seggio (SEG1)	loam-sandy-clay	10.28	24.20	65.52	85
Marzuchi (MAR)	loam-sandy-clay	35.43	17.65	46.93	90
Morici (MOR1)	loam-silty	10.44	51.41	38.15	100
Morici (MOR2)	loam	15.80	38.24	45.96	30
Morici (MOR4)	loam	19.54	33.24	47.22	80
Torre (TOR1)	loam-sandy	5.41	35.37	59.22	30
Torre superficiali (TOR2)	loam	19.54	33.24	47.22	80
Canotta (CAN1)	clay	41.07	41.44	17.49	120
Papa (PAP)	loam-sandy-clay	27.44	27.22	45.35	125
Barone (BAR2)	loam-sandy	18.50	13.50	68.00	75
Modione (MOD)	loam-clay	21.37	39.00	39.63	110

Table 3.3: Soil water retention curve coefficients estimate by means “ROSETTA” software (Schaap et al., 2001).

SOIL	θ_s [$cm^3\ cm^{-3}$]	θ_r [$cm^3\ cm^{-3}$]	α [cm^{-1}]	α [cm^{-1}]	θ_{fc} [$cm^3\ cm^{-3}$]	θ_{wp} $cm^3\ cm^{-3}$]
Seggio (SEC1)	0.39	0.11	0.0334	1.2067	0.28	0.19
Marzuchi (MAR)	0.39	0.11	0.0334	1.2067	0.28	0.19
Morici (MOR1)	0.44	0.06	0.0051	1.6626	0.29	0.09
Morici (MOR2)	0.30	0.06	0.0111	1.4737	0.24	0.09
Morici (MOR4)	0.40	0.06	0.0111	1.4737	0.24	0.09
Torre (TOR1)	0.39	0.04	0.0347	1.7466	0.10	0.05
Torre superficiali (TOR2)	0.39	0.04	0.0347	1.7466	0.10	0.05
Canotta (CAN1)	0.46	0.09	0.0150	1.2529	0.33	0.19
Papa (PAP)	0.39	0.11	0.0334	1.2067	0.28	0.11
Barone (BAR2)	0.39	0.04	0.0347	1.7466	0.10	0.02
Modione (MOD)	0.44	0.07	0.0158	1.4145	0.26	0.12

The volumes delivered in each hydrant located within the sector are registered on a paper format user card. For each user, the employees of the consortium, registers in a paper the information to draw up an effective irrigation plan. Each form are reports information regarding the location of the farms in the district, the number of the sector, the crop type, the farm extension, the date, and the volume of the water delivered (fig. 3.7).

Figure 3.7: Example of the paper sheet referred to one user.

For the whole district, the MSI Sentinel-2 level 2A product were acquired and, in particular, the scene N0207_R079_T33SUB, (fig. 3.8). For the period from 01-03-2018 to 31-12-2020 were acquired 68 scenes, in clear sky condition.
For the period 01-01-2009 to 31-12-2011 and same area, MODerate resolution Imaging Spectroradiometer (MODIS) MCD43A3, Version 6 product (MCD43A c006) were also acquired. This product provides nadir reflectance at different wavelengths; with a spatial resolution equal to 500 m, in particular ρ_{nir}, ρ_{red} and ρ_{swir} were detected respectively in band B1 ranging from 620 to 670 nm, in band B2 ranging from 841 to 876 nm and in band B6, from 1628 to 1652 nm.

Figure 3.8: Scene N0207_R079_T33SUB in true colors with identification of the study area.

3.3.1 Experimental field – Castelvetrano

The experimental field "Tenuta Rocchetta" showed in figure 3.9, is represented by an olive orchard (cv. "Nocellara del Belice") extended about 6 ha (figure 3.9). The field, located in the South-West of Sicily, Italy (37°38'61'' N, 12°50'53'' E), about 5 km far from the town of Castelvetrano, is part of irrigation district 1A (fig.3.5) characterized by a flat landscape and rather homogeneous soil and crop types. The plants within

the experimental field a height of about 3.50 m and are spaced according to a regular grid 5.0 × 8.0 m (density of about 250 trees ha^{-1}).
The climate of the area is Mediterranean, with precipitation events mainly concentrated during autumn and winter and high air temperature in summer with sporadic precipitation events.
In the eastern side of this area, about 500 m is located a standard weather station (ID=302) of the SIAS, presented in section 3.1.

Figure 3.9: Map of the experimental field with the position of the EC tower and the SIAS weather station; the MODIS (MCD43A v006) pixel containing the experimental field is also shown.

The temporal dynamic of the evapotranspiration flux, at field scale, was monitored by means of an EC tower installed in the left side of the experimental field located within the farm (fig. 3.9). The EC flux tower was installed in April 2009 equipped with a 4-component net radiometer (CNR4, Campbell Scientific Inch., Logan, Utah) installed at 8.50 m height to measure low-frequency (30 min) R_n, (W m^{-2}) a three-dimensional sonic anemometer (CSAT3-D, Campbell Scientific Inch., Logan, Utah) to measure high-frequency (20 Hz) wind speed 3D components, and an infrared open patch gas analyzer (Li-7500, Li-cor bioscience inch., Lincoln,

Nebraska) to measure H_2O and CO_2 concentrations, respectively (at 20 Hz) positioned at 7.00 m and two self-calibrated flux plates (HFP01SC, Hukseflux) placed, respectively, in the exposed and shadowed bare soil, at a depth of about 0.10 m. High and low-frequency data were collected in a CR5000 datalogger (Campbell Scientific Inch., Logan, Utah) equipped with a PCMCIA 2 GB memory card. Irrigation water is supplied by a drip irrigation system (four 8 l h^{-1} emitter/plant). For the experimental field, hourly data of air temperature, T (°C), R_s (W m^{-2}), T_{dew}, and, U_{10} (m s^{-1}), were also downloaded from the ERA5-L database (Muñoz Sabater, 2019), available in the climate change service portal provided by Copernicus (https://cds.climate.copernicus.eu/cdsapp#!/home).

Chapter 4: Methods

4.1 FAO56 Penman-Monteith equation to estimate crop reference evapotranspiration

Using the databases SIAS and ERA5-L, the FAO56-PM equation (Allen et. Al., 1998) was applied to estimate hourly crop reference evapotranspiration, *ETo*. The ERA5-L database includes all the climate variables necessary to estimate *ETo* by means FAO56-PM equation, except U_2. Therefore, to maintain the coherency between the two databases, as well as to avoid possible uncertainty due to the assumption of logarithmic wind profile (Newman and Klein, 2014), *ETo* was calculated considering all climate variables at 2 m height and only wind speed at 10 m height.
In the ERA5-L database the hourly relative air humidity, *RH*, (%), is not available, therefore was calculated as suggested in the FAO56 paper (Allen et al., 1998).

$$RH = 100 \frac{e_a(T_{dew})}{e_s(T)} \tag{4.1}$$

where $e_a(T_{dew})$ and $e_s(T)$ are the actual and saturation vapour pressure corresponding at, T_{dew}, and actual air temperature, T, respectively.
A Matlab® script was generated to localize the grid cells, to aggregate the hourly ERA5-L climate data at daily time-step except for the already available daily R_s and, finally to estimate daily *ETo*. The examined database is complete and, for the period 2006-2015, contains 3652 records for each variable.
For each daily climate variable, the comparison between the values measured by SIAS and retrieved by ERA5-L database was carried out by assuming intercept-free linear regression. The slope of the regression line, b, was used as a measure of accuracy, while the R^2, was considered as a measure of precision (Sentelhas et al., 2010).
The daily S_c, associated to each generic variable v_i, was calculated based on the partial derivative of *ETo* to v_i, transformed into a non-dimensional form (McCuen 1974; Beven 1979), as:

$$S_{ci} = \frac{\partial ET_0}{\partial vi} \frac{vi}{ET_0} \quad (4.2)$$

where: *∂ETo* is the variation of reference evapotranspiration caused by the change associated to the variable, *∂vi*. The partial derivatives, needed for to evaluate daily S_{ci}, were calculated using symbolic calculation tool of Matlab®. Yearly average S_c was obtained by averaging daily values.
The total error referred to the *ETo* estimation was obtained as the sum of the individual error of each variable, E_i, calculated by the following equation:

$$E_i = \left((b-1)S_{ci}\right) \cdot 100 \quad (4.3)$$

where: *b* indicates an eventual underestimation or overestimation, and S_{ci} is the sensitivity coefficient referred to the single variable, which indicates how *ETo* is sensitive to the single variables used to assess *ETo*.

4.2 Estimation of actual evapotranspiration based on Gaussian Process Regression (GPR) algorithm

To estimate the missing data in the ET_a time series, the GPR (Rasmussen and Williams, 2006) model was used for its power, among other ML algorithms, to make predictions relying on a few parameters.
To identify the best *m(x)* and *k(x,x')* functions, the ML model based on the GPR was implemented by using a Matlab® script, which was used to test fifteen possible combinations of the mean and covariance kernel functions (3 mean functions and 5 covariance kernel functions). This analysis was carried out by considering the complete dataset of the input variables acquired in the Villabate experimental field including i) the weather variables used to estimate crop reference evapotranspiration *ETo* (R_s, T_a, *RH* and U_2); ii) the SWC, expressive of the soil water status and iii) two VIs, such as NDVI and NDWI, accounting for the characteristics of the vegetation, with impact on the crop coefficient (Lei and Yang, 2014; Pôças et al., 2020).
Once identified the best *m(x)* and *k(x,x')* functions, four additional combinations of the input variables were considered to reduce the computational burden.

Table 4.1 summarizes the combinations of the investigated variables used as input, to run the model for the citrus orchard.

The first combination contains the complete dataset that was also used to select the *m(x)* and *k(x,x')* functions. The second and the third combinations excluded, respectively, the VIs, and the SWCs, whose values are not always available. The fourth combination considers only the agrometeorological variables, whereas the last combination included only variables acquired from remote platforms and available online, such as the agrometeorological variables and the VIs retrieved from the ERA5-L and Sentinel-2, respectively.

Further assessment of the suitability of the GPR algorithm was carried out for the olive orchard, located in the irrigation district 1A, by considering only the last three variables combination due to the unavailability of SWC measurements. However, considering that for the examined period in which operated the EC tower (2009-2011) the Sentinel-2 images were not available, the MODIS images were considered to estimate the VIs used as input for combinations 3 and 5.

The best combination of *m(x)* and *k(x,x')* functions, as well as the performances associated with the other variables combinations, were evaluated using the N-fold cross-validation (Mosteller and Tukey, 1968). In this study, the N value was set up as five and therefore 80% of the entire database was used for training while the remaining 20% was used for testing purposes. The suitability of *m(x)* and *k(x,x')* functions, as well as the performance of the GPR model with the other four different variables combinations were assessed based on the following statistical indicators: i) the RMSE, ii) the R^2, iii) the MAE, v) the Nash Sutcliffe Efficiency (NSE) coefficient. The statistical indicators were evaluated as the mean of all the N performed iterations.

Table 4.1: Different combinations of input variables.

Variables' combination	Input	Tool	Symbol	Unit
1	Global Solar Radiation	WatchDog 2000	R_s	[W m^{-2} d^{-1}]
	Air Temperature		T	[°C]
	Relative Air Humidity		RH	[%]
	Wind Speed		W_{s2}	[m s^{-1}]
	Normalized Difference Vegetation Index	Sentinel-2	NDVI	[-]
	Normalized Difference Water Index		NDWI	[-]
	Soil Water Content	Drill and Drop	SWC	[cm^3 cm^{-3}]
2	Global Solar Radiation	WatchDog 2000	R_s	[W m^{-2} d^{-1}]
	Air Temperature		T	[°C]
	Relative Air Humidity		RH	[%]
	Wind Speed		W_{s2}	[m s^{-1}]
	Soil Water Content	Drill and Drop	SWC	[cm^3 cm^{-3}]
3	Global Solar Radiation	WatchDog 2000 or SIAS	R_s	[W m^{-2} d^{-1}]
	Air Temperature		T	[°C]
	Relative Air Humidity		RH	[%]
	Wind Speed		W_{s2}	[m s^{-1}]
	Normalized Difference Vegetation Index	Sentinel-2 or MODIS	NDVI	[-]
	Normalized Difference Water Index		NDWI	[-]
4	Global Solar Radiation	WatchDog 2000 or SIAS	R_s	[W m^{-2} d^{-1}]
	Air Temperature		T	[°C]
	Relative Air Humidity		RH	[%]
	Wind Speed		W_{s2}	[m s^{-1}]
5	Global Solar Radiation	ERA5-Land	R_s	[W m^{-2} d^{-1}]
	Air Temperature		T	[°C]
	Relative Air Humidity		RH	[%]
	Wind Speed		W_{s2}	[m s^{-1}]
	Normalized Difference Vegetation Index	Sentinel-2 or MODIS	NDVI	[-]
	Normalized Difference Water Index		NDWI	[-]

4.3 Experimental field – Villabate

4.3.1 Evaluation of vegetation indices

The availability of high-resolution MSI from the ESA Sentinel-2 mission has allowed the easy computation of VIs based on VIS–NIR wavelength, as NDVI (Rouse et al., 1974), and in additional on SWIR region. For the experimental field, the use of the SWIR region with the NDWI has the advantage to be sensitive to the surface water content (Gao, 1996).
Considering the different spatial resolutions associated with NIR and SWIR, to evaluate NDWI, the values of reflectance related to four pixels corresponding to the NIR domain were associated with a single pixel reflectance in the SWIR.
The wavelengths, for Sentinel-2A and 2B satellites, are centered at 664.6 nm and 664.9 nm for the red band (B4), at 832.8 nm and 832.9 nm for NIR (B8) and 1613.7 nm and 1610.4 nm for SWIR (B11), respectively.
For the considered period (2018–2020), after selecting the Sentinel-2 clear-sky images, a gap-filled database of daily NDVI and NDWI maps was generated using a linear interpolation technique (Pan et al., 2017) implemented in Matlab® 2021b and then exported in Quantum Gis (QGis) (release 3.4.3) environment.

4.3.2 Calibration of crop coefficient - vegetation indices functional relationship to estimate actual evapotranspiration by means FAO56 Agro-Hydrological model

A K_c(VIs) non-linear relationship was initially identified by using an extended time series of MSI retrieved by the Sentinel-2 platform combined with a set of field micro-meteorological measurements. For the investigated orchard, the proposed K_c(VIs) relationship allowed obtaining a *priori* a database of daily K_c maps characterized by high spatial resolution (10 m).
The empirical relationship was obtained in the absence of crop water stress and, therefore, on days in which SWC in the orchard resulted higher than 0.21 cm^3cm^{-3}, which was identified as the θ^*, and crop water stress occurs in the orchard under it (Franco et al., 2022).

The database of daily K_c maps was then used as input for the FAO56 model to estimate the spatio-temporal variability of actual evapotranspiration, ET_a, as well as the other terms of SWB in the root zone.
According to the single crop coefficient approach proposed in the FAO56 paper (Allen et al., 1998) the value of actual evapotranspiration can be defined as:

$$ET_a = K_c K_s ET_o \tag{4.4}$$

where: K_c is the crop coefficient obtained through the predictive relationship based on VIs, K_s is the stress coefficient and *ETo* is the crop reference evapotranspiration.
In this study, according to the FAO56 paper (Allen et al., 1998), K_s is expressed as a linear function of the soil water depletion, D, (mm) (eq. 2.13). At the daily time-step, the SWB in the root zone, Z_r (m), was computed by means equation (2.6).
The net precipitation was calculated by reducing the gross precipitation *P* (mm) of the canopy interception, P_{int} (mm), estimates as suggested by Braden (1985).

$$P_{int} = \alpha \mathrm{LAI}\left(1 - \frac{1}{1+\frac{bP}{\alpha \mathrm{LAI}}}\right) \tag{4.5}$$

where: α is an empirical conversion coefficient and *b* is the soil cover fraction, corresponding to about LAI/3. For ordinary crops, α=0.25.
Model simulations to estimate daily values of SWC and ET_a, were carried out during three irrigation seasons, from Day Of the Year (DOY) 137 to 273, considering as initial SWC the corresponding measurement. Table 4.2 summarizes the values of the input variables assumed for the simulations and the related data sources.

Table 4.2: Values for the variables used for FAO56 model simulations.

Variable	Units	2018	2019	2020	Data source
$\theta_{fc\backslash}$	[cm^3cm^{-3}]	0.28	0.28	0.28	measured
θ_{wp}	[cm^3cm^{-3}]	0.15	0.15	0.15	measured
θ_0	[cm^3cm^{-3}]	0.20	0.23	0.24	measured
θ^*	[cm^3cm^{-3}]	0.21	0.21	0.21	fixed
Z_r	[m]	0.50	0.50	0.50	fixed

4.4 Irrigation district 1A – Castelvetrano

4.4.1 Estimation of basal crop coefficient based on fractional cover and canopy height

To estimate the basal crop coefficient, K_{cb}, in the irrigation district, due the absence during the analysis period (2018-2020) of ET_a measurements, it was not possible to apply the methodology proposed in the Villabate citrus orchard. For this reason, it was applied the procedure based on fractional vegetation cover, f_c, and canopy height, h_{crop}, suggested by Allen and Pereira (2009).

Initially, a functional relationship was calibrated between f_c and NDVI. For this purpose two polygons databases were identified, the first for the calibration K_c(NDVI) relationship and the second one for his validation.

The first database contains 20 polygons in which are contained 100 plants, while the second contain 12 polygons characterized by the same number of the plants (fig. 4.1). Figure 4.1 shows the two databases, red for the calibration and blue for the validation. For both databases, the fraction cover, f_c, during the intermediate phase of the phenological cycle of the crop was estimated by means aerial images available on the Google Earth Pro® platform version 7.3.4.8642 (GEP), referring to the month of July 2019. During the studied period, the frequent operations performed by farmers, allow to recognize, and assume the absence of weed vegetation on the soil surface. The value of f_c in the different plots was obtained as the ratio between the total area occupied by the plants and the extension of the plot examined (fig 4.2). The total area occupied by the plants of a single plot was obtained vectorizing the surface canopy of about 25% of the trees present,

retrieving the average total area occupied by the plants and multiplying this for the number of the plants inside the plot.

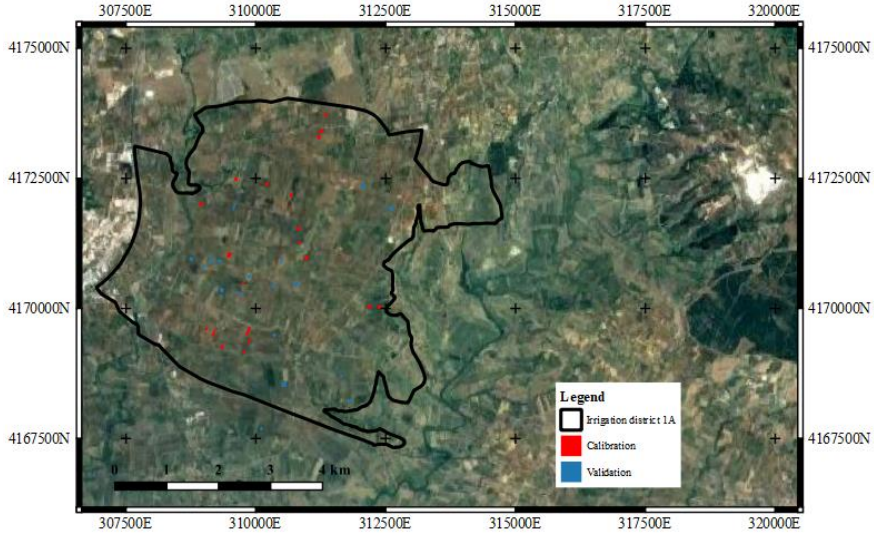

Figure 4.1: Polygons used for calibration (red areas) and validation (blue areas).

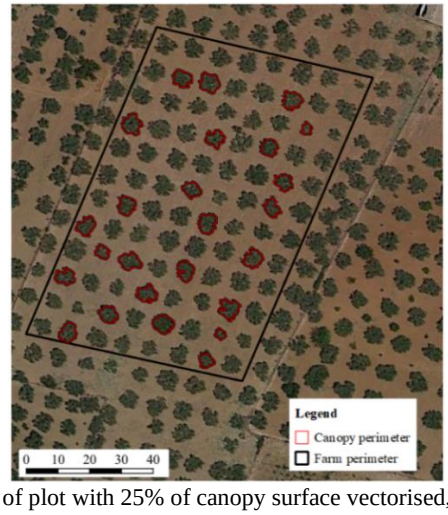

Figure 4.2: Example of plot with 25% of canopy surface vectorised, used for calibration of predictive relationship fc-NDVI.

The spatio-temporal variability of the VIs was investigated using Sentinel-2 MSI level 2A. The images were downloaded and pre-processed using the

R package toolbox "sen2r" (Ranghetti et al., 2020). For the irrigation district 1A, in 2019, four available clear-sky Sentinel-2 scenes were selected: two images the days before the aerial image of GEP, and two after. Table 4.3 shows the dates and the images available for the examined period.

Table 4.3: Clear-sky Sentinel-2 available scenes and date of GEP aerial image referred to the study area

Google Earth Pro	04/07/2019
Sentinel-2	07/06/2019 02/07/2019 22/07/2019 01/08/2019

For the four images available the NDVI was calculated based on the relationship suggested in Rouse et al. (1974).
Then, for each plot, using the "zonal statistic" tool of QGis software, were retrieved the mean and the standard deviation values of NDVI. Finally, the representative value for the plot was obtained as the mean of the four images. Based on the f_c and NDVI values, a functional relationship was found. This relationship was used as input to implement A&P procedure, while the other terms were set based on values found in literature. Table 4.4 summarizes the values of variable used to run the A&P procedure, as well as the corresponding refence source.

Table 4.4: Values of variable used to run the A&P procedure

Variable	Unit	Value	source
M_L	[-]	1.50	(Allen and Pereira, 2009)
h_{crop}	[m]	4	(Rallo et al., 2021)
k_h	[-]	0.10	(Allen and Pereira, 2009)
K_{cb_cover}	[-]	0	fixed
r_c	[s m^{-1}]	600	(Autovino et al., 2006)

In order to obtain a functional relationship K_{cb}(NDVI), the K_{cb} obtained with the A&P procedure were correlated with NDVI values. Figure 4.3 shows the flow chart used to obtain the functional relationship K_{cb}(NDVI).

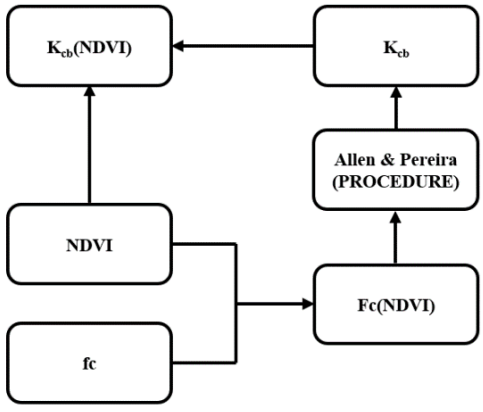

Figure 4.3: Functional relationship K_{cb}(NDVI) calculation flow chart.

4.4.2 Implementing the spatially distributed FAO56 model

The implementing of spatially distributed FAO56 Agro-Hydrological model was carried out using the Matlab® images processing tool library. The model was applied on several farms, identified by the Web Map Service (WMS) provide by "Agenzia delle Entrate" (https://www.agenziaentrate.gov.it) joint with the personal data of owners. The farms identify, for privacy reasons, were coded using an alphanumeric encoding (fig. 4.4).

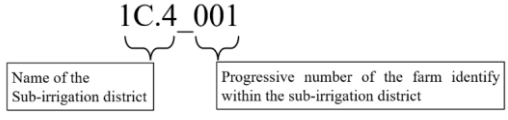

Figure 4.4: Example of the farm encoding.

In figure 4.4, the combination before the underscore defines the sub-irrigation district, while the number after the underscore the progressive number of a farm within the sub-irrigation district.
The figure 4.5 shows the general flow chart developed to use the FAO56 agro-hydrological model at distributed spatial scale. The NDVI, θ_{fc} and θ_{wp} inputs are in raster format whereas the weather data such as crop reference evapotranspiration, *ETo*, and rainfall are expressed like a single lumped value; all input are referred at daily time scale.

The flow chart (fig. 4.5) shows two different model modes, the first is named WRM, and the second, WUM. The first function based on the irrigation management parameters, allows the irrigation scheduling by identifying the time and the volume of irrigation. The second allows the crop water requirements estimation using the farmer irrigation data. A total of 91 farms distributed in 67 olives, 14 vineyards, 3 citrus orchards and 7 mixed crops.

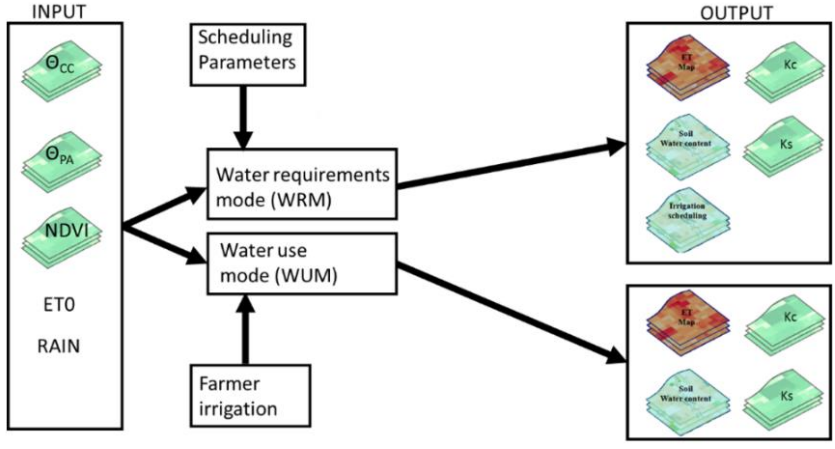

Figure 4.5: Schematization of spatially distributed FAO56 Agro-Hydrological model.

With reference to the 67 olives farms, figure 4.6 shows the farms used in WUM (green surfaces) and in WRM (blue surfaces). to obtain the farmers' management parameters and to estimate crop water requirements, respectively.

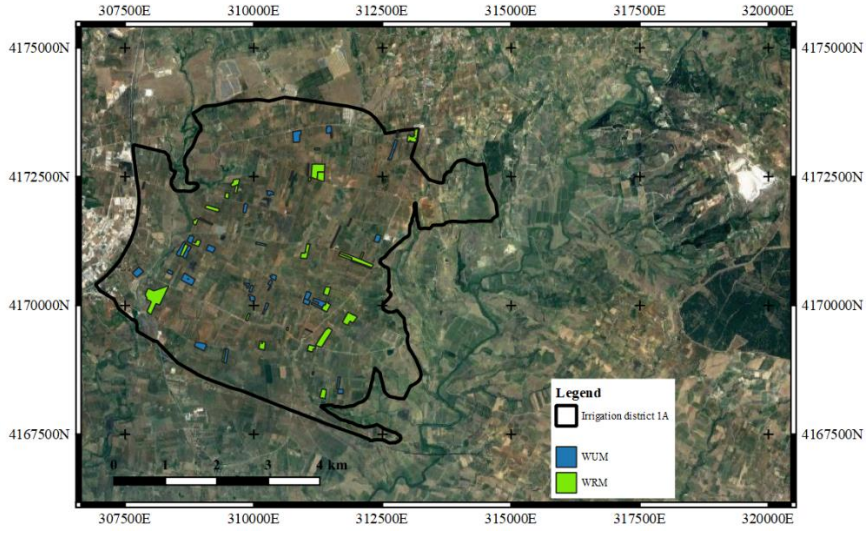

Figure 4.6: Spatial distribution of 67 olives orchards divided in calibration (blue) and validation (green) surfaces.

4.5 Statistical indicators for model validation

The model performance was evaluated based on the goodness-of-fit indicators used to assess the matching between measured and estimated SWC and actual evapotranspiration:
RMSE, whose target value is zero when there are no differences between simulated and observed values.

$$\mathrm{RMSE} = \sqrt{\frac{\sum_{i=1}^{N}\left(y_{,i}-x_{,i}\right)^{2}}{n}} \tag{4.6}$$

where: y_i is the predicted value of the i-th sample and x_i is the corresponding measured value and n is total number of observations..
Mean Bias Error (MBE), whose target value is zero; a positive value indicates that simulated values are overestimated, while a negative value indicates the model underestimation (Kennedy and Neville, 1986).

$$\mathrm{MBE} = \frac{\sum_{i=1}^{n}\left(y_{,i}-x_{,i}\right)}{n} \tag{4.7}$$

where: y_i is the predicted value of the i-th sample and x_i is the corresponding measured value and n is total number of observations.
MAE, represent the distance between the predicted and observed values, with a target of zero.

$$\mathrm{MAE} = \frac{\sum_{i=1}^{n}|y_{,i}-x_{,i}|}{n} \tag{4.8}$$

where: y_i is the predicted value of the i-th sample and x_i is the corresponding measured value and n is total number of observations.
Slope of regression line, b, whose target value is one, represents the angular coefficient of the regression line between simulated and observed variables forced to the origin.

$$b = \frac{\sum_{i=1}^{n} y_i x_i}{\sum_{i=1}^{n} x_i^2} \tag{4.9}$$

where: y_i is the predicted value of the i-th sample and x_i is the corresponding measured value.
R^2, whose target value is one indicating that the variance of the observed values is explained by the model (Eisenhauer, 2003).

$$R^2 = 1 - \frac{\sum_{i=1}^{n}(y_i-x_i)^2}{\sum_{i=1}^{n}(y_i-\bar{x_i})^2} \tag{4.10}$$

where: y_i is the predicted value of the i-th sample and x_i is the corresponding measured value and $\overline{x}$ is the mean of measured data for a total n observations.
The Percent Bias (PBIAS), whose target value is zero, and positive values are associated with the model underestimation, while negative values indicate the model overestimation.

$$\mathrm{PBIAS} = 100\frac{\sum_{i=1}^{n}(y_i-x_i)}{\sum_{i=1}^{n} x_i} \tag{4.11}$$

where: y_i is the predicted value of the i-th sample and x_i is the corresponding measured value.
NSE, whose target value is one; values between 0.0 and 1.0 indicate an acceptable model performance, whereas negative values indicate that the

mean of observed values is a better predictor than the simulated values and, therefore, unacceptable performance (Nash and Sutcliffe, 1970).

$$\mathrm{NSE} = 1 - \frac{\sum_{i=1}^{n}(y_i x_i)^2}{\sum_{i=1}^{n}(x_i - \overline{x})^2} \tag{4.12}$$

where: y_i is the predicted value of the i-th sample, x_i is the corresponding measured value and $\overline{x}$ is the mean of measured data for a total n observation.

Chapter 5: Results and Discussion

5.1 Comparison between ground weather stations (SIAS) and ERA5-Land reanalysis climate variables

The preliminary analysis on the consistence of the dataset highlighted that, in the decade 2006-2015, the examined climatic stations included a percentage of daily records containing all the variables required by FAO56-PM equation higher than 85% except for the weather stations with ID 235, 345 and 311 for which this percentage is equal to 74%, 78% and 79%, respectively. However, it was verified that the short periods with the occurrence of missing data, randomly distributed during the seasons and the years and it, did not affect the statistical analysis.

As an example, figure 5.1 shows the scatterplots of daily climate variables (T_{min}, T_{max}, R_s, RH_{min}, RH_{max}, U_{10}) retrieved from ERA5-L dataset versus the measured ones by SIAS for the weather stations of Canicattì (ID 208)

As it can be observed, the variables are well dispersed around the best fitting line. On the one hand, reanalysis data of air temperature, and R_s follows the trends of the corresponding measured ones, on the other hand, a deviation from the perfect fitting line can be observed when comparing relative air humidity and U_{10}.

Considering the entire dataset, table 5.1 shows the values of RMSE and MBE associated, for each climatic station, for all the examined climate variables, as well as the minimum, maximum and average RMSE and MBE values referred to the whole database.

The RMSE associated to T_{min}, T_{max} and R_s resulted quite low and equal, on average, to 2.13 °C, 2.52°C and 2.95 MJ m^{-2} d^{-1} respectively. While the average RMSE values associated with RH_{min} and RH_{max}, resulted of 14.14% and 9.94%, respectively.

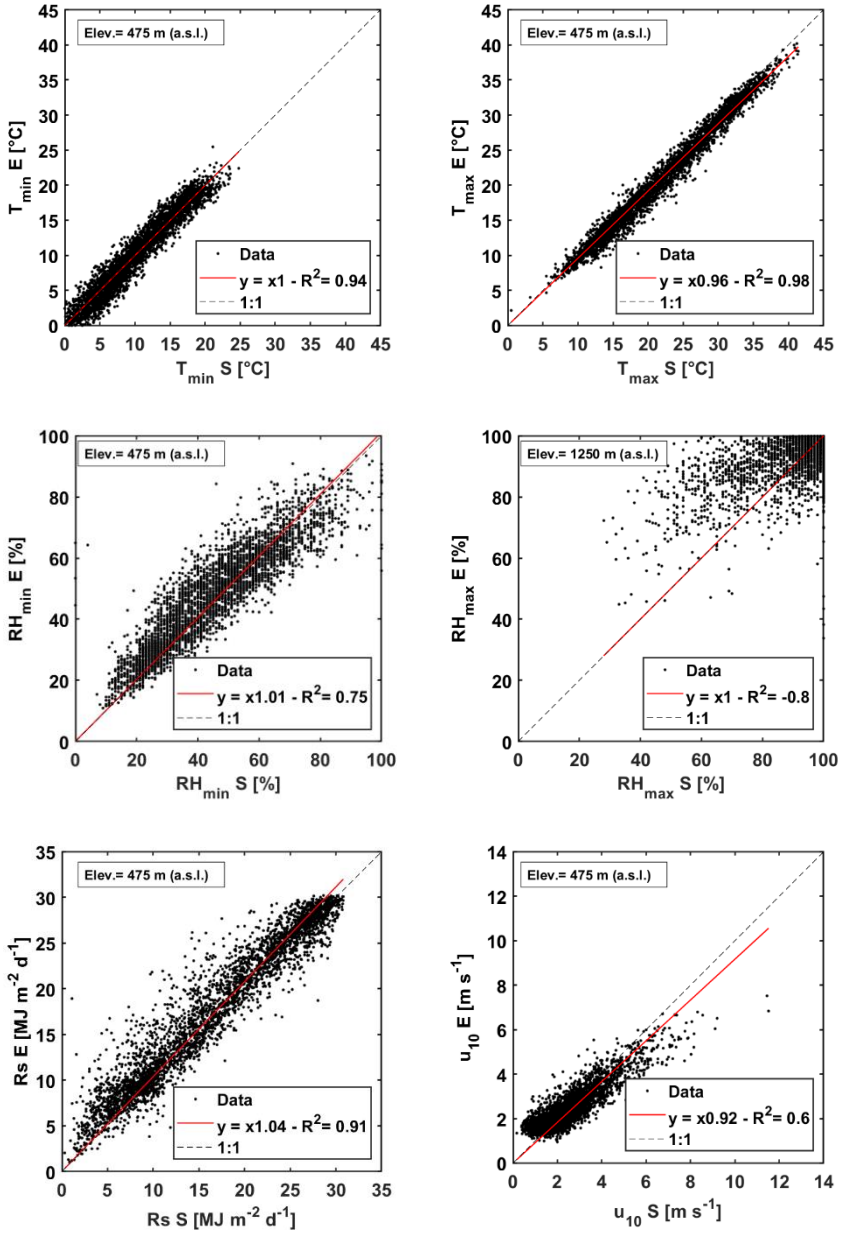

Figure 5.1: Scatterplots of daily climate variables (T_{min}, T_{max}, R_s, RH_{min}, RH_{max}, U_{10}) retrieved from ERA5 dataset (E, y-axis) and measured on ground by SIAS (S, x-axis) by the weather stations of Canicattì (ID 208).

Table 5.1: Values of RMSE and MBE associated to the climate variables calculated for all the weather stations.

	T_{min}		T_{max}		RH_{min}		RH_{max}		Rs		u_{10}	
ID	*RMSE*	*MBE*	*RMSE*	*MBE*	*RMSE*	*MBE*	*RMSE*	*MBE*	*RMSE*	*MBE*	*RMSE*	*MBE*
	[°C]		[°C]		[%]		[%]		[MJ $m^{-2}d^{-1}$]		[m s^{-1}]	
206	1.80	0.61	2.73	-2.48	10.67	7.33	6.99	-2.09	2.51	1.01	0.59	-0.16
208	1.50	-0.07	1.49	-0.95	8.08	2.10	6.83	-0.46	2.47	1.11	0.63	-0.02
209	2.77	-2.23	1.96	-1.48	11.18	7.84	10.22	3.44	2.45	0.21	1.02	-0.54
213	1.83	1.26	3.70	-3.38	22.43	20.13	9.15	0.81	2.48	-0.24	1.74	1.20
216	1.94	0.73	3.07	-2.83	11.20	8.55	8.04	-0.61	2.36	0.55	0.95	-0.36
220	1.83	-1.23	1.73	-1.24	8.77	4.63	7.75	0.84	2.57	0.98	0.69	0.16
222	2.04	1.13	2.47	-2.13	12.02	8.26	8.15	1.31	2.67	1.02		
224	2.07	-0.59	5.79	-5.60	19.85	17.82	10.83	4.28	2.86	1.09		
228	1.78	0.86	2.18	-1.31	13.21	10.09	8.35	3.53	2.56	0.24	0.75	0.04
231	2.15	-1.61	2.42	-2.02	15.77	9.55	12.93	6.26	3.27	0.60	1.47	-1.13
232	1.80	0.79	1.98	-1.63	14.14	11.17	7.63	-0.27	2.42	0.37	0.89	-0.14
235	2.21	1.40	1.39	0.50	13.79	6.78	10.91	5.32	3.33	1.65		
242	1.67	-0.47	1.66	-0.81	10.16	5.12	9.31	1.27	2.60	0.65	0.80	-0.36
245	3.76	3.36	4.05	3.57	19.48	1.51	10.52	-1.64	4.75	1.99		
246	1.41	-0.15	1.46	-0.55	13.44	7.67	14.37	8.45	3.20	1.02	0.93	-0.57
251	2.46	1.74	1.82	1.01	13.70	5.88	10.97	-7.86	2.96	0.25		
257	1.55	-0.33	3.63	-3.20	17.17	12.39	9.18	0.45	3.00	1.45	1.18	0.85
258	1.41	0.46	2.88	-2.66	19.71	17.85	10.71	4.01	3.00	1.25	1.35	0.51
259	3.91	3.50	1.53	0.54	16.43	5.92	10.80	-2.11	5.02	3.04		
262	1.62	-0.84	1.76	-1.26	10.87	6.49	8.53	3.14	2.74	1.00	1.29	-1.08
264	1.82	0.06	1.67	0.98	9.57	3.65	9.85	1.35	2.92	1.41		
265	1.59	0.87	2.55	-2.06	21.16	18.54	12.79	-1.19	3.07	0.86		
267	1.65	1.08	3.47	-3.20	14.79	11.78	7.67	-1.35	2.44	0.62		
268	1.99	-1.35	2.45	-2.20	10.19	5.64	9.60	3.93	2.77	0.90	0.91	-0.53
271	1.54	0.80	3.93	-3.71	19.05	16.70	8.30	-0.92	2.91	1.19	1.54	0.91
275	2.11	1.12	1.30	0.09	12.73	4.45	9.98	1.48	3.38	1.69	1.45	-0.80
276	1.99	-1.63	3.78	-3.48	17.59	15.10	12.66	8.56	2.96	1.46	1.46	1.13
282	3.07	2.62	2.55	-2.06	14.24	11.05	9.22	-6.22	2.54	0.23	1.93	1.43
286	1.76	0.52	1.88	1.33	11.40	0.64	10.22	-0.69	3.12	0.14	2.27	-1.91
288	1.51	0.78	2.97	-2.74	13.80	10.37	9.42	-4.25	2.67	0.38	1.67	1.16
292	1.60	-0.33	2.72	-2.29	15.00	12.18	9.10	1.81	2.73	0.02	1.34	-1.10
298	1.74	-0.27	1.45	-0.53	10.15	4.79	9.90	3.22	3.00	0.53	1.25	-1.01
301	1.90	-0.70	2.48	-0.25	13.75	-0.28	7.90	-0.44	3.41	2.35		
302	3.57	3.16	3.29	-2.77	24.15	21.69	10.36	-4.70	2.34	0.33	1.99	1.51
305	3.86	3.36	2.71	-2.45	13.22	9.97	11.54	-9.19	2.69	0.77	1.31	1.00
308	1.50	-0.64	1.37	-0.65	8.81	4.18	10.08	4.12	2.81	1.07	1.76	-1.38
309	3.49	3.09	3.70	3.30	15.67	4.04	10.30	1.19	3.92	1.91		
311	2.40	0.43	2.59	1.66	14.34	4.18	11.84	3.44	3.50	1.61		
312	2.42	-1.90	1.54	-0.98	9.70	6.26	14.58	9.81	2.65	0.44	1.18	-0.82
min	1.41	-2.23	1.30	-5.60	8.08	-0.28	6.83	-9.19	2.34	-0.24	0.59	-1.91
max	3.91	3.50	5.79	3.57	24.15	21.69	14.58	9.81	5.02	3.04	2.27	1.51
average	2.13	0.50	2.52	-1.28	14.14	8.77	9.94	0.98	2.95	0.95	1.27	-0.07

ERA5-L climate variables showed, in general, a good capability in estimating the main variables needed to assess *ETo* by means FAO56-PM equation. When considering the initial 39 weather stations the average values of RMSE (Table 5.1) refer to T_{min} and T_{max} was slight better than those found by Negm et al. (2017) in Sicily, using NASA-POWER database, were

2.13 C° and 2.5 C°, respectively; this can be attributed to the more detailed spatial resolution. In Campania region Pelosi et al. (2020), using the ERA5-L database, found an average RMSE value associated to air temperature and wind speed equal to 1.2 C° and 2.78 m s^{-1}, respectively; these values agree with those obtained in this study (1.77 C° and 1.27 m s^{-1}). Despite the different morphology characteristics, between these two Italian regions, the low RMSE values obtained using ERA5-L database and indicates that the ERA-Land database adapted well to the different climate conditions.

For the weather stations in which the measurements of U_2 and U_{10} were available, the reliability of the wind speed downscaling coefficient 0.75 suggested in the FAO56 paper (Allen et al., 1998), obtained by the assumption of the logarithmic wind profile, was evaluated. For these weather stations, annex 1 shows the scatterplots between daily average U_2 and the corresponding U_{10}.

As it can be observed, the values of *b* ranged between 0.35 and 0.74. These are the lowest values associated to the near weather stations where occur atmospheric instability due to the presence, nearby the weather station, of hedges and tall trees causing deviations of the wind speed profiles. The variability of the *b* in the scatterplot between the U_2 and U_{10} highlights that in some cases the general practice to consider a unique downscaling coefficient equal to 0.75 obtained by the application of the logarithmic wind speed profile not always is prudent. This because the weather station's local position and the environmental conditions around the station (i.e. trees and buildings) could cause uncertainties on the validity of the logarithmic wind speed profile assumptions and, consequently, the downscaling coefficient could not be enough to consider all these factors. Therefore, before the downscaling of wind speed values, it would be appropriate to locally verify the reliability of the logarithmic wind speed profile.

For each weather station, annex 2 shows the values of RMSE and MBE as a function of the ground station elevation, z (m a.s.l.).

The variability of RMSE and MBE values associated to T_{avg}, RH_{avg} and R_s is minimal up to elevation values equal to 600 m a.s.l., whereas it increases for elevation values above 600 m a.s.l. It is to notice the exception for the MBE and RMSE values associated to R_s and U_{10}, where it is not possible to observe a clear relation with the elevation of the weather station. A similar analysis was conducted by Negm et al. (2017) which found a value equal to

650 m a.s.l. Therefore, for T_{avg}, RH_{avg} and R_s variables can be possible to assert that ERA5-L database, up to 600 m a.s.l., is slightly dependent on the elevation.

5.1.1 Crop reference evapotranspiration, estimated from SIAS and ERA5-Land climate variables

The suitability of ERA5-L database to estimate *ETo* was assessed for all weather stations for which wind speed data at 10 m were available. For these weather stations, table 5.2 summarizes the values of the statistical indicators associated with *ETo*.

In general, the estimates of *ETo* from ERA5-L database are in good agreement with the corresponding values obtained according to the SIAS weather stations. The values of *b*, ranges between 0.77 and 1.00 with an average value equal to 0.90, denoting a maximum underestimation of 23% in the ERA5-L database. The dispersions of the *ETo* values around the best fitting line 1:1 is expressed in terms of R^2. The values ranging between 0.86 and 0.96 with an average value equal to 0.92, indicate a generally slight dispersion around the perfect fitting. RMSE and MBE, ERA5-L provided daily *ETo* estimates with good accuracy characterized by overall RMSE equal to 0.73 mm d^{-1} and corresponding MBE equal to -0.36 mm d^{-1}. Similar results were obtained by Pelosi et al. (2020), who considering 18 weather stations over Campania region, their RMSE values ranged between 0.44 mm d^{-1} and 1.04 mm d^{-1} with a mean value equal to 0.67 mm d^{-1}. These suggest the possibility of replicating the analysis in other different regions to assess the suitability of ERA5-L database in different climate and morphological conditions. The values of RMSE found by Negm et al. (2017) were also similar to those found in this study, with a minimum and maximum RMSE equal to 0.68 mm d^{-1} and 1.27 mm d^{-1}, respectively.

Table 5.2: Statistical indices associated to *ETo* values estimated with SIAS and ERA5-Land database.

ID	Statistical indices (ETo)			
	b	R^2	*RMSE [mm]*	*MBE [mm]*
206	0.90	0.96	0.58	-0.34
208	0.99	0.96	0.42	0.00
209	0.86	0.91	0.92	-0.63
213	0.81	0.90	1.07	-0.65
216	0.85	0.94	0.87	-0.68
220	0.96	0.95	0.48	-0.12
228	0.93	0.92	0.62	-0.31
231	0.82	0.93	0.84	-0.59
232	0.88	0.93	0.73	-0.45
242	0.92	0.93	0.59	-0.22
246	0.89	0.93	0.65	-0.33
257	1.00	0.90	0.56	-0.04
258	0.88	0.94	0.62	-0.39
262	0.86	0.95	0.74	-0.53
268	0.88	0.94	0.73	-0.45
271	0.91	0.88	0.66	-0.30
275	0.92	0.86	0.80	-0.20
276	0.97	0.92	0.52	-0.11
282	1.00	0.90	0.54	0.04
286	0.88	0.88	0.83	-0.26
288	0.95	0.90	0.57	-0.16
292	0.77	0.92	1.26	-1.03
298	0.87	0.92	0.79	-0.44
302	0.87	0.90	0.81	-0.41
305	0.98	0.93	0.51	0.03
308	0.86	0.93	0.88	-0.56
312	0.81	0.91	1.05	-0.67

Specifically, daily *ETo* reached the best performance in the Canicatti station (ID 208), figure 5.2a, with the lowest values of RMSE equal to 0.42 mm d^{-1} and MBE equal to 0.00 mm d^{-1}. While the lower performance was observed in Lentini station (ID 292), figure 5.2b, with RMSE 1.26 mm d^{-1} and MBE equal to -1.03 mm d^{-1}.

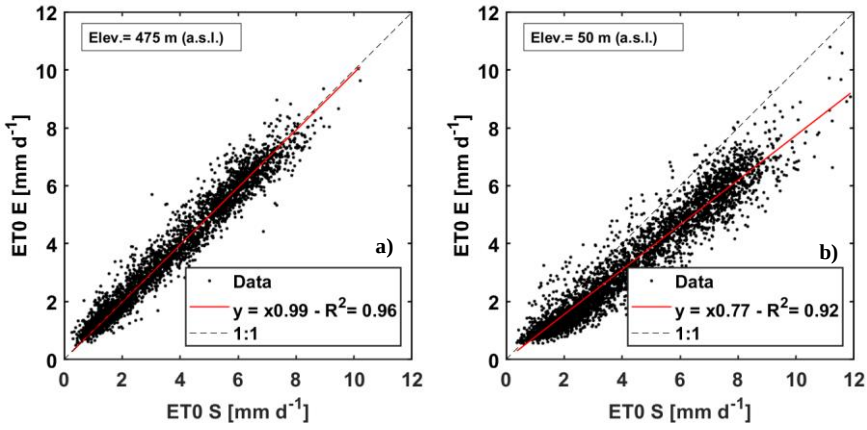

Figure 5.2: Scatterplot between *ETo* estimated using ERA5-Land climate variables and corresponding ground measurement for the best a) Canicatti (ID= 208) and the worst b) Lentini (ID= 292) weather station.

5.1.2 Sensitivity analysis of FAO56-Penman-Monteith equation

For each climate variable and weather station considered, figure 5.3 shows the average values of S_{ci} referred during the analysis period (2006-2015). The temporal variability of S_{ci} for each weather station is expressed through the standard deviation bar. For T_{min}, T_{max}, R_s and U_{10}, the values are relatively stable among the weather station considered, with an average standard deviation equal to 0.10, 0.04, 0.19 and 0.12, respectively. Only the RH_{max} and RH_{min} shows the largest fluctuations, with average standard deviation equal to 0.42 and 0.49, respectively. This indicates that relative air humidity, during period under investigation changes most rapidly than other variables. When considering the average values of S_{ci} among the weather stations, T_{min}, T_{max}, R_s, and U_{10}, show the average values of S_{ci} equal to 0.59, 0.06, 0.33 and 0.27 respectively, with corresponding values of standard deviation equal to 0.06, 0.02, 0.03 and 0.03, respectively. For these variables, the values of standard deviation close to zero suggest that the location of the weather stations does not change the sensitivity of the FAO56-PM equation.

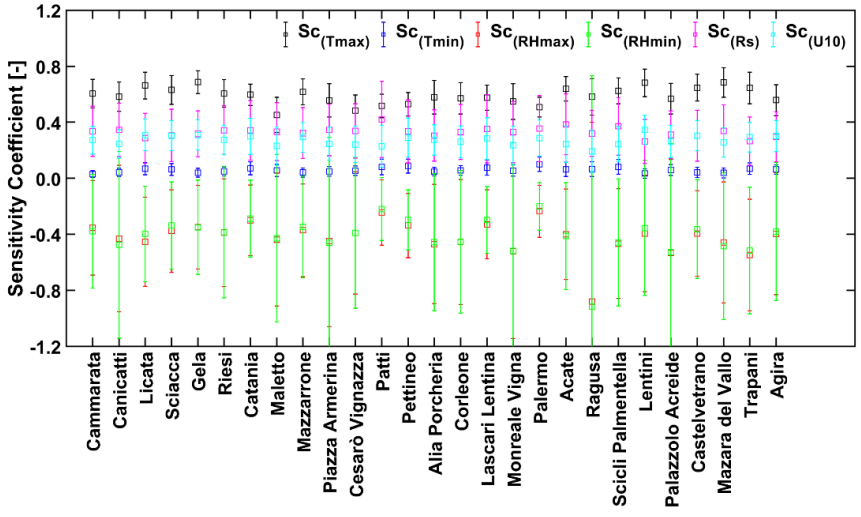

Figure 5.3: Mean values of sensitivity coefficient for each variable and weather stations referred to the analysis period (2006-2015).

A different evaluation is necessary for the S_{ci} referred to the RH_{max} and RH_{min} which show an average value of -0.42 and -0.41, with standard deviation equal to 0.12 and 0.13, respectively. In this case, relative air humidity is the variable with the largest standard deviation, highlighting that this variable is more sensitive to the location of the weather station.

Annex 3 summarizes the values of *b*, S_{ci} E_i, referred to each variable. The individual error E_i for each variable was calculated using equation 4.3. The error E_i explains the effect of an overestimation or underestimation in the estimation of *ETo* compared to the use the ERA5-L climate variables. Specifically, for Canicatti (ID 208) station, the higher errors E_i occur for T_{max} (E_i= -2.32), U_{10} (E_i= -2.00) and R_s (E_i=1.40), which have the worst performance which values b equal to 0.96, 0.92 and 1.04, respectively. On the other hand, for the variables T_{min}, RH_{max} and RH_{min}, the values of *b* equal to 1.00, 0.99 and 1.01 can compensate the error in the *ETo* estimation. While for Lentini (ID 292) station, the poor values of *b*, for T_{max}, U_{10} and RH_{min} equal to 0.92 and 0.65 and 1.25, respectively cause the worst performance in *ETo* estimation.

The sensitivity analysis allows to identify the variables with the highest error rates on *ETo* estimation. Specifically, in this study, *ETo* is most sensitive to relative air humidity and T_{max}. Estévez et al. (2009) and Liang et al. (2008)

found similar result, using a similar approach, in Spain and China, respectively. The standard deviation equal to ± 12% associated to $Sc_{(RH)}$ was similar to Gong et al. (2006) with values ranging between -20 % to 20% referred mainly in the lower region of the Chang Jiang river basin, China. For the other variables ($Sc_{(Tmax)}$, $Sc_{(Tmin)}$, $Sc_{(Rs)}$ and $Sc_{(U10)}$) were not possible to appreciate relevant spatial variations. Similar results were obtained by Liang et al. (2008), in the Tao'er River Basin, China, they found that relative air humidity has the highest spatial variability. Therefore, it is possible to assert that a high uncertainty in T_{max} and RH_{min} can cause the largest effects on *ETo* estimation.

5.2 Estimation of actual evapotranspiration by means machine learning algorithm

5.2.1 Input variables: In situ data

For the citrus orchard (fig. 3.2), the left column of figure 5.4 shows the temporal dynamics of daily R_s (a), average air temperature, T_{avg} (c), relative air humidity, RH_{avg} (e), and wind speed measured at 2 m above the soil surface, U_2 (g), acquired by the WD weather station (black line) or retrieved by ERA5-L reanalysis database (blue dots) in the examined period (from March 2019 to September 2021). For each considered variable, the right side of figure 5.4 shows the scatterplots between ground and reanalysis observations; the coloured bar indicates the DOY.

As it can be observed, R_s during the three years followed similar patterns with values ranging between a maximum of about 345 W m^{-2} in summer and a minimum of 18 W m^{-2} in winter. The annual dynamic from the two databases resulted quite similar, even if R_s values retrieved from the ERA5-L were slightly overestimated (b = 1.03; RMSE = 32.68 W m^{-2}), the higher differences associated with the lower R_s values, mostly concentrated during winter. The dynamic of average air temperature, T_{avg}, is similar to the R_s one, with a maximum of around 30°C in summer and a minimum of about 10°C in winter. The average air temperature retrieved by the ERA5-L database resulted slightly underestimated if compared with the ground measurements (b = 0.93; RMSE = 2.25°C). The annual patterns of RH_{avg} measured on the ground ranged from a minimum of about 40% to a maximum of about 98%.

A slight overestimation (b = 1.03; RMSE = 8.64%) characterized the values of RH_{avg} assessed on the basis of ERA5-L records.
Finally, the wind speed values at 2 m height, calculated from the ERA5-L reanalysis data, and referred at 10 m height by assuming a logarithmic wind profile, resulted generally higher than the ground measurements, with a coefficient of the regression line passing through the origin equal to b = 2.00 and RMSE value equal to 1.43 m s^{-1}.
For all the climate variables, the results of the comparison between the climate data acquired from the weather station (ID=302), installed near the olive orchard (fig.3.5), and ERA5-L reanalysis climate are shown in table 5.1.

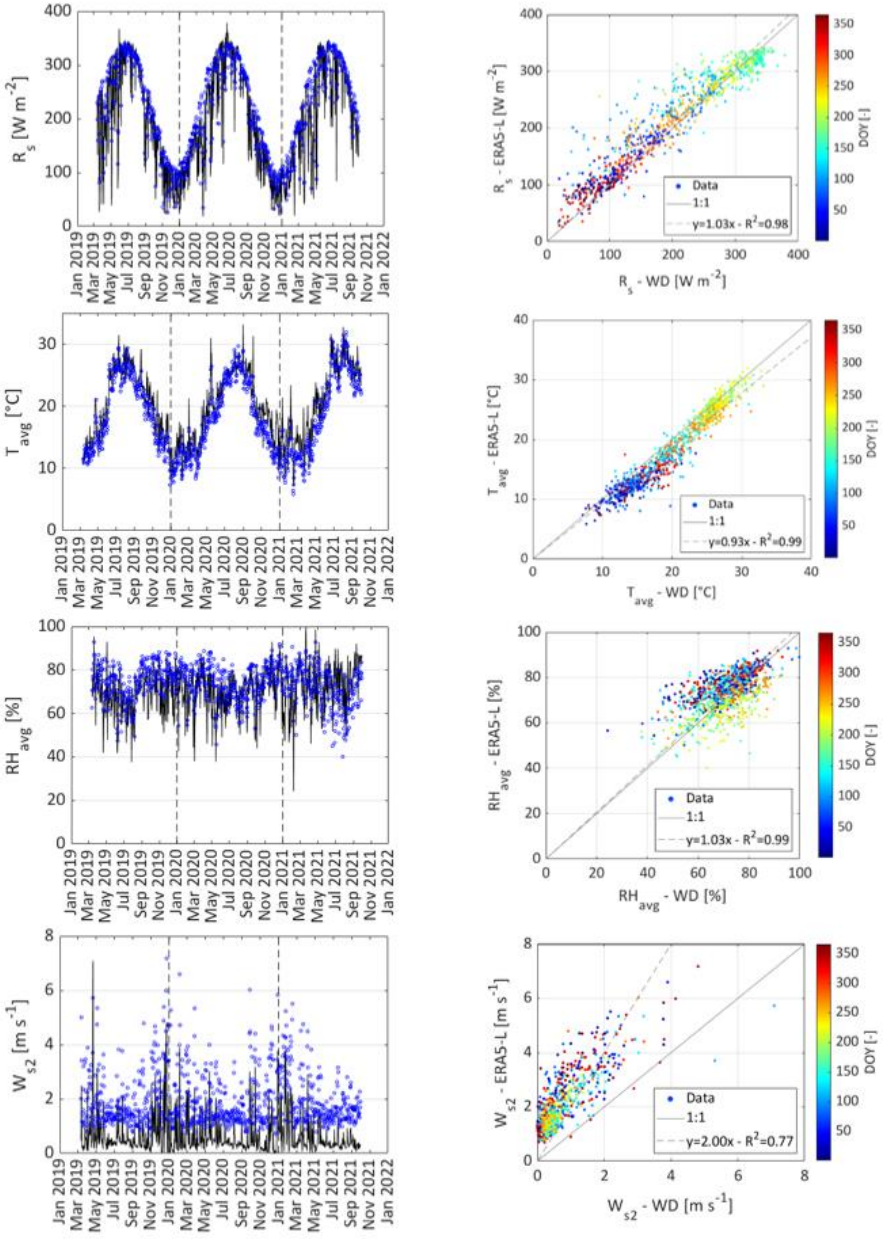

Figure 5.4: Temporal dynamics of a) daily global solar radiation, R_s, c) average air temperature, T_{avg}, e) average air relative humidity, RH_{avg}, and g) wind speed, U_2, registered by weather station (black line) and ERA5-Land data (blue dots); b), d), f) and h) shows the scatterplot from the two sources. The color bar indicates the day of the year (DOY).

The availability of the main agrometeorological variables such as R_s, air temperature and relative air humidity acquired by weather stations, is essential to obtain a high-quality estimation of the evaporative atmospheric demand. However, in the examined area, reanalysis database such as the NASA-POWER or the ERA5-L can be considered a suitable surrogate of the ground data, as evaluated by several authors for most weather stations installed in Sicily (Negm et al., 2017; Pelosi and Chirico, 2021; Vanella et al., 2022).

For the three years of observations, figure 5.5 shows the daily dynamics of average SWC (black line) and precipitation (blue bars) in the citrus orchard. The values of SWC were obtained as the mean of the measurements registered by the four probes in the layer 0-0.50 m in which the active roots are mainly located. The dynamic of the SWC profile from topsoil to 0.50 m depth is also shown at the bottom of the figure.

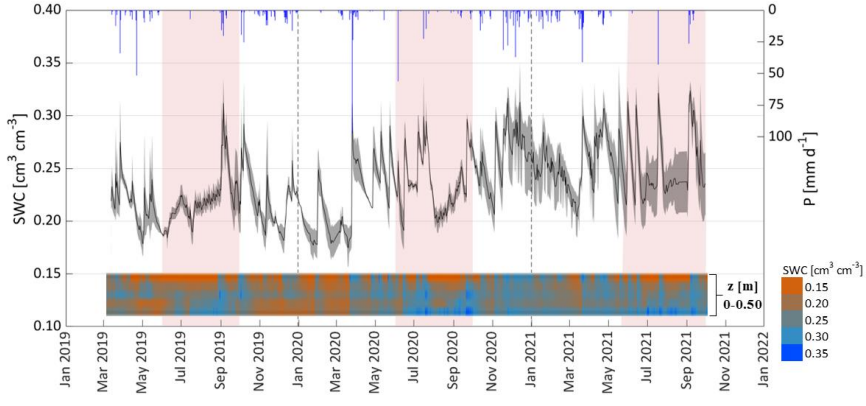

Figure 5.5: Temporal dynamics of daily average soil water content (black line), SWC, and precipitation, P in the citrus orchard. SWC profile from 0 to 0.5 m depth is also shown at the bottom of the figure.

The rapid increases of SWC always occurred during rain events or after a few micro-sprinkler irrigation events (February, May and June 2020, as well as in May and June 2021) supplied after long periods of droughts or immediately before weeding. The patterns of SWC profiles at the bottom of figure 5.5 also shown that during the periods in which the SDI system operated, the layer 0.30 m-0.50 m was the only wetted portion of the soil, being the upper part of the soil profile characterized by relatively lower

SWC. The standard deviation associated with SWC ranges from a minimum (close to zero) to a maximum of 0.06 cm^3 cm^{-3}. Since the end of 2020, the standard deviation values resulted relatively higher than in the previous period due to the failure of one of the four probes installed in the field.

The accuracy of balance closure was verified based on the CR, (eq. 2.33) (Prueger et al., 2005) computed only from the subset of hourly data with $R_n \geq 100$ W m^{-2}, whose values resulted satisfactory and equal to 0.98, 0.88 and 1.03 for 2019, 2020 and 2021, respectively. On the other hand, for the olive orchard (fig. 3.9), the values of CR resulted equal to 0.90 in 2009 and 0.92 in 2010 (Cammalleri et al., 2013b) and 1.02 in 2011 (Autovino et al., 2016). For tree crops, Kustas et al. (1999) considered acceptable values of CR ranging between 0.80 and 0.90. Values of the CR, equal to 1.08 and 1.03, were obtained by Er-Raki et al. (2009) in two citrus orchards in south Morocco characterized by a semi-arid Mediterranean climate. Figure 5.6a,b shows the temporal dynamics of daily actual evapotranspiration (red dots) and daily precipitation (blue bars), in the Villabate citrus orchard and Castelvetrano olive orchard, respectively.

For the three years of observation (2019–2021), figure 5.6 shows the temporal dynamics of precipitation, P, and daily ET_a, measured by the EC flux tower. The temporal dynamic of daily ET_a resulted similar in 2019 and 2020, but for the 2021 year, the values of ET_a resulted generally higher, with a maximum value slightly lower than 6 mm d^{-1}. EC system monitoring was interrupted from March to June 2020, due to the instrument failure occurring during the COVID-19 pandemic lockdown. This effect can be associated with the relatively higher air temperatures registered in 2021 compared with the other two years, as well as with the transpiration of the growing weeds due to field mismanagement during the irrigation season.

In the olive orchard, for the examined period (2009-2011) (fig. 5.6b), 92 ET_a values, corresponding to rainy days, were excluded from the analysis. A total of 573 ET_a measurements resulted available out of 1095 days of observations (52.3 %). The maximum ET_a values, slightly higher than 4 mm d^{-1}, generally occurred between May and June. The missing values of daily ET_a are scattered during the three years. As it can be observed, the periods with the most missing data are concentrated from November 2009 to March 2010 and from August to November 2011.

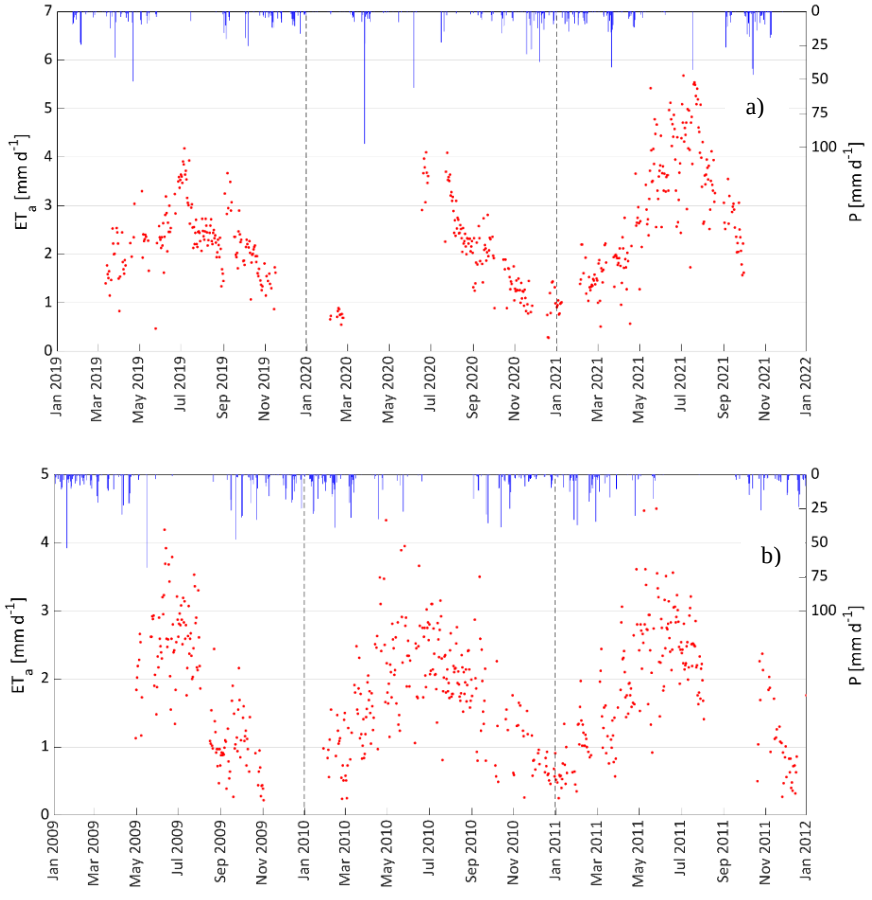

Figure 5.6: Temporal dynamics of actual crop evapotranspiration (red dots), ET_a, and precipitation (blue bars), P, for the citrus orchard a) and olive orchard b).

5.2.2 Input variables: remotely sensed data

Based on equations (2.18) and (2.19), maps of NDVI and NDWI with a spatial resolution of 10 m, were generated for the citrus orchard. To downscale the maps of NDWI at 10 m resolution, the value of a single pixel in the shortwave region (20 m resolution) was associated with the corresponding four values in the NIR region. A continuous time series of daily VIs were obtained based on linear interpolations carried out between

consecutive pairs of Sentinel-2 images acquired at two different dates (Pan et al., 2017).

The temporal dynamic of the examined VIs for the citrus orchard, is shown in figure 5.7. For both the VIs, the annual trends resulted quite similar, with values in winter generally higher than in summer.

In summer, the NDVI and NDWI assumed values were around 0.55 and 0.10, respectively, which resulted lower than in winter when the values fluctuated around 0.90 and 0.45. On the other hand, the trend tended to decrease in spring (March-May) and to increase in fall. The intra-field variability for both VIs resulted quite limited, with values of standard deviation ranging between 0 and a maximum of 0.13 for NDVI and from 0 and 0.11 for NDWI.

Figure 5.8a,b shows the comparison between NDVI and NDWI retrieved from Sentinel-2 (black line) and MODIS (red line) for the olive orchard. The Sentinel-2 VIs, with the corresponding standard deviations, were obtained through zonal statistics considering all the Sentinel-2 pixels contained within the pixel MODIS. The generally good agreements between the NDVI (b = 0.95; R^2=0.99) and NDWI (b = 0.88; R^2 = 0.96) obtained from the two different platforms strongly depend on the homogeneity of soil and land characterizing the MODIS pixel (Autovino et al., 2016).

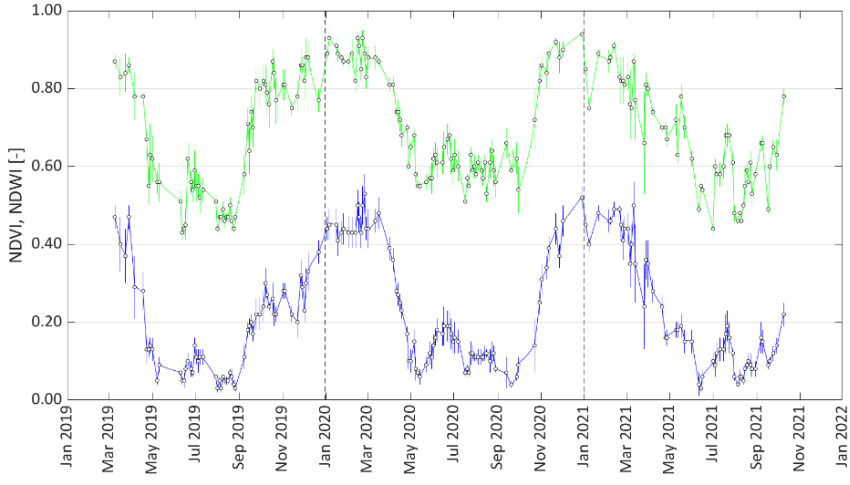

Figure 5.7: Temporal dynamics of average NDVI (green line) and NDWI (blue line), retrieved from Sentinel-2 satellites for the citrus orchard.

The best *m(x)*, and *k(x,x')*, functions were assessed with the complete dataset related to the citrus orchard, which includes all the examined variable considered in the combination 1 shown in table 4.4. Annex 4 summarizes the statistical indicators associated with the fifteen combinations of the examined *m(x)* and *k(x,x')* functions.

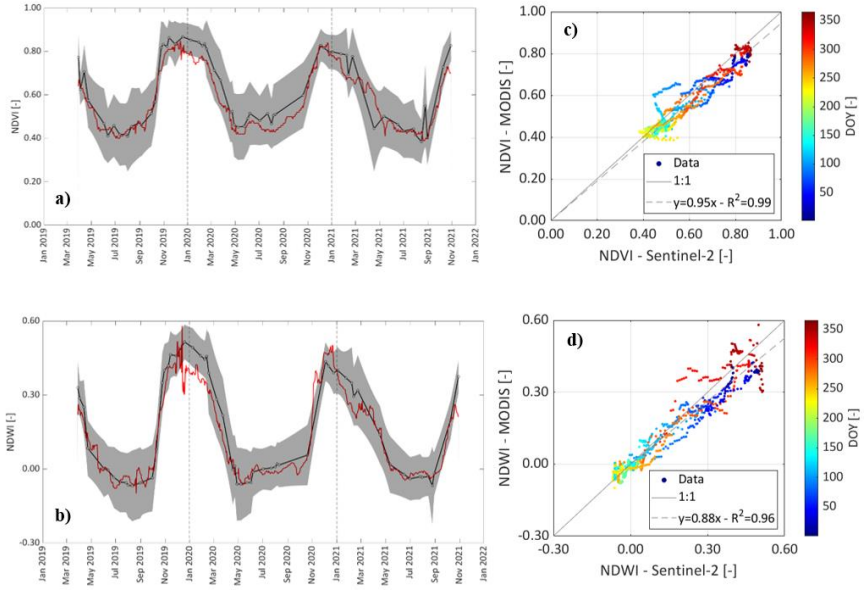

Figure 5.8: Comparison between the temporal dynamics of NDVI (a) and NDWI (b) retrieved from Sentinel-2 satellites (black line) and MODIS (red line) products for the olive orchard. The corresponding scatterplots of NDVI and NDWI obtained by Sentinel-2 versus the corresponding MODIS are also shown on the right (c, d).

5.2.3 Predicted actual evapotranspiration values in the Villabate experimental field

Figure 5.9a,b illustrates the temporal dynamics of simulated and estimated ET_a when considering the complete database of the input variables and implementing the best and the worst *m(x)* and *k(x,x')* functions in the GPR model. On the right side, the scatterplots of the corresponding estimated versus measured ET_a are also shown (fig. 5.9c-d). Despite the limited differences in the examined statistical indicators, the best result was obtained when assuming a zero mean function and an exponential kernel covariance function. Under these assumptions, the estimations of ET_a

resulted characterized by RMSE = 0.38 mm d^{-1} and MAE = 0.28 mm d^{-1}. On the other hand, the worst result, characterized by RMSE = 0.45 mm d^{-1} and MAE = 0.32 mm d^{-1} was obtained when assuming a constant *m(x)* and a squared exponential *k(x,x')*. In general, however, regardless of the *m(x)* and *k(x,x')* functions, the model estimates quite well the daily actual evapotranspiration (NSE > 0.83), even if the values resulted always slightly underestimated (*b* < 1.0).

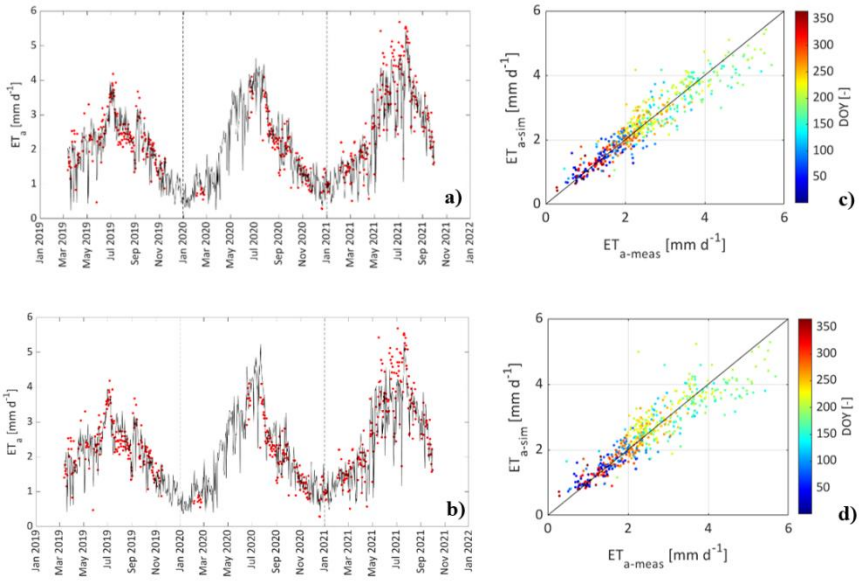

Figure 5.9: Temporal dynamic of simulated (black line), $ET_{a\text{-}sim}$, and measured (red dots), $ET_{a\text{-}meas}$, daily actual evapotranspiration obtained for the citrus orchard when considering the complete dataset and assuming the best (a) and the worst (b) combination of the mean and kernel covariance functions. The corresponding scatterplots of estimated versus measured ET_a are also shown (c, d).

The results related to the other four different combinations of the input variables (combinations 2-5) are reported in annex 5. The left side of the annex 5 shows the temporal dynamics of actual evapotranspiration estimated by implementing in the GPR model the best *m(x)* and *k(x,x')* functions; the right side of the figure shows the corresponding scatterplots of estimated versus measured daily ET_a. For the citrus orchard, table 5.3 summarizes the statistical indicators associated with the GPR model implemented with the best *m(x)* and *k(x,x')* functions and the five input

variables' combinations. As it can be observed, whatever the examined variable combination, there is always an underestimation of actual evapotranspiration with slopes of the regression lines declining from 0.97 to 0.95 as the number of variables decreases.

Table 5.3: Statistical indicators associated with the GPR model implemented with the best *m(x)* and *k(x,x')* functions and the five combinations of the input variables, for the citrus orchard.

	RMSE [mm d^{-1}]	MAE [mm d^{-1}]	R^2 [-]	*b* [-]	NSE [-]
1	0.38	0.28	0.88	0.98	0.88
2	0.43	0.31	0.84	0.97	0.84
3	0.48	0.36	0.80	0.96	0.80
4	0.53	0.39	0.76	0.96	0.76
5	0.55	0.42	0.74	0.95	0.74

The comparison of the second and third combination of the input variable, involving the measured SWC (combination 2), resulted in a better model performance than including the two VIs (combination 3), the lower RMSE and MAE and the higher R^2, *b* and NSE. The possibility to include measurements of SWC among the input variables to improve the estimations of actual evapotranspiration was also indicated by Granata (2019) in an analysis aimed to predict ET_a within a farm located in Florida, USA, by using the SVM algorithm and the Regression Tree (TR). The variables adopted by the author to implement the algorithms were: R_n, *H*, SWC, wind speed, mean relative humidity and mean temperature. He demonstrated the reduction of the model predicting capacity when excluding the SWC measurements.

By including the VIs NDVI and NDWI, it is possible to consider the plant vigour and the surface water status, respectively. Carter and Liang (2019), after evaluating ten ML algorithms to assess daily latent heat flux *LE*, which represents a proxy of ET_a, demonstrated that the quality of the results can be improved if among the input variables are included the Downward Shortwave Radiation (DSR) and Photosynthetically Active Radiation (PAR), retrieved by the Global Land Surface Satellite (GLASS), in addition of VIs (NDVI and EVI). On the other hand, Mosre and Suárez (2021) found that the use of NDWI, combined with weather data acquired by a standard

weather station, contributes to improving the quality of monthly ET_a site-specific equations. Moreover, the results of the four additional combinations of input variables demonstrated that the introduction of the VIs, as well as the SWC, improved the model performances. The highest value of RMSE (0.55 mm d^{-1}) was associated with combination 5, in which all the input variables are detected from information freely available online. However, if compared to the others, combination 5 produced the worst results; this can still be considered acceptable for practical applications related to irrigation management, considering that all the required input data can be downloaded from the web, avoiding costly and time-consuming field measurements.

The reanalysis NASA-POWER database joint with the SVM algorithm was used by Faraminan et al. (2021) to assess ET_a retrieved from the application of a SWB model. In their study, these authors found that in the semi-arid Pampean region of Argentina, the reanalysis data represents a suitable source of data to assess ET_a. These authors obtained mean RMSE and MAE equal to 0.54 mm d^{-1} and 0.39 mm d^{-1}, respectively, fairly similar to those obtained in this study, but comparatively lower values of R^2 and NSE, equal to 0.67 and 0.66, respectively. The use of ERA5-L reanalysis data, characterized by a higher level of detail compared with the NASA-POWER can therefore contribute to improve the overall quality of the ET_a estimations. To fill gaps in the time-series of daily ET_a measured in two-crop rotation in sequential seasons, Kang et al. (2019) used a Support Vector Regression (SVR) algorithm initially by including, as input variables, only the weather data (daily DSR, air temperature, vapour pressure deficit and precipitation) acquired daily in situ; then, the analysis also included: daily DSR, retrieved from the Japan Aerospace Exploration Agency (JAXA), air temperature, vapour pressure deficit and precipitation, retrieved by the National Centers for Environmental Prediction (NCPE), remote sensed data of the land surface LAI, Land Surface Temperature (LST) and two VIs (Enhanced Vegetation Index (EVI) and the Land Surface Water Index (LSWI))retrieved from the MODIS (spatial resolution of 1.5 km). When considering the ground measurements of weather variables, these authors found values of RMSE and R^2 equal to 0.46 mm d^{-1} and 0.83, respectively. On the other hand, the joint use of reanalysis and remote sensed data resulted in a lower performance of the model, which was characterized by RMSE and R^2, equal to 0.76 mm d^{-1} and 0.33, respectively. Similarly, in the present

study, the climate variables from ERA5-L reanalysis data and VIs from Sentinel-2 images (combination 5) resulted in slightly lower performance (RMSE=0.55 mm d^{-1} and R^2=0.74) than the only weather data measured on the ground (combination 4) to which corresponded RMSE and R^2 values of 0.53 mm d^{-1} and 0.76, respectively.

5.2.4 Predicted actual evapotranspiration values in the Castelvetrano experimental field

The daily actual evapotranspiration data collected in the "Tenuta Rocchette" experimental field (fig. 3.9), even if the available database did not include measurements of SWC, it allowed a further validation of the proposed ML algorithm by considering only the three variable combinations including the weather data and VIs. Figure 5.10 shows the temporal dynamics of daily ET_a estimated by assuming a zero mean function and an exponential kernel covariance function and the three combinations of the input variables, as well as the scatterplots between estimated and measured ET_a. The statistical indicators associated with the three different variable combinations are summarized in table 5.4.

Table 5.4: Statistical indicators associated with the GPR model implemented with the best *m(x)* and *k(x,x')* functions and the three combinations of the input variables, for the olive orchard.

	RMSE [mm d^{-1}]	MAE [mm d^{-1}]	R^2 [-]	*b* [-]	NSE [-]
3	0.50	0.38	0.67	0.94	0.67
4	0.51	0.39	0.65	0.93	0.65
5	0.50	0.38	0.66	0.94	0.66

As it can be observed, combinations 3 and 5 are characterized by quite similar results, with RMSE of 0.50 mm d^{-1} and a *b* value equal to 0.94, which corresponds to an average underestimation of 6%. This result is a consequence of the good performance of the ERA5-L in depicting the agrometeorological data measured on the ground nearby the olive orchard (Vanella et al., 2022). Slightly worse results were associated with combination 4 in which only measured weather data were used as input of the model.

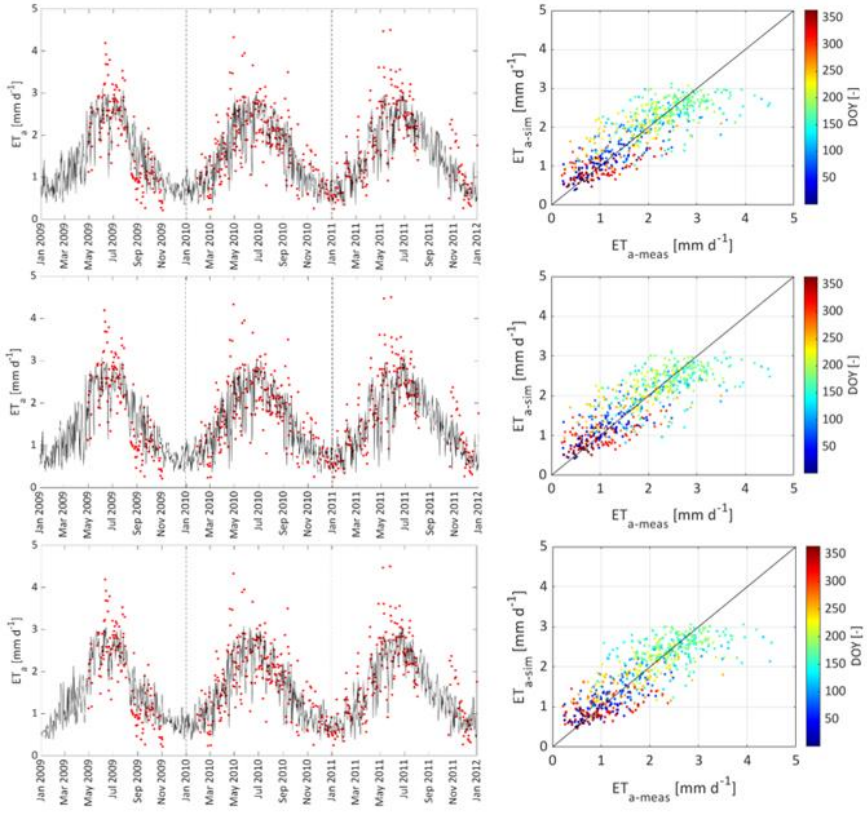

Figure 5.10: Temporal dynamics of simulated (black line), $ET_{a\text{-}sim}$, and measured (red dots), $ET_{a\text{-}meas}$, referred to the three different combinations of the input variables. The corresponding scatterplots of estimated versus measured ET_a are also shown.

5.3 ET estimation on the Villabate experimental field

5.3.1 In situ measurements: Climatic characterization

For the three years of observation (2018-2020), the climatic characterization was carried out using a standard weather station WD 2000, installed nearby the experimental field. As already mentioned, this weather station provides, hourly climate data such a: air temperature, T_a (°C), relative air humidity, RH (%), R_s (MJ m^{-2} h^{-1}), wind speed and direction at 2 m above the soil, U_2 (m s^{-1}) as well as rainfall heights, P (mm). Figure 5.11 shows the values aggregated at daily time scale of the T_{max}, T_{min} RH_{max}, RH_{min}, R_s, U_2, as well

as the values of daily *ETo*, evaluated using the FAO56-PM equation (eq. 2.30) and the daily and cumulative rainfall heights.

In the three-year observation period (2018-2020), the annual trend of R_s remained almost similar, assuming values that are quite usual for the study area, with maximums of around 30 MJ $m^{-2}d^{-1}$ in July and minimum values of around 2 MJ $m^{-2}d^{-1}$ during the winter period (December-January). The temperature trend also followed a similar dynamic to the R_s, with annual T_{max}, between 15 and 35 °C and minimums between 2 and 20 °C. Precipitation for the three years of observation was 923 mm (2018), 550 mm (2019) and 576 mm (2020), respectively and concentrated in the periods between January and May and between September and December. *ETo*, values were around 1 mm d^{-1} in January, increased in the first half of each year, reaching peak values of around 6 mm d^{-1} in the summer period, and decreasing in the following period, reaching minimum values about 1 mm d^{-1} in December.

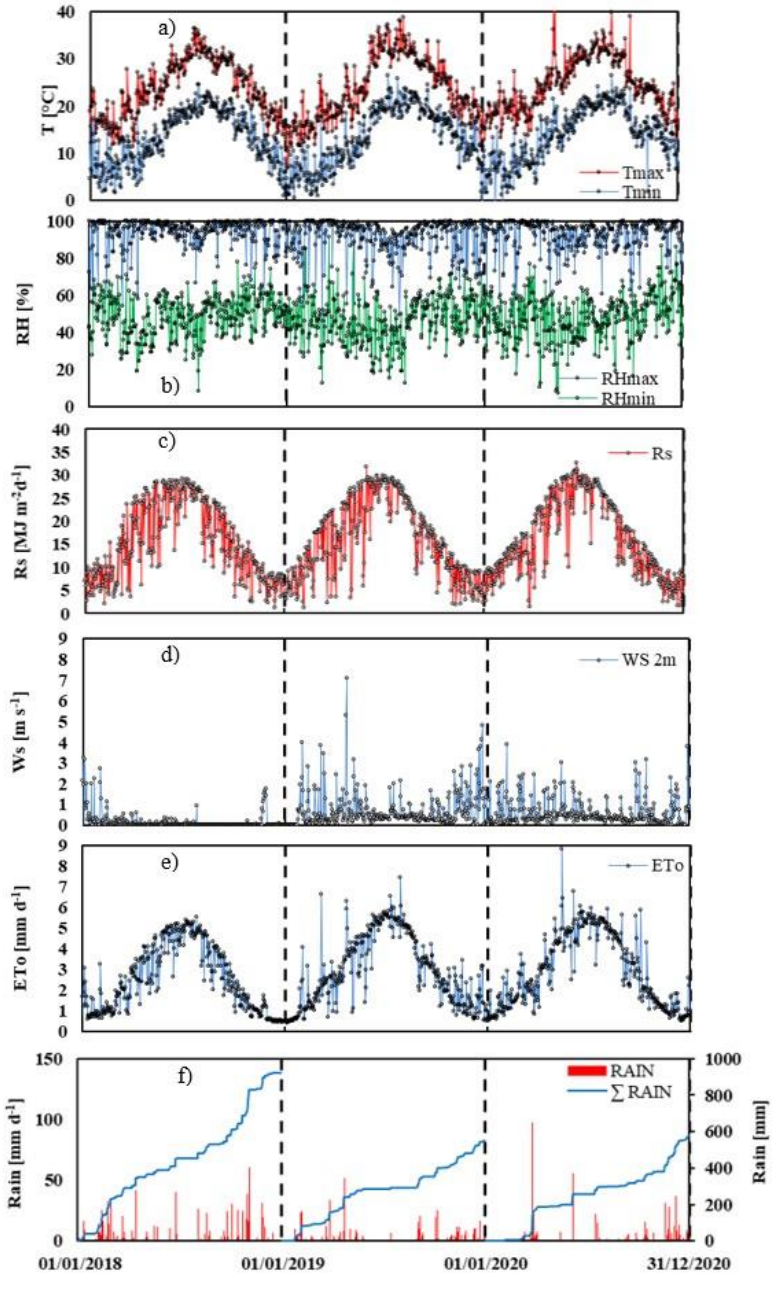

Figure 5.11: Daily temporal dynamics of maximum and minimum air temperatures a), relative air humidity b) solar radiation c), wind speed d), crop reference evapotranspiration e) and precipitation f) for the three years of observation (2018-2020).

For the three years of observation (2018–2020), figure 5.12 shows the temporal dynamics of precipitation, *P*, the amount of irrigation, *I*, daily *ETo*, estimated using the eq. 2.30, as well as, ET_a, measured by EC flux tower (presented in the section 5.2.1). The gray boxes identify the irrigation seasons (light gray), which include the periods of water deficit application (dark gray), usually applied from the beginning of July to mid-August.

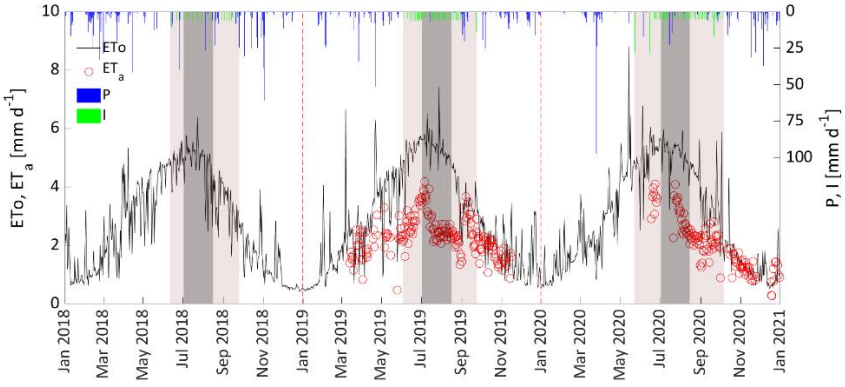

Figure 5.12: Temporal dynamic of crop reference evapotranspiration, *ETo*, precipitation, *P*, and amount of irrigation, *I*, from 2018 to 2020. Available values of actual crop evapotranspiration, ET_a, are also shown. The light box indicates the irrigation season, while the dark box identifies the period of application of water stress.

As it can be observed, even if the annual trends of daily *ETo* during the three years resulted quite similar, the values in 2018 were relatively lower than in the other two years. The maximum *ETo* generally occurred in July, during periods of limited or absent precipitation, while the minimum was registered between December and January. On the other hand, a certain variability during the three years can be noticed in the patterns of rainfall; the number of rainy days, with rainfall value equal to or higher than 2.5 mm d^{-1}, resulted 65 in 2018 and only 44 in 2020, when a prolonged drought period occurred at the beginning of the year, followed by an extreme event of 97.3 mm registered on March 25.

When considering the yearly cumulated precipitation, a total of 923 mm was recorded in 2018, and only 550 mm and 576 mm in 2019 and 2020, respectively. Likewise, the yearly crop reference evapotranspiration resulted in 988 mm in 2018, 1069 mm in 2019 and 1076 mm in 2020 (fig. 5.13).

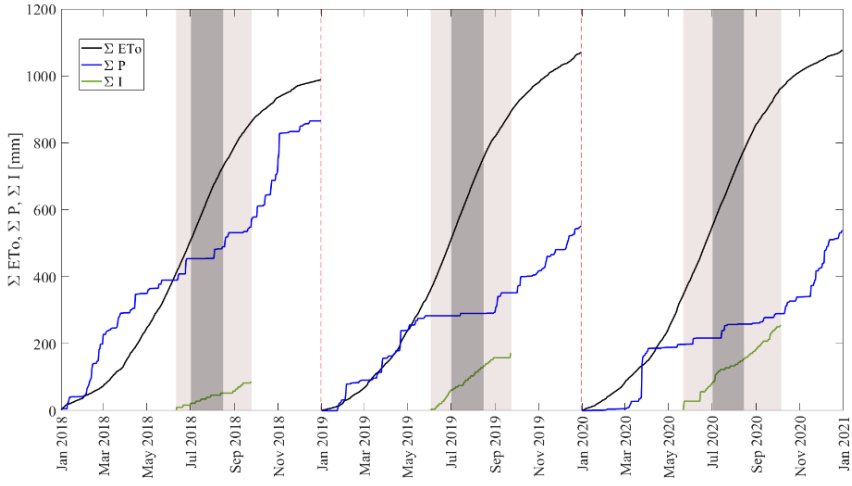

Figure 5.13: Cumulative precipitation, *ΣP*, crop reference evapotranspiration, *ΣETo*, and irrigation, *ΣI*, distributions during 2018–2020. The light box indicates the irrigation season, while the dark box identifies the period of application of water stress.

For the three investigated years, table 5.5 indicates the periods before, during and after irrigation season, and summarizes the cumulated precipitation, *ΣP*, the amount of irrigation, *ΣI*, the crop reference evapotranspiration, *ΣETo*, and the corresponding pluviometric deficits *Σ(P-ETo)*. During the irrigation seasons, the lowest pluviometric deficit, equal to − 293 mm, and it was observed in 2018; on the other hand, irrigation seasons 2019 and 2020 were characterized by higher pluviometric deficit, with values equal to − 462 mm and − 523 mm, respectively, which suggested to anticipate the start of irrigation season and to increase the applied volumes. The footprint of the flux tower, which identifies the area on the ground encompassing at least 70% of the flux source, is shown in figure 5.14; the footprint was obtained based on the model proposed by Kljun et al. (2015) and considering the dominant wind speed of 1.7 m s^{-1} with a direction of 45° (NE).

Table 5.5: Cumulated annual precipitation, ΣP amount of irrigation, ΣI , crop reference evapotranspiration, ΣETo , and pluviometric deficit $\Sigma(P - ETo)$, in the three years before, during and after irrigation seasons.

YEAR	*Date*	*Duration* [d]	ΣP [mm]	ΣI [mm]	ΣET_0 [mm]	$\Sigma (P\text{-}ET_0)$ [mm]
2018	01 Jan - 11 Jun	162	390	-	411	-21
	12 Jun - 24 Sep	105	158	87	451	-293
	25 Sep - 31 Dec	98	317	-	127	190
2019	01 Jan - 03 Jun	154	283	-	362	-79
	04 Jun - 23 Sep	112	68	172	530	-462
	24 Sep - 31 Dec	99	199	-	177	22
2020	01 Jan - 22 May	143	198	-	347	-149
	23 May - 05 Oct	136	92	256	615	-523
	06 Oct - 31 Dec	87	248	-	115	133

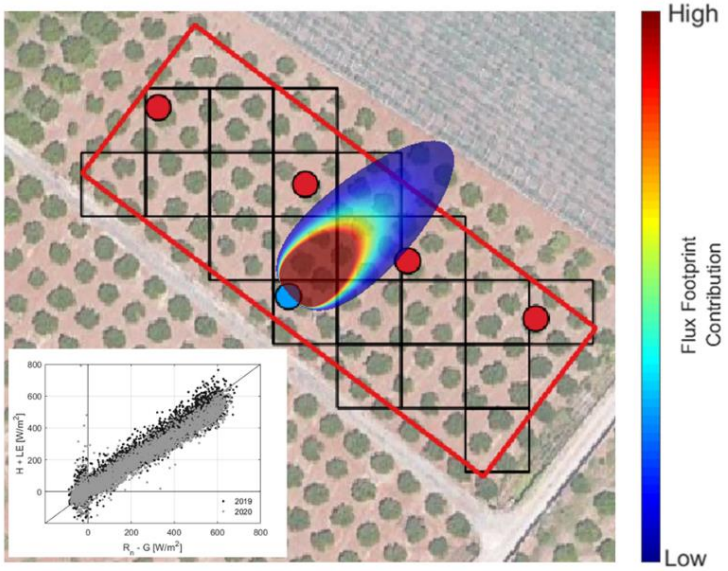

Figure 5.14: Map of the experimental plot showing the EC tower footprint. The inner box shows the scatterplot between hourly ($H+LE$) and ($R_n - G_0$) fluxes measured in 2019 (black dots) and 2020 (grey dots).

The accuracy of balance closure was verified based on the CR, (Prueger et al., 2005) computed only from the subset of hourly data with $R_n \geq 100$ W m^{-2}, whose values resulted equal to 0.98 in 2019 and 0.88 in 2020.
Daily ET_a measured with the EC tower only in 2019 and 2020 (fig. 5.12), resulted lower than daily *ETo*, except during or immediately after rainy days, because of the higher contribution of evaporation (French et al., 2020).

The availability of measurements acquired by the EC flux tower and the weather station in 2019 and 2020, provided the source of data to estimate the crop coefficient, K_c, as the ratio between ground-based ET_a retrieved in the absence of water stress and ETo (Calera et al., 2017).
The crop coefficient, K_c, temporal dynamic, calculated after excluding the rainy days (P < 2.5 mm) from the dataset of measured ET_a, is shown in figure. 5.15.

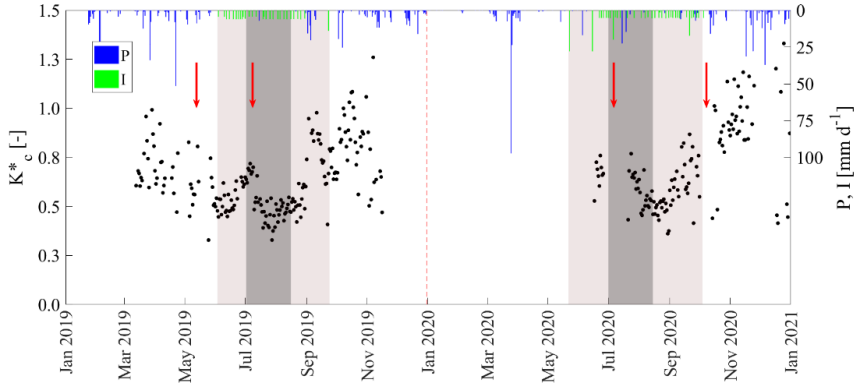

Figure 5.15: Values of the ratio between measured ET_a and ETo, K_c, in 2019 and 2020. The light box indicates the irrigation season, while the dark one identifies the period of water deficit application. Red arrows indicate the days in which weeds were cut down.

This ratio represents the actual crop coefficient, K^*_c, represented by the product, $K^*_c = K_c \cdot K_s$, between the standard unstressed crop coefficient, K_c, and the water stress coefficient, K_s. The latter is lower than 1 only in periods of crop water stress (generally occurring from the beginning of July to mid-August), and equal to 1 when SWC did not limit crop transpiration (absence of crop water stress). The values of K^*_c were characterized by a quite high variability, with trends decreasing in spring and rising at the end of summer, up to values higher than 0.55. Moreover, the rapid decline of K^*_c observed during the period of water deficit application (fig. 5.15) was due to the contextual effect of the weeds removal from the soil surface (red arrows) and the limited water supply.

5.3.2 Remote sensing data: Temporal dynamics of vegetation indices

For the three investigated years, figure 5.16 shows the temporal dynamics of VIs, NDVI and NDWI retrieved from the Sentinel-2 clear-sky images database (presented in section 5.2.2); the average and standard deviation of both VIs were determined by considering the four pixels containing the trees in which the SWC sensors were installed.

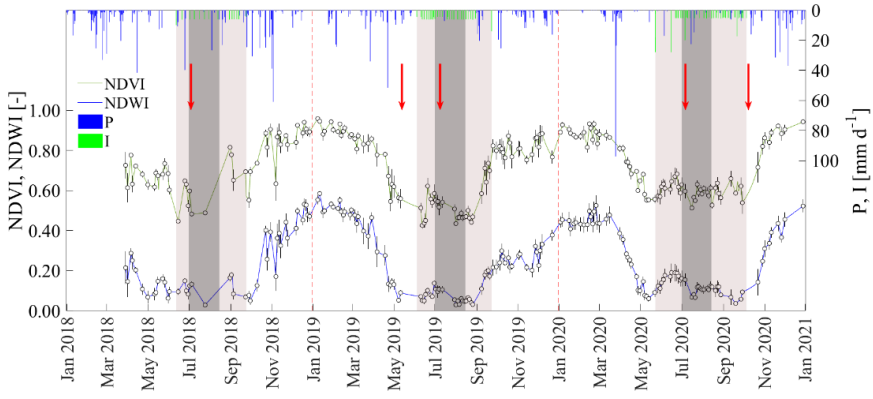

Figure 5.16: Temporal dynamic of average NDVI and NDWI, precipitation, P, and the amount of irrigation, I, for the investigated period (2018-2020). The light box indicates the irrigation season, while the dark box identifies the period of application of water stress. Red arrows indicate the days in which weeds were cut down.

The generally low standard deviations characterizing both the VIs indicated that the four pixels were almost homogeneous. The occurrence of rainfall events during the irrigation seasons 2018 and 2020 (table 5.5) determined the rise of NDVI values, due to the rapid germination and emergence of spontaneous weeds on the soil surface. On the other hand, during 2019, the lower amount of rainfall associated with the SDI system did not drive the emergence of spontaneous weeds and it caused, after weeding, the progressive decline of NDVI from 0.62 to 0.43. During the periods from late fall to early spring, NDVI resulted in slightly variable and reached values up to 0.90, due to vigorous vegetation cover in the tree rows caused by the presence of uncut weeds.

The values of NDWI, normally used to monitor the moisture conditions of vegetation canopies, ranged between 0.01 and 0.60, with the highest values associated with the high vegetation water content and coverage of a large part of the field, and the lowest associated with the low vegetation water

content and sparse coverage. The possibility to use jointly NDVI and NDWI effective to improve the evaluation of the crop coefficient in sparse orchards characterized by the sporadic presence of cover weeds.

5.3.3 Predictive relationship K_c (VIs)

To identify the relationship to predict the crop coefficient from the examined VIs, it was assumed that the joint use of the examined indices (NDVI and NDWI) can better represent the actual field conditions which was characterized by sparse vegetation, the presence of transpiring weeds on the soil surface, and a limited period of water deficit application.
Figure 5.17 shows the scatterplot representing the crop coefficient K_c, evaluated in the absence of crop water stress, as a function of the sum of NDVI and NDWI and the predictive relationship, expressed by the following exponential function characterized by $R^2 = 0.70$:

$$K_c = ae^{(b(\mathrm{NDVI+NDWI}))} \tag{5.1}$$

where a and b are two calibration coefficients equal to 0.304 and 0.939, respectively. To exclude the effects of the crop water stress in the predictive relationship, the periods of water deficit application ($K_s < 1$) were not included for this analysis.
For the investigated field**,** figure 5.18 shows some examples of maps of NDVI and NDWI, retrieved by Sentinel-2, and the corresponding K_c, estimated with eq. 5.1 in two different days (June 20, 2019, and December 4, 2019) and characterized by the absence (upper row) and the presence (lower row) of actively transpiring cover weeds on the soil surface. The sum of the two VIs in the absence of cover weeds ($NDVI_{avg} = 0.59$, $NDWI_{avg} = 0.10$) resulted lower than the one obtained under the presence of active cover weeds ($NDVI_{avg} = 0.90$, $NDWI_{avg} = 0.36$). The observed difference is due to the diverse spectral responses caused by the presence of weeds covering the soil among the tree rows and consequently, the average K_c estimated in the absence of cover weeds ($K_c = 0.58$) resulted lower than the corresponding obtained in the presence of actively transpiring weeds ($K_c \sim 1.00$).

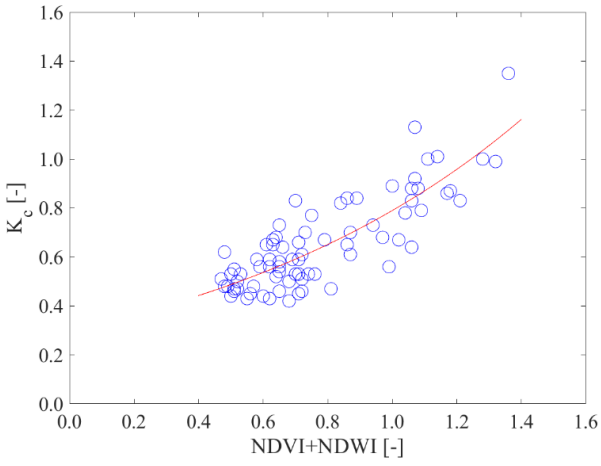

Figure 5.17: Predictive relationship to estimate the crop coefficient, K_c, from the sum of NDVI+NDWI.

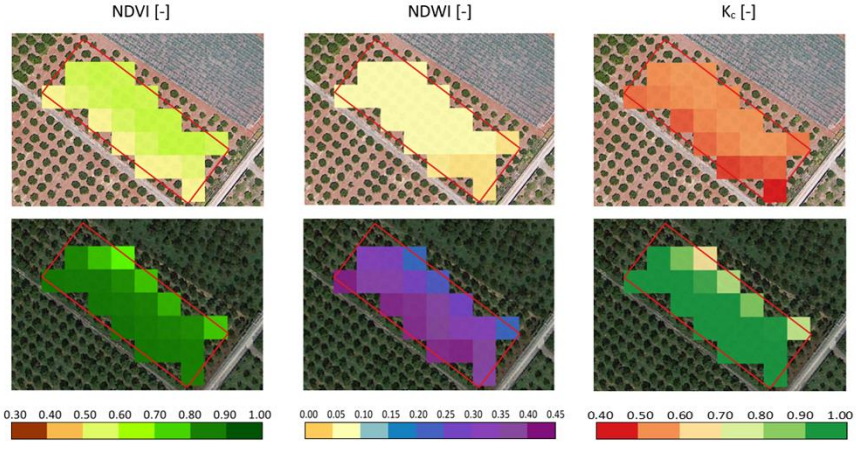

Figure 5.18: Maps of NDVI and NDWI obtained from Sentinel-2 acquisitions and corresponding K_c estimated from eq. (5.1) in two days characterized by the absence (June 20, 2019, upper row) and the presence of transpirating cover weeds (December 4, 2019, lower row) on the soil surface.

Figure 5.19 shows the comparison of temporal trends of crop coefficient estimated with eq. 5.1 with those obtained from the literature for citrus orchards characterized by the presence (Allen and Pereira, 2009) and absence (Rallo et al., 2021) of ground weeds. The colours associated with the estimated K_c values depend on the sum of NDVI and NDWI. As it can

be observed, relatively higher K_c were associated with the higher VIs combination, with values close to 1.0, and were obtained from late fall to early spring after the beginning of sprouting, while in the following stage, they were associated with the decrease in the VIs combination.

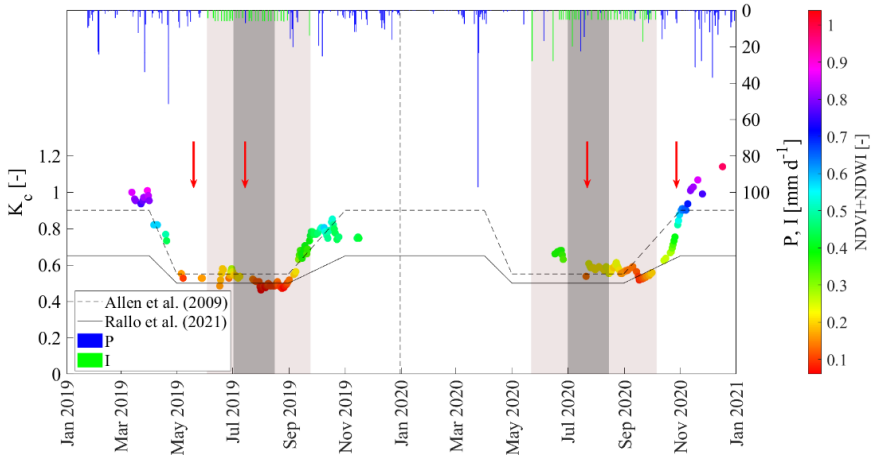

Figure 5.19: Comparison between crop coefficient estimated with eq. 5.1 and the corresponding curves suggested by Allen et al. (2009) and Rallo et al. (2021). The colours associated with the experimental values depend on the combination of NDVI and NDWI. The light grey box indicates the irrigation season, while the dark grey identifies the period of application of water deficit (DI). Precipitation, *P*, and Irrigation events, *I*, are indicated in the secondary axes.

On the other hand, during the irrigation season, under absent or scarce precipitation, the estimated K_c associated with the relatively lower combination of VIs, resulted in about 0.55; finally, after the end of irrigation, the rise in the estimated K_c, was associated with increased values of the VIs and can be justified by the development of ground weeds among the plant rows. In 2020, the late growth season started later than in 2019, because of a high pluviometric deficit characterizing the mid-season 2020. Similar annual patterns of crop coefficient have been recently reported by Puig-Sirera et al. (2021) for an olive orchard and by Segovia-Cardozo et al. (2022) in a citrus orchard in which, focusing on the full year and not only on the growing season, it was observed that K_c values in non-growing periods resulted in higher values than in the growing period, due to the large contribution of soil evaporation.

5.3.4 Application of FAO56 Agro-Hydrological model

For the Villabate field, the FAO56 Agro-Hydrological model was implemented in a spatially distributed mode to estimate the SWB with a 10 m spatial resolution. However, considering that SWC measurements were acquired in only four trees, while ET_a measurements involved the entire field, the validation of the spatially distributed FAO56 model was performed at field scale using the average of the output pixel values falling inside the perimeter of the study area. In this way, the results of the pixel-based FAO56 procedure were aggregated at a field scale where evapotranspiration and SWC measurements were carried out.

To give an example, figure 5.20 shows the maps of simulated soil water content, SWC_{sim} and actual evapotranspiration, ET_a, retrieved from the application of the FAO56 Agro-Hydrological model on two different days, i.e., on June 20, 2019, and December 4, 2019, respectively, in the absence and presence of active weeds on the soil surface.

During these two days, the average, ET_a, resulted equal to 3.27 mm d^{-1} and 1.27 mm d^{-1}, with a standard deviation of 0.17 mm d^{-1} and 0.13 mm d^{-1}, respectively. Moreover, on the same days, the average SWC_{sim} resulted equal to 0.19 ± 0.00 $cm^3\,cm^{-3}$ and 0.27 ± 0.01 $cm^3\,cm^{-3}$, respectively. The value of K_c was close to 1.0 on days in which weeds were present on the soil surface determining values of ET_a fairly close to the corresponding ETo.

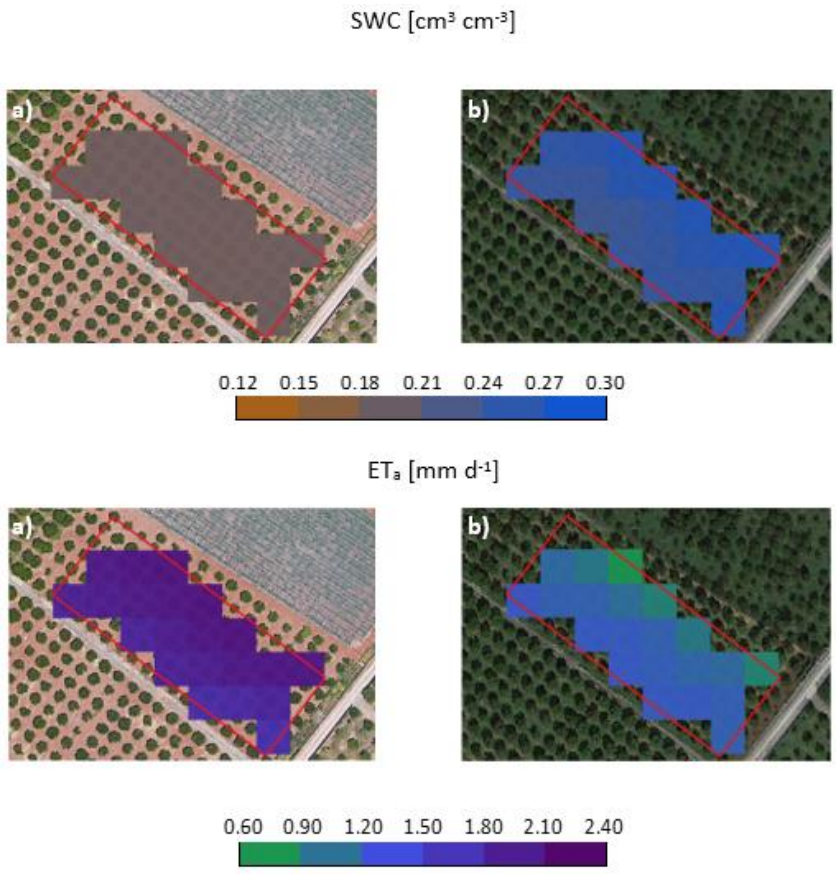

Figure 5.20: Examples of maps of simulated soil water content, SWC_{sim}, and actual evapotranspiration, ET_a, obtained in the absence (a, June 20, 2019) and presence (b, December 4, 2019) of active weeds among the tree rows.

The results of the FAO56 model simulations applied at the field scale for the three years (from 17 May to 30 September) are reported in figure 5.21. The upper row illustrates the comparison between measured, SWC_{avg} and simulated, SWC_{sim}, soil water contents, the second row shows the SWC distribution in the soil layer 0-0.50 m where the active root system is developed, whereas the third row shows the dynamic of crop reference evapotranspiration, *ETo*, in the three years, as well as measured, ET_{a_meas} and simulated, ET_{a_sim} actual evapotranspiration.

The daily values of measured SWC of the entire experimental field were calculated as the mean of the values acquired in layer 0-0.50 m by the four

probes installed in the plot. A fairly good agreement can be observed between simulated and measured SWC in the root zone, negligible discrepancies can be noticed, mainly after rainfall events and, for 2018 and 2020, around the final periods of simulations, when a slight overestimation of simulated SWC occurred. Regarding the temporal dynamics of SWC profiles, it is interesting to notice that water applications with the SDI system increased only the SWC at depths ranging from 0.30 m to 0.50 m, whereas the upper soil layer remained generally dry.

For the two years in which measured ET_a values were available, the trends of simulated values followed, in general, those of the corresponding measured, even if a slight underestimation can be observed in the initial period of simulation of 2019, probably due to rapid SWC depletion consequent to the absence of rainfall events in the period.

The lower row of figure. 5.21 shows the trend of measured and simulated K^*_c, whose values which were in a fairly good agreement. During irrigation seasons, excluding the short periods of crop water stress, K_c values ranged between 0.47 and 0.76, in line with the tabulated values of 0.50 and 0.82 suggested by Allen et al. (1998) for a citrus orchard characterized by a fraction cover of 30%, respectively, in absence and presence of active ground cover or weeds. Moreover, an indicative value of the mid-season crop coefficient, equal to 0.55 ± 0.50, has been recently confirmed by Rallo et al. (2021) for low density citrus orchards characterized by a fraction cover between 25 and 40% and with a plant height between 2.3 and 4.5 m.

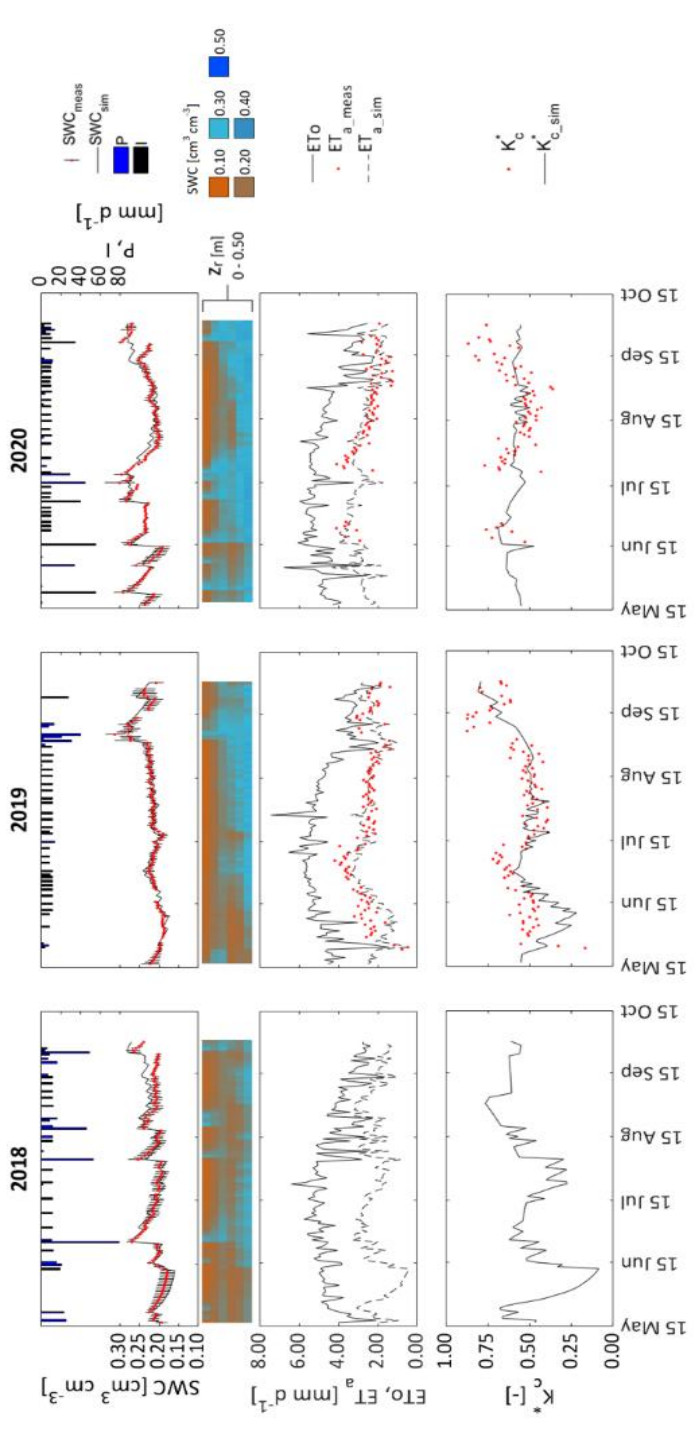

Figure: 5.21: Temporal dynamics of average and standard deviation of measured SWC_{meas} and corresponding simulated, SWC_{sim}, precipitation, P, amount of irrigation, I (upper row) and detail of soil water contents measured each 10 cm depth in the layer 0-50 cm (second row); temporal dynamics of crop reference evapotranspiration, *ETo*, and of measured, ET_{a_meas}, and simulated actual evapotranspiration, ET_{a_sim}, (third row); temporal dynamics of measured and estimated Kc* (lower row) for the simulated periods of 2018, 2019 and 2020.

The performance of the K_c(VI) relationship implemented in the FAO56 Agro-Hydrological model was evaluated based on the statistical parameters associated with simulated and measured SWC and ET_a, reported in table 5.6 for the periods of observation.

Table 5.6: Results of the statistical analysis to check the FAO56 model performance.

	SWC					
	RMSE	*MBE*	*PBIAS*	R^2	*b*	*NSE*
	[cm³/cm³]	[cm³/cm³]	[%]	[-]	[-]	[-]
2018	0.01	0.00	-1.30	0.74	1.01	0.40
2019	0.01	0.00	-0.49	0.86	1.00	0.85
2020	0.01	0.00	-2.11	0.80	1.02	0.76
	ET_a					
	[mm/day]	[mm/day]	[%]	[-]	[-]	[-]
2019	0.57	-0.26	10.36	0.44	0.88	0.21
2020	0.40	-0.01	0.22	0.70	0.98	0.68

The model allows very accurate predictions of daily SWC, with RMSE equal to 0.01 cm^3 cm^{-3} and the absence of bias, because of the good agreement between the average SWC measured in the root zone and the corresponding ones simulated by the model. The goodness of the proposed K_c(VIs) relationship is also confirmed by the high R^2 values, the *b* coefficient slightly higher than 1 and the always positive NSE. However, the negative values of PBIAS obtained in the three years of simulation indicate a weak tendency of simulated values to be higher than the corresponding observed ones. On the other hand, the simulated values of ET_a, were characterized by RMSE equal to 0.57 mm d^{-1} and 0.40 mm d^{-1}, MBE of -0.26 mm d^{-1} and -0.01 mm d^{-1} and PBIAS of 10.40 and 0.20 for 2019 and 2020, respectively. The high values of regression coefficient *b* (higher than 0.88), and the positive NSE index, are acceptable for practical application aimed at irrigation scheduling and ET_a estimation.

5.4 ET estimation at the Irrigation District 1A – Castelvetrano

5.4.1 In situ measurements: Climatic characterization

For the three years of observation (2018-2020), the climatic characterization was carried out using weather data acquired by the Castelvetrano (ID=302) standard weather station owned by SIAS, located within the irrigation district 1A. This weather station provides, hourly climate data such as: air temperature, T_a (°C), relative air humidity, RH (%), R_s (MJ m^{-2} h^{-1}), wind speed and direction at 2 m and 10 m above the soil, U_2 and U_{10} (m s^{-1}) as well as rainfall heights, P (mm).

Figure 5.22 shows the daily values of the T_{max}, T_{min} and relative air humidity, R_s, U_2 and U_{10}, as well as, the values of daily ETo, evaluated using the FAO56-PM equation (eq. 2.30) and the daily and cumulative rainfall heights.

In the three-year observation period (2018-2020), the annual trend of R_s remained almost similar, assuming values that are quite usual for the study area, with maximums of around 30 MJ $m^{-2}d^{-1}$ in July and minimum values of around 2 MJ $m^{-2}d^{-1}$ during the winter period (December-January). The air temperature trend also followed a similar dynamic to the R_s, with annual T_{max}, between 10 and 40 °C and minimums between 1 and 25 °C. Precipitation for the three years of observation was 889 mm (2018), 651 mm (2019) and 557 mm (2020) respectively, concentrated in the periods between January and May and between September and December.

ETo, was around 1 mm d^{-1} in January, increased in the first half of each year, reaching peak values of around 7 mm d^{-1} in the summer period and decreased in the following period, reaching minimum values of around 1 mm d^{-1} in December.

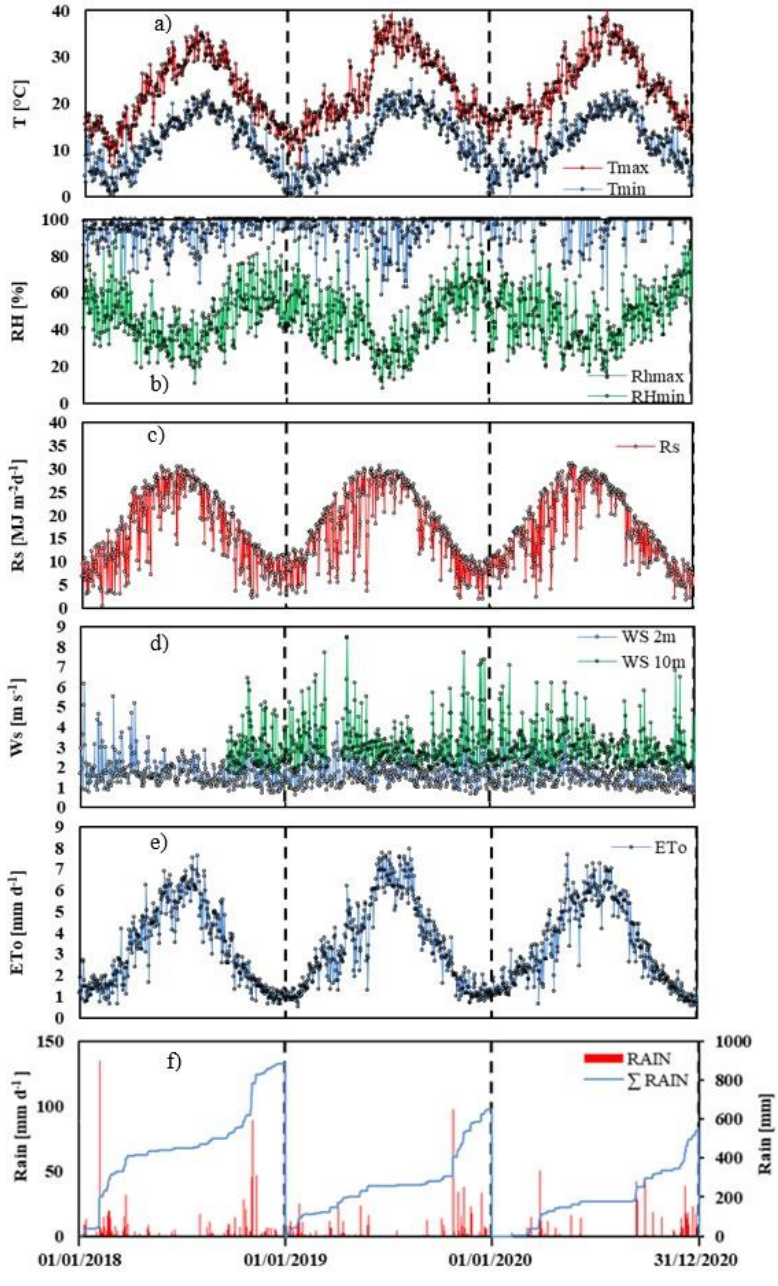

Figure 5.22: Daily temporal dynamics of maximum and minimum air temperatures a), relative air humidity b) solar radiation c), wind speed d), crop reference evapotranspiration e) and precipitation f) for the three years of observation (2018-2020).

During the three years of observation (2018-2020) figure 5.23 shows that the annual value of precipitation was rather variable, while the atmospheric evapotranspiration demand was almost constant with value about to 1200 mm.

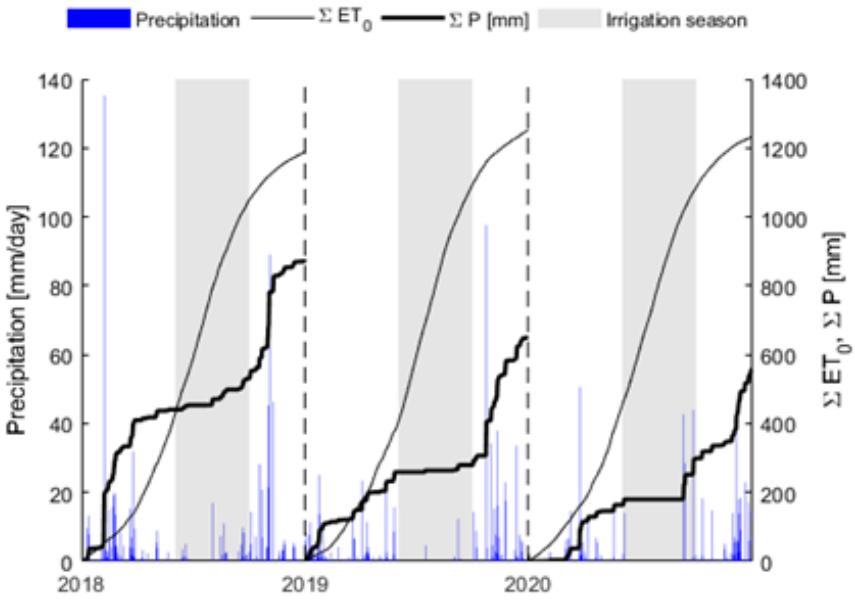

Figure 5.23: Temporal trend of the cumulative values of reference crop evapotranspiration and rainfall over the three-year period 2018-2020.

For the period analyzed, the pluviometric deficit was valuated referred to the whole year, as well as, for the irrigation season (01/06 – 30/09). Table 5.7 summarizes the annual cumulative *ETo*, rainfall, as well as the pluviometric deficit referred for the reference periods.
With reference to the different meteorological contributions over the three years, the lowest pluviometric deficit was in 2018 and the highest in 2020.
Instead, when considering the three irrigation seasons, the pluviometric deficit was lowest in 2020, because the significant rain events occurred at the beginning and end of the irrigation season.

Table 5.7: Cumulated values of crop reference evapotranspiration, rainfall and pluviometric deficit annual and during the irrigation season (01/06 - 30/09).

Year	*Year*			*Irrigation season (01/06 - 30/09)*		
	∑ P [mm]	∑ ETo [mm]	∑ (P-ETo) [mm]	∑ P [mm]	∑ ETo [mm]	∑ (P-ETo) [mm]
2018	889	1188	-299	90	630	-540
2019	651	1253	-602	20	695	-675
2020	557	1232	-675	134	639	-505

5.4.2 Analysis of irrigation volumes database

The analysis of distributed irrigation volumes together with the pluviometric deficit made allow to identify possible irrigation strategies adopted by the farmers.

With reference to the period 2009-2020, table 5.8 shows the volume delivered through the irrigation district, the irrigated surface, the overall water supply in the district, as well as the annual pluviometric deficit.

Table 5.8: Pluviometric deficit and water supply within the irrigation district 1A for the period 2009-2020.

Year	Volume delivered [m^3]	Irrigated surface [ha]	water supply [$m^3\ ha^{-1}$]	∑ P [mm]	∑ ETo [mm]	∑ (P-ETo) [mm]
2009	746774	1187	629	915	1184	-269
2010	830273	1169	710	747	1189	-442
2011	923303	978	944	568	1226	-658
2012	1216230	1173	1037	580	1373	-793
2013	677338	978	693	813	1277	-464
2014	1010033	1013	997	638	1279	-641
2015	831181	1090	763	822	1274	-452
2016	705136	956	738	598	1313	-715
2017	1061626	1066	996	589	1288	-699
2018	713360	887	804	889	1188	-299
2019	880631	891	988	651	1253	-602
2020	952226	994	958	557	1232	-675

Table 5.8. shows a significant variability in water supply with minimum and maximum of 677338 m^3 and 1216230 m^3 for 2013 and 2012, respectively. It is also important to highlight that despite a total area of about 3000 ha in the irrigation district, only about 1000 ha are frequently irrigated. This suggest that a high percentage of farmers provide the irrigation volumes from unauthorised well or undeclared drawing.

The water supply between the years was slightly variable with an average value equal to 855 m^3 ha^{-1}. Figure 5.24 shows the water supply as a function of the annual pluviometric deficit in the irrigation district, for the period 2009 -2020.

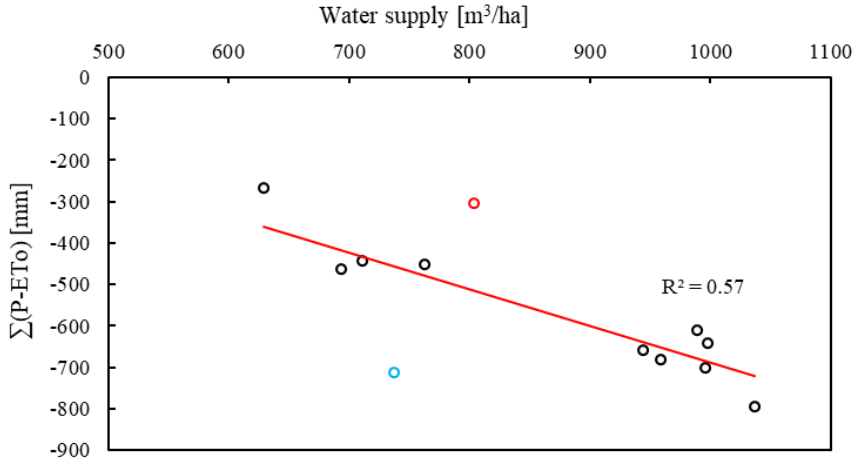

Figure 5.24: Trend between total pluviometric deficit and total volume delivered within the irrigation district 1A.

As showed in figure 5.24 a correlation between total pluviometric deficit and water supply exists, R^2 equal to 0.57. Only two points referred to 2016 (blue dot) and 2018 (red dot) do not follow the trend. For 2016, the pluviometric deficit and water supply were equal to -715 mm and 738 m^3 ha^{-1}, respectively. Whereas for 2018, the pluviometric deficit and water supply were equal to -299 mm and 804 m^3 ha^{-1}, respectively. These results could be explained by an intensive rainfall event occurred at the beginning of June in 2016 (33.4 mm d^{-1}) and in the middle of August in 2018 (45.0 mm d^{-1}). The trend shown in figure 5.24, suggests that the irrigation

management strategies adopted by the farmers, are based on the actual weather condition.

When considering only the olive orchards within the irrigation district 1A, the figure 5.25 shows the total water supply in the district for the irrigation seasons 2018-2019 and 2020.

The distribution of the water supply shown in figure 5.25, along the three irrigation seasons, highlights a certain regularity in the temporal distribution of the water supply, with maximum water consumption in August and minimum at the beginning and end of the irrigation season. For the irrigation season of 2018, the maximum water consumption occurs in September, due to an intense rainfall event (45 mm d^{-1}) in middle of August, which reduced the water supply by the farmers. Therefore, the farmer's irrigation strategies are strongly influenced by the weather condition.

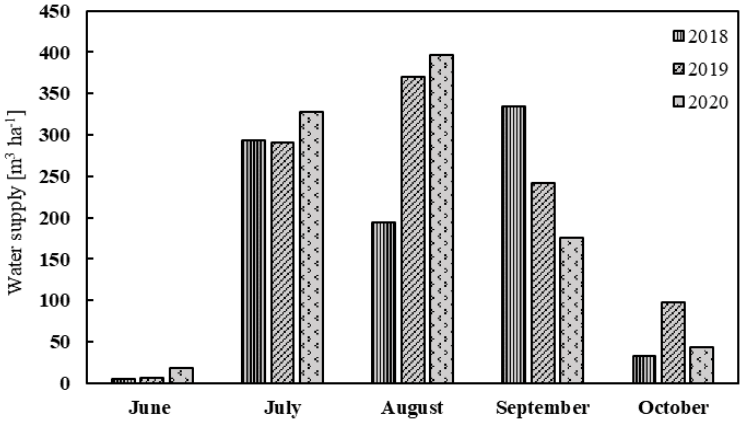

Figure 5.25: Monthly water supply measured in the irrigation district 1A referred to the olives orchards during the irrigation seasons 2018, 2019 and 2020.

5.4.3 Remote sensing data: Temporal dynamics of vegetation indices

Based on the Sentinel-2 MSI level 2A database, the NDVI was calculated for the entire district. Figure 5.26 shows the spatial distribution of the NDVI over the irrigation district.

As it can be noted from figure 5.26, the NDVI shows a wide heterogeneity among the crops in the irrigation district. In particular, the NDVI values are

higher than 0.50 in areas with high leaf density; for sparsely vegetated areas, they ranged between 0.20 to 0.50.

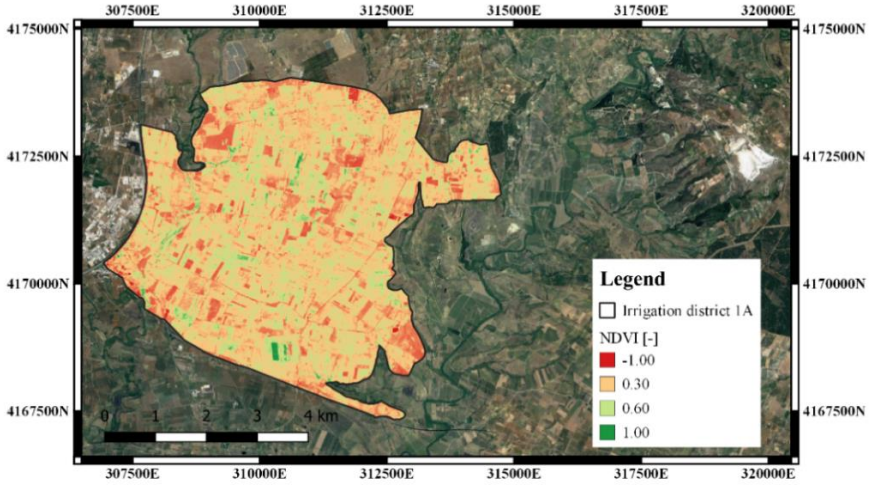

Figure 5.26:Spatial distribution of NDVI, over the irrigation district 1A (11/08/2018).

As an example, figure 5.27 shows the spatial distribution of the NDVI over the farm coded as 1A.9_002.

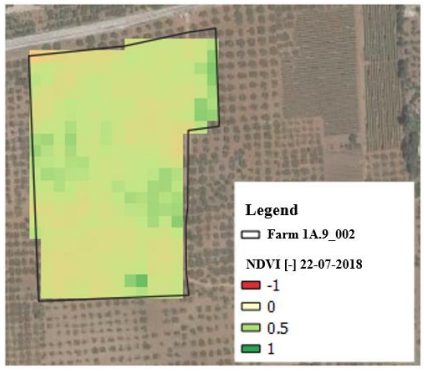

Figure 5.27: Spatial distribution of the NDVI over the 1A.9_002 farm relative to the acquisition date 22-07-2018.

The analysis of figure 5.27 shows a certain variability within the farm, whit the predominant values ranging between 0.20 to 0.50, with sporadic areas characterized by values higher than 0.50.

For the same farm, the temporal dynamic of the NDVI is reported in figure 5.28.

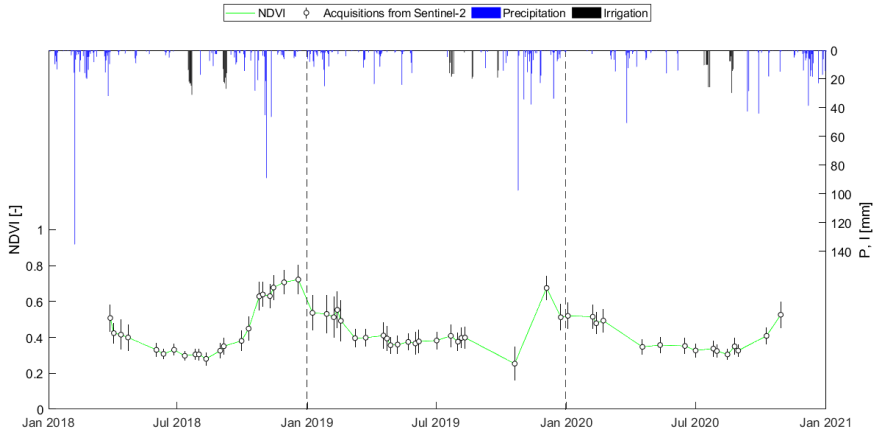

Figure 5.28: Temporal dynamic of the NDVI during the analysis period (2018-2020).

During the 2018 irrigation season, the value of NDVI remains quietly constant at around 0.37, and then increases to reach a maximum value equal to 0.77 in December. The behaviour during the 2019 irrigation season is different, as the NDVI index value grows linearly from a minimum value similar to the 2018 to reach a value equal to 0.67 at the end of the irrigation season.

5.4.4 Estimation of the basal crop coefficient for olive orchards, based on fraction cover and height crops

The estimation of the basal crop coefficient, K_{cb}, following the A&P approach (Allen and Pereira, 2009), requires the knowledge of the fraction cover and the height of the crops. The fraction cover, f_c, for both polygons database shown in figure 4.1, was calculated as the product between the value representative of the plant canopy surface in the plot and the number of plants within the plot.

As an example, figure 5.29 shows the mean and the standard deviation of the canopy surface with the increase of the number of the plants in the plot, the representative of the plant canopy surface, for the examined polygon, is also shown.

In figure 5.29, it is possible to argue that, after a certain number of plants, the average area of the canopy and the relative standard deviation reaches a constant value. Therefore, this value can be assumed as representative of all the plants, in the plot. This procedure was applicated for each polygon of the database.

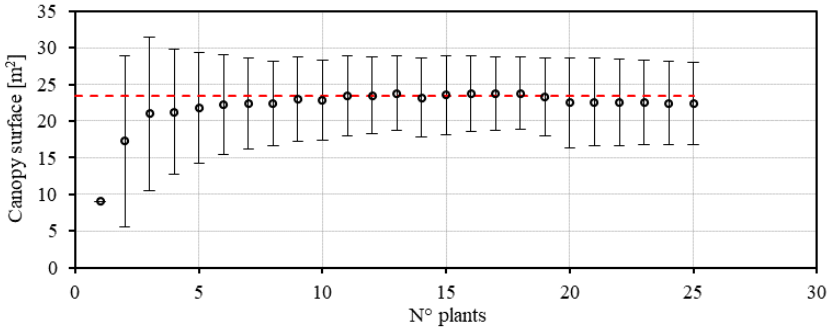

Figure 5.29: Mean and standard deviation of the canopy surface with the increase of the number of the plants in the plot.

The values of f_c were correlated with the corresponding values of NDVI and figure 5.30 shows the scatterplots between f_c and NDVI for each plot considered.
The values of f_c ranged between 0.02 to 0.71 and the NDVI ranged from 0.15 to 0.78 with the maximum and minimum values for the standard deviation equal to 0.23 and 0.00, respectively.
A linear relationship was obtained to predict the fraction cover from the VI.

$$fc = 1.21\text{NDVI} - 0.17 \tag{5.2}$$

The linear relationship (eq. 5.2) is supported by an R^2, equal to 0.80, this result is in according to several authors that have been confirmed the good relationship between f_c and NDVI (Carlson and Ripley, 1997; Gutman and Ignatov, 1998; Ric Baret et al., 1995).

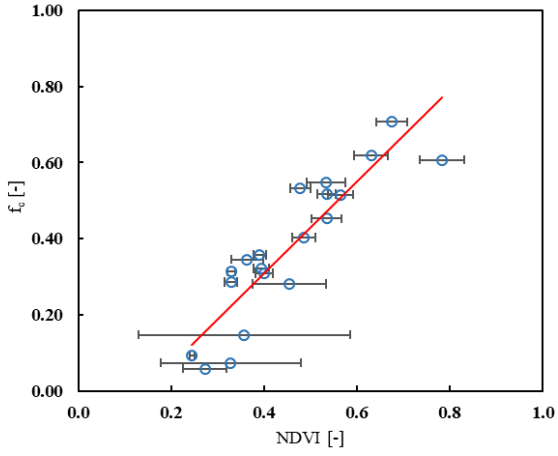

Figure 5.30: Scatterplot between fraction cover and NDVI.

The performance of the predictive relationship (eq. 5.2) was evaluated based on the statistical parameters associated with the correspondence values of f_c retrieved by GEP software. The statistical analysis was carried out by means of the RMSE, MAE and slop of regression line, b, whose values were 0.10, 0.08 and 0.85, respectively. The results confirm that the linear relationship can be a useful solution to estimate the f_c from NDVI values. Similar results were obtained for different crops in China. In their study, Ding et al. (2016) analysed different approaches using dimidiate pixel models to obtain f_c values from NDVI, retrieved by Landsat 8 OLI images, for steppe and corn. They obtained values of R^2 and RMSE equal to 0.96 and 0.11, respectively, for steppe and 0.72 and 0.08, respectively, for corn. Zhang et al. (2019) analysed the correlation between the f_c and the VI, retrieved by Landsat 8 operation land imager (OLI) images, for dessert, steppe, meadow, and mixed vegetation. They found values of R^2 equal to 0.85 for dessert, 0.73 for steppe, 0.82 for meadow and 0.73 for mixed vegetation. Finally, the linear relationship between measured f_c and NDVI, retrieved from World-View 3 high resolution image, showed in Ma et al. (2021), value of R^2 equal to 0.89 for corn, wolfberry and rice.

The basal crop coefficient, K_{cb} obtained, for each plot, through the A&P procedure, were correlated with the corresponding value of NDVI. Figure 5.31 shows the scatterplot representing the basal crop coefficient K_{cb}, as a

function of the NDVI the predictive relationship, expressed by the following linear function is characterized by R^2 = 0.98:

$$K_{cb} = 1.25\,\mathrm{NDVI} - 0.14 \tag{5.3}$$

The high value of R^2, suggest that the functional relationship can be a suitable solution to estimate basal crop coefficient, K_{cb} for olives orchards in different fraction cover condition. The functional relationship obtained resulted in according with those reported in a review published by Calera et al. (2017) for many crops and the most common techniques to assess CWR based on remotely sensed data. Contrary with the results obtained by Mateos et al. (2013), in which used the Soil Adjusted Vegetation Index (SAVI) to assess K_{cb}, the linear relationship K_{cb}(NDVI) is an useful tools to assess, crop water requirements with suitable temporal and spatial resolution.

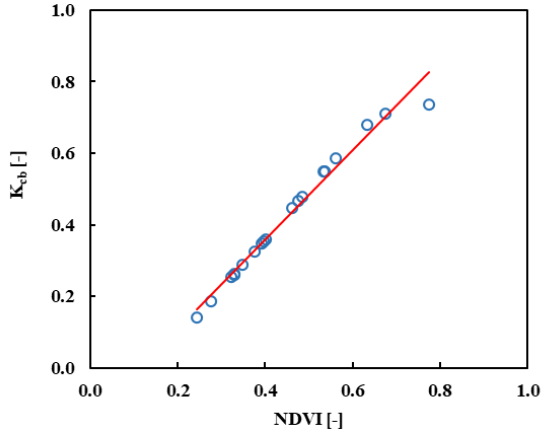

Figure 5.31: Predictive relationship to estimate the basal crop coefficient, K_{cb}, from the NDVI vegetation index.

5.4.5 Applications of FAO56 model in Water Uses Mode (WUM)

The functional relationship (eq. 5.3) together with the time series of NDVI and some ancillary data retrieved from weather station were implemented in the model and run, in water uses mode (WUM).
The model was applied to the farms identify as WUM (fig. 4.6) selected to derive the average management parameters adopted by the farmers of the

irrigation district from April to September in 2018. In this case the irrigation volumes applied by the farmers were used as input of the simulation.
The model outputs were represented by maps describing the spatial distribution of crop coefficient, K_c, actual evapotranspiration, $ET_{a,}$ and SWC, for all day of the simulation. Moreover, the temporal dynamic of SWC, *ETo*, ET_a, K_c and K_s are also available.
The application of the model in WUM, allowed to determinate the threshold of the irrigation water supply and the percentage of the SWC re-established after irrigation. Even if the model was applied to all selected farms, for the WUM applications (fig. 4.6), the results for the farm coded as 1A.9_002 (fig.5.32), implanted with olives with an extension of about 3.00 ha, are used as example to present model application and achieved results.

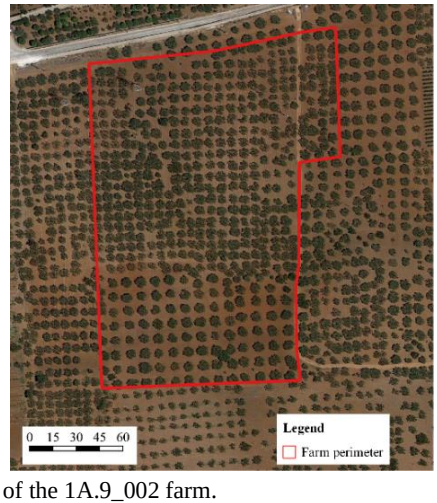

Figure 5.32: Perimeter of the 1A.9_002 farm.

In figure 5.33, the upper row illustrates the temporal dynamic of the SWC, the second row the *ETo* and ET_a, while the third and fourth rows shows K_c and K_s.

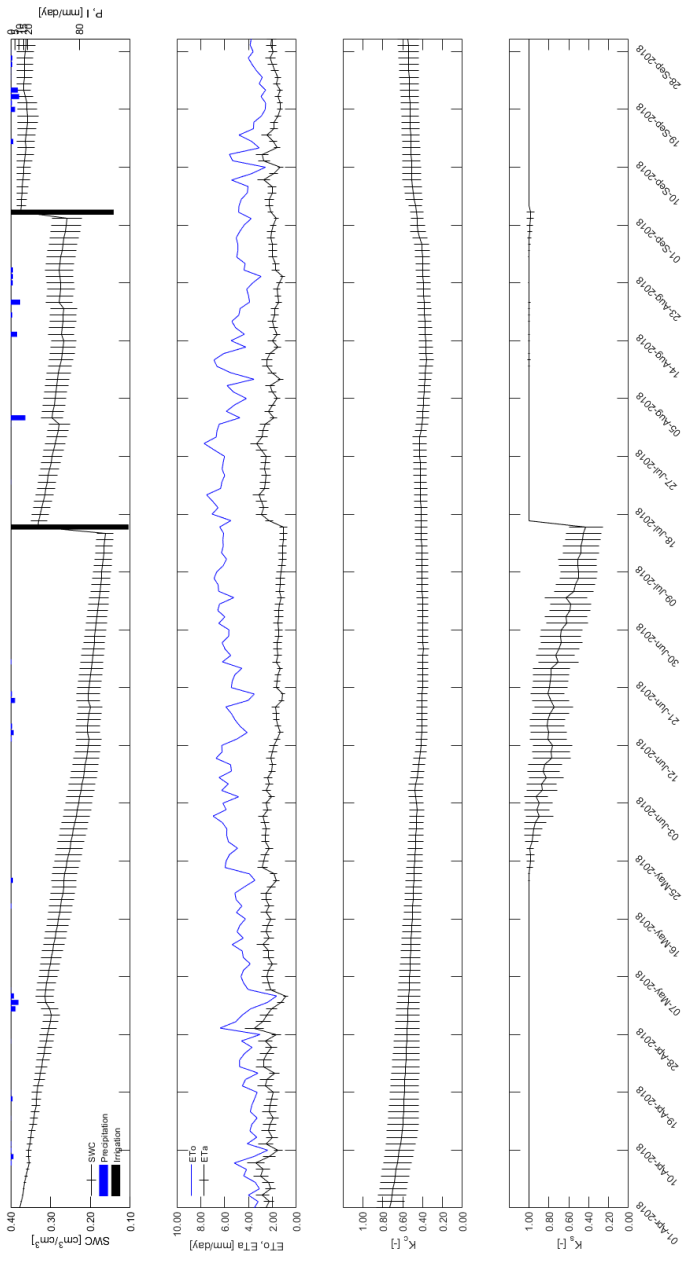

Figure 5.33: Temporal dynamics of average and standard deviation of simulated, SWC, precipitation, P, amount of irrigation, I (upper row); temporal dynamics of crop reference evapotranspiration, ETo, and simulated actual evapotranspiration, ET_a, (second row); temporal dynamics of estimated Kc (third row);temporal dynamics of estimated K_s (fourth row) for the simulated period (01-04-2018 to 30-09-2018).

The daily values of simulated SWC in the root zone follows the thermo-pluviometric trend of the period. After long periods without precipitation, the SWC reaches values below 0.15 cm^3cm^{-3}, it increases after the rains and irrigation.

For the period studied, the temporal dynamic of ET_a follows the atmospheric water request expressed as *ETo*. The minimum value, around to 1.00 mm d^{-1}, was observed at the end of a long period without precipitation, where the high atmospheric water demand and low SWC reduce the transpiration capacity of the plants.

The third row of figure. 5.33 shows the trend of simulated K_c. During irrigation seasons, K_c was about 0.45, slightly lower than 0.50 obtained by Cammalleri et al. (2013a) for an olives orchard characterized by a fraction cover of 35%.

In the lowest row of the figure 5.33, the temporal dynamic of the simulated K_s is also shown. The values of K_s equal to 1.00 for most of the examined period, identifying conditions of non-water stress (Allen et al., 1998), except for the periods where the SWC ranges between 0.27 $cm^3\ cm^{-3}$ (negligible water stress condition) to 0.16 cm^3cm^{-3} (maximum water stress condition).

The model used in WUM allowed to estimate the ET_a consumption of the crops according to the management strategy applied by the farmers, as well as, the management parameters.

With reference to the management parameters, the results of the 33 simulations allowed to identify the parameters adopted by the farmers. Table 5.9 summarizes the threshold of the irrigation water and the percentage of the SWC re-established after irrigation, expressed as percentage of the TAW.

Table 5.9: Farmer's irrigation management parameters

Variable	[% TAW]
threshold irrigation water apply	75 ± 15
irrigation dose	15 ± 18

5.4.6 Application of FAO56 model in Water Requirement Mode (WRM)

The management parameters (tab.5.9) obtained with the model in WUM, were then implemented in the model for the farms (fig.4.6) to run the simulations in WRM mode; the values of the variables for the simulation are summarized in Table 5.10 and converted in millimetres.
For the simulated period, the model outputs were represented by maps of crop water requirement, expressed by ET_a, SWC, in the root zone, K_c and K_s. Moreover, for each considered farm, the model provides the irrigation calendar.
The model was applied to the 33 farms identified as WRM (fig. 4.6), from April to September 2018 and 2019. Initially, 2020 was also included but the poor quality of the irrigation volumes distributed data provides by the "Consorzio di Bonifica", was a drawback in the model application in fact, it was impossible to validate the results of the simulation.

Table 5.10: Values for the variables used for FAO56 model simulations.

Model variables	Unit	Value
INPUT		
Start simulation	[-]	01/04/2018
End simulation	[-]	30/09/2018
Root depth	[m]	0.80
SWC_0	$[cm^3cm^{-3}]$	0.80 θ_{fc}
MANAGEMENT PARAMETERS		
Threshold irrigation water apply	[mm]	160 ÷ 220
Irrigation dose	[mm]	30 ÷ 45

The model was applied to all farms selected, for the WRM applications (fig. 4.6). The results for the olives farm coded as 1.16_003 (fig.5.34), with an extension of 1.64 ha, are used as example to describe model application.
The farm under examination is represented by an uneven-aged olive grove, with plants in the north area about nine years younger than those in the southern part and along the perimeter. This plant's distribution could cause different response in the model outputs. The figure 5.35 shows the results of a simulation referred to the 1.16_003 farm, the first row (fig. 5.35a-c)

illustrates the SWC spatial variability, while the second row (fig. 5.35d-f) the ET_a, spatial variability.

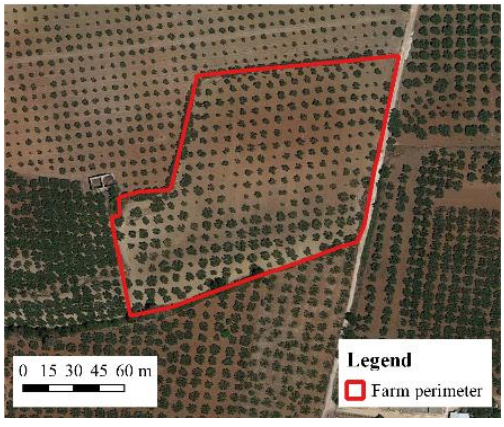

Figure 5.34: Perimeter of the 1.16_003 farm.

The dates were chosen to show the response of the model in the three different conditions after a rainfall event (07-05-2018) of 18.6 mm, at the end of a drying period (24-06-2018) and finally, after an irrigation of 23 mm (23-07-2018). The figure 5.35a-c shows that in general, the SWC is fairly uniform over the entire area. In particular, for the three different examined dates the average values of SWC were 0.31 $cm^3\,cm^{-3}$, 0.19 $cm^3\,cm^{-3}$ and 0.20 $cm^3\,cm^{-3}$ 0.19 $cm^3\,cm^{-3}$ respectively. As it was expected, the average SWC after the rain event or irrigation was higher than after the drying period. These results suggests that the model could be a useful tool to monitoring the soil water status. With reference to the spatial variability of the ET_a, (fig. 5.35d-f), it is interesting to note how the two portions of the field were characterized by different values, being higher in the south portion. This particularity can be attributed to the differences in K_c values estimated by the NDVI index, which were lower in the younger olive grove. The upper panel of figure 5.36 shows the temporal dynamic of the SWC, the second panel shows the *ETo* and ET_a, while the third and fourth panels shows the K_c and K_s.

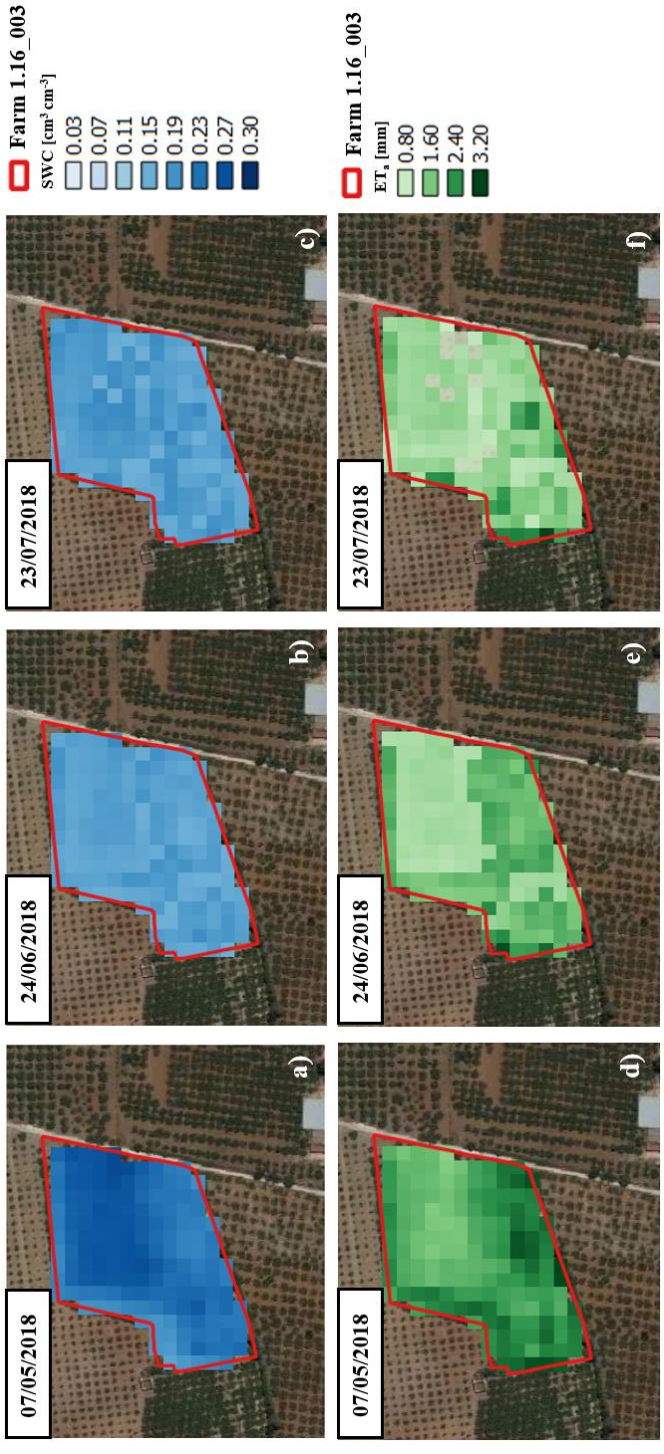

Figure 5.35: Examples of maps of simulated soil water content, SWC, (upper row) and actual evapotranspiration, ET_a, (lower row) for the dates (07/05/2018), (24/06/2018) and (23/07/2018) representative of three different conditions after rain event, after drying period and after irrigation intervention, respectively.

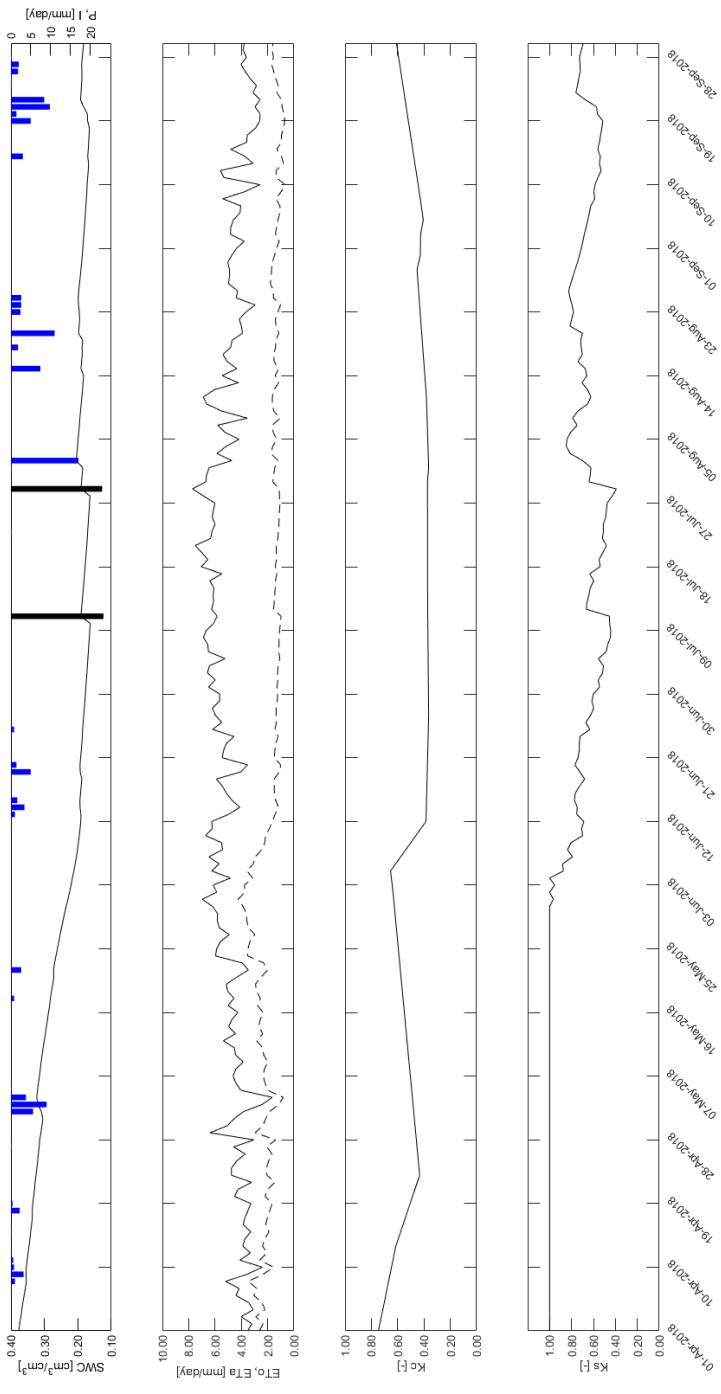

Figure 5.36: Temporal dynamics of average of simulated, SWC, precipitation, P, amount of irrigation, I (upper row); temporal dynamics of crop reference evapotranspiration, *ETo*, and simulated actual evapotranspiration, ET_a, (second row); temporal dynamics of estimated *Kc* (third row);temporal dynamics of estimated K_s (fourth row) for the simulated period (01-04-2018 to 30-09-2018)

The analysis of figure 5.36 (upper panel) shows the temporal dynamic of SWC after a rainfall event or irrigation. In these cases, the model responds with a quick increase in the simulated value.
Regarding to the temporal dynamic of the simulated ET_a, (fig. 5.36 second panel), the trend agrees with that of SWC, and a reduction in SWC corresponds to a reduction in ET_a.
The third panel of figure. 5.36 shows the trend of simulated K_c. During the irrigation seasons, the average value of K_c was about of 0.50, equal to the value obtained by Cammalleri et al. (2013a) for an olive orchard characterized by a fraction cover of 35%.
In the lowest panel of the figure 5.36, the temporal dynamic of the simulated K_s is also shown. As it can be observed, the values of K_s at beginning of the simulation the value is equal to 1.00, identifying conditions of non-water stress (Allen et al., 1998), while K_s is below 1 in the periods where the SWC range between 0.22 cm^3cm^{-3} (negligible water stress condition) until to 0.16 cm^3cm^{-3} where it reaches the maximum water stress condition.

5.4.7 Irrigation depth estimates by FAO56 Agro-Hydrological model and irrigation delivered to hydrants

The model application in WRM allowed the estimation of crop water demand and, consequently, the irrigation depth for each farm.
The irrigation systems commonly adopted by the farmers in the area is represented by three micro sprinklers installed in a ring located at about 20 cm above the soil. This system allows to wet an area about the 60% of the canopy projection. For this reason, the irrigation depth calculated by FAO56 Agro-hydrological model was slightly reduced to account the wetted area that was assumed equal to 60%.
Before discussing these results, it is important to highlight that some farms for irrigation purpose provide the irrigation volumes from unauthorised well or undeclared drawing. This can explain the large differences sometimes observed, between simulated irrigation depth from FAO56 model and measured values from the hydrants. In addition, the irrigation strategies adopted by farmers are highly variable and strongly dependent on the use of the crop grown. In other words, if the crop is used for oil production, the farmer reduces irrigation to improve the quality of the oil. On the contrary,

if the product is used for table consumption, the farmers increase the irrigation dose to improve the weight of the product. Unfortunately, this detail level was not available for the considered farms, therefore the eventual differences observed in the simulation can be also attributed to this uncertainty. Figure 5.37a,b shows the comparison between the daily measured and estimated irrigation depth referred to the two irrigation seasons. The bar charts in reference to the secondary axis, represents the rainfall events during the considered irrigation seasons.

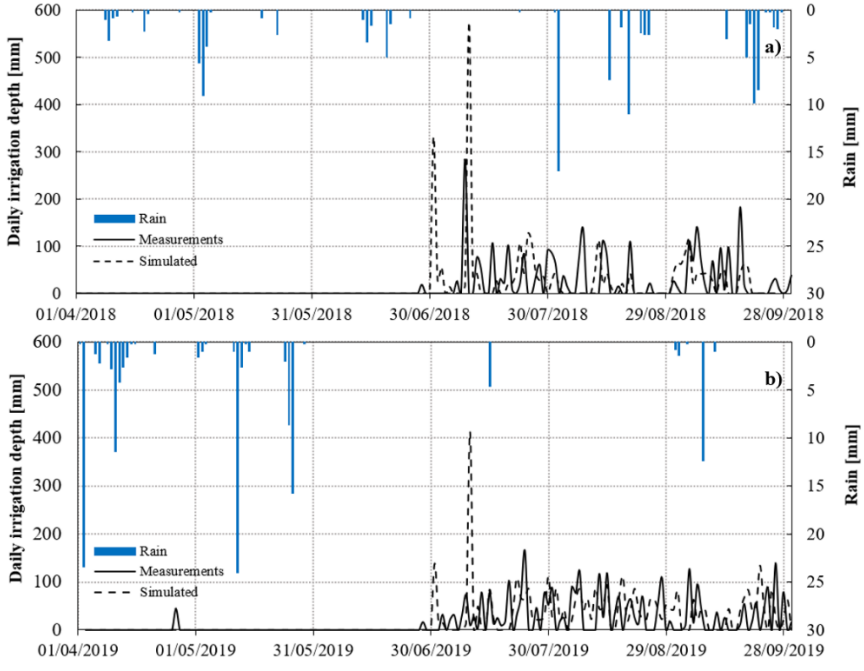

Figure 5.37: Comparison between measured and simulated daily irrigation depth for the two irrigation seasons examined (2018 and 2019), the rainfall events are also shown.

In figure 5.37a it is possible to note that one of the main differences between irrigation depth simulated (dashed line) and measured (continuous line) occurs at the beginning of July, where simulated irrigation depth was higher than the one delivered form the hydrants. A similar result was observed by Minacapilli et al. (2008) who found an overprediction at the start of the irrigation season. For the remaining season, the temporal distribution of simulated irrigation depth follows the thermo-pluviometric conditions while

in some cases, the measured values show the application of irrigation also during rainfall events. This highlights that improper irrigation practices contribute to irrigation water waste. In the 2019 irrigation season (fig. 5.37b), the absence of rainfall events worsens the model's performance with a slightly regular overestimation in simulated irrigation depth. Results on a monthly basis for the two years 2018 and 2019, are shown in figure 5.38a and 5.38b, respectively.

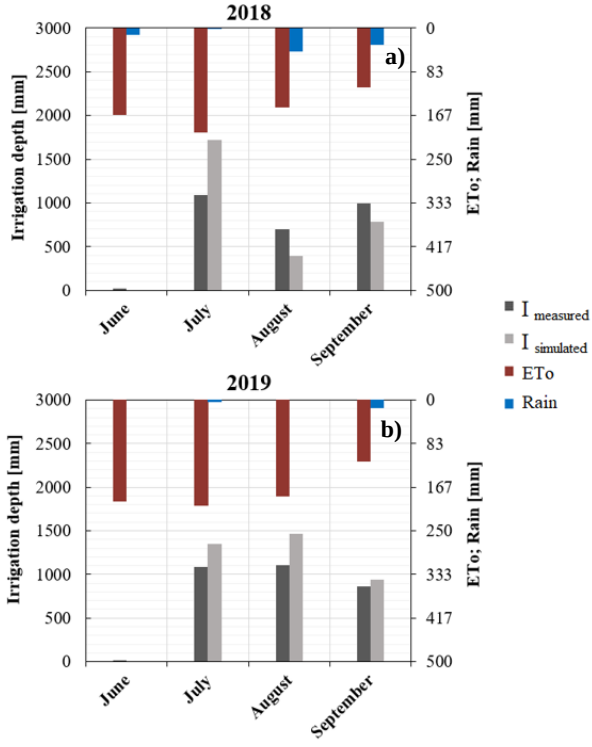

Figure 5.38: Monthly irrigation depth estimated by FAO56 model (mm) (grey bars) *vs.* monthly irrigation depth supplied at hydrants (mm) (black bars), during irrigation seasons 2018 a) and 2019 b). Monthly rain and crop reference evapotranspiration are also indicated in the secondary axis.

The figure 5.38a,b shows the comparison between monthly irrigation depth simulated by FAO56 model and the corresponding monthly water depth supplied by farmers, obtained by integrating the water discharges measured at the hydrants. As it can be observed, for 2018 (fig. 5.38a), it was estimated that an important amount of water could have been saved by following the

FAO56 estimation, except in July when rainfall events were absent or negligible. This effect was confirmed in 2019 (fig. 5.38b), characterized by high atmospheric water demand and absence of precipitation, where the simulated irrigation depth was always slightly higher than that applied. Similar results were observed by Campos et al. (2017), during a study carried out on an irrigated and rain-fed maize and soybean fields in eastern Nebraska (USA). The authors assessed the performance of the functional relationship between K_{cb} and SAVI or LAI proposed by Choudhury et al. (1994) with RMSE lower than 0.7 mm d^{-1}. In terms of simulated irrigation requirement, the authors observed an overestimation of about 15%, mainly during the periods with low precipitation and high atmospheric water demand.

A good agreement was found for the temporal evolution of the cumulative irrigation depth (fig. 5.39a,b) with a difference between simulated and measured seasonal cumulated irrigation volumes of around 3% and 17% for 2018 (fig. 5.39a) and 2019 (fig. 5.39b) irrigation season, respectively.

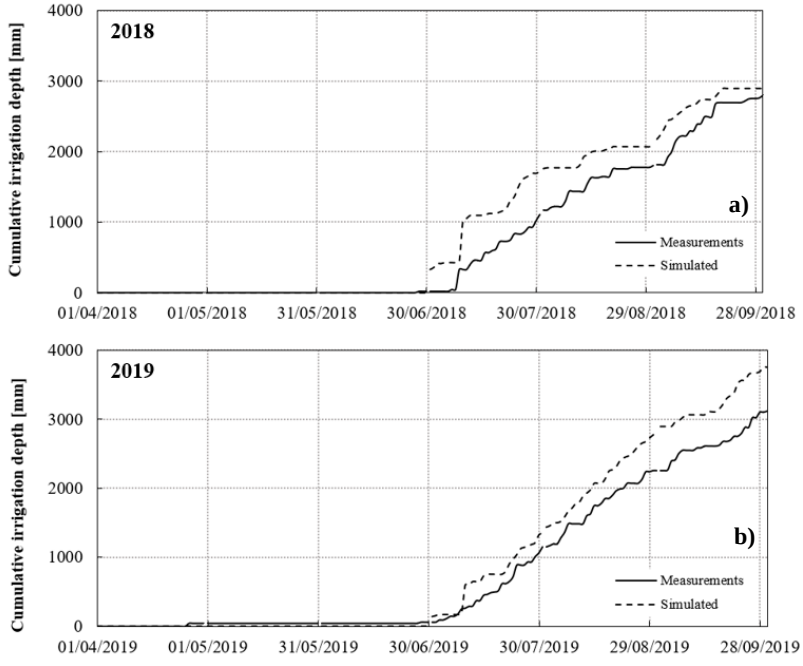

Figure 5.39: Comparison between measured and simulated cumulative irrigation volumes during irrigation seasons 2018 a) and 2019 b).

These results are in agreement with those obtained by Minacapilli et al. (2008) who found, in an irrigation district in Sicily, using the SIMODIS model, a difference from estimated and measured irrigation volumes less than 8%. In conclusion, following the FAO56 estimations, the district could have a tool for supporting the decision in the management of the irrigation water resource.

Chapter 6: Conclusion

For irrigation water management and to improve water use efficiency, reliable climate data measurements and accurate estimations of ET_a, are essential. This concept is crucial to optimize water use in irrigation and reduction of waste of water resource. Therefore, for the different application scales, from fields to irrigation districts, it is important to focus the attentions on innovative techniques that allows reliable irrigation scheduling and to adopt efficient irrigation strategies.

Direct measurements of the main climate data (T_{min}, T_{max}, R_s, RH_{min}, RH_{max}, U_{10}) to estimate the atmospheric water demand are very important to know the upper boundary conditions of the SPA system. In some areas of the world, these measurements are not always available due to limited economic or difficult morphological conditions for the installation of the climatic stations. In this case, the increased availability of reanalysis climate data can be an alternative to access these data and reduce the technological gap.

The EC systems are the most used technique to monitoring the evapotranspiration fluxes from the canopy and soil. However, these systems are subject to improper installation of the sensors or incorrect calibration, as well as the poor maintenance can cause acquisition gaps of one or more sensors and compromises the continuity of actual evapotranspiration records. Recent studies based on ANNs and ML techniques have been demonstrated that these models can be a reliable solution for time series gap-filling and or produce synthetic data series.

Despite the direct measurements of ET_a are most important to know the real crop water requirements, for large scales of application can be costly and time-consuming. For these reasons, remotely sensed data, as earth observation by means MSI can be reliable input data to assess crop water requirements by means the implementation of spatially distributed models.

In this framework, the general context of this thesis can be defined as how the use of remotely sensed data and innovative techniques of data analysis can support the estimation of crop water requirements, at different spatial scales, using spatially distributed model.

In this thesis, the quality of the ERA5-L reanalysis climate variable was evaluated to assess crop reference evapotranspiration, *ETo*, in Sicily, with specific attention to the assessment of the FAO56-PM equation sensibility for the *ETo* estimation. Contextually, over the Villabate citrus orchard and

"Tenuta Rocchette" olives orchard, the performance of the GPR algorithm was evaluated for time series gap-filling of ET_a. For two different crops (citrus and olives) were obtained two functional relationships K_c(VIs). The reliability of these equations was assessed by means the implementation of the FAO56 Agro-Hydrological model to assess crop water requirements for the two different types of crops examined. To this aim, two databases of Sentinel-2 MSI level 2A were obtained and then processed to derive spatial and temporal distribution of the NDVI and NDWI over the study areas. The datasets were used as input of the FAO56 Agro-Hydrological model to estimate spatial and temporal distribution of SWC, actual evapotranspiration, ET_a, crop coefficient, K_c, and stress coefficient, K_s.

Regarding to the assessment of the ERA5-L reanalysis climate variables quality, the comparison between reanalysis climate variables and ground measurement evidenced that ERA5-L database generally is in good agreement with the variables measured on the ground. Specifically, T_{min} and T_{max} and R_s were mostly well estimated, by reanalysis database with overall average RMSE values equal to 2.13 °C, 2.52°C and 2.95 MJ m^{-2} d^{-1}, respectively. With corresponding MBE values equal to 0.50 °C, -1.28°C and 0.95 MJ m^{-2} d^{-1} respectively. On the other hand, the worst variables estimated were RH_{min} and RH_{max} with RMSE equal to 14.14 % and 9.94% and corresponding MBE value equal to 9.94 % and 0.98 %, respectively. Considering that in ERA5-L database the relative air humidity is a function of dew point temperature and air temperature, an improvement in these two variables could better assess relative air humidity.

The effect of the weather station elevation on the quality of the reanalysis climate data shows that for average air temperature, average relative air humidity and R_s, RMSE and MBE values were generally stable for elevation below 650 m a.s.l.. While for the stations with elevation above 650 m a.s.l. was possible to notice an increase of the two indices.

The *ETo* values estimated based on climate variables from ERA5-L database encourage to use of the reanalysis database to assess *ETo* in Sicily. In general, the results were in agreement with those obtained from ground measurement by 27 weather stations, with average RMSE equal to 0.73 mm d^{-1} and corresponding MBE equal to -0.36 mm d^{-1}. The best estimation performance of *ETo* (b= 0.99, R^2=0.96, RMSE =0.42 mm d^{-1} and MBE=0.00 mm d^{-1}), was obtained in Canicatti (ID 208) station where all climate variables were well estimated by the ERA5-L database. While the highest differences (b= 0.77, R^2=0.92, RMSE =1.26 mm d^{-1} and MBE=-1.03 mm d^{-}

[1]) were observed in Lentini (ID 292) station where the relative air humidity overestimation (b=1.25) and wind speed underestimation (b=0.65) cause the worst performance in *ETo* estimation.

The S_c referred to the six variables T_{min}, T_{max}, RH_{max}, RH_{min}, R_s and U_{10}, used in the PM equation were equal to 0.59, 0.06, -0.42, -0.41 0.33 and 0.27, respectively. It is possible conclude that the main contribution to *ETo* quality estimation derives from the accuracy of T_{max} and relative air humidity measurements.

The results obtained in this study can be useful to encourage the use of ERA5-L database in Sicily. Moreover, the sensitivity analysis allowed to identify, which instruments need accurate maintenance routines to ensure a good quality of the future estimation. The results also provide an approach for assess *ETo* in areas where climate data are not available and to replace eventual lack in the ground measurement.

The use of the GPR algorithm to fill gaps in the time series of daily actual evapotranspiration was investigated. In the first step, the best combination of mean, $m(x)$, and kernel covariance, $k(x,x')$, functions were identified considering all the input variables associated with the climate, soil water status as well as two VIs expressive of plant vigor and surface water status. In the second step, four additional variable combinations were also explored, to verify the performance of the estimation when limiting the number of input variables or considering only input variables freely downloadable from the web. The goodness of the proposed methodology is confirmed by the quite high NSE index, ranging between 0.74 and 0.88, and values of RMSE always lower or equal to 0.55 mm d^{-1}. Further validation of the proposed ML algorithm with the three variable combinations not including SWC was carried out in an olive orchard. The performance of the GPR model was confirmed by the values of RMSE always lower than 0.51 mm d^{-1} and values of NSE positive and ranging from 0.65 to 0.67. Therefore, the combined use of agrometeorological and RS data with a GPR model can represent an opportunity to estimate missing data in the daily ET_a time series. Furthermore, in the zone where ground data are not available, the use of ERA5-L agrometeorological archive and VIs retrieved from Sentinel-2 images or, in areas characterized by homogeneous soil and land use, from MODIS sensors can be considered a valid alternative to fill gaps in measured time series of daily actual evapotranspiration.

The application of the FAO56 Agro-Hydrological model, in the Villabate citrus orchard during three irrigation seasons (2018, 2019 and 2020), based

on the proposed non-linear relationship K_c(VIs), showed fairly good agreement between estimated and measured, SWC, and ET_a at field level. The predictions of daily SWC were very accurate, with RMSE equal to 0.01 $cm^3\ cm^{-3}$ and the absence of bias, as a consequence of the substantial agreement between the average SWC, measured in the root zone, and the corresponding ones simulated by the model.

The reliability of the proposed K_c(VIs) relationship is also confirmed by the high R^2 values, the b coefficient slightly higher than 1 and the always positive NSE. However, the negative values of PBIAS, obtained in the three years of simulation, indicate a weak tendency of simulated values to be higher than the ones observed. On the other hand, the simulated values of ET_a were characterized by RMSE equal to 0.57 and 0.40, MBE of -0.26 mm d^{-1} and -0.01 mm d^{-1} and PBIAS of 10.40 and 0.20 for 2019 and 2020, respectively. Even if the crop coefficients tabulated for the different stages of citrus crop growth, on average, were confirmed in this research, the possibility of using site-specific crop coefficients, accounting for local and time-variable conditions occurring in the field can contribute to improving the crop water requirement predictions and irrigation scheduling. Moreover, the proposed K_c(VIs) relationships, implemented in a GIS environment, can also contribute to driving the implementation of precision irrigation strategies accounting for the actual field spatial variability.

The FAO56 Agro-Hydrological model was also applied on 33 pilot farms located within the irrigation district 1A, during two irrigation seasons (2018 and 2019). This model allowed retrieving daily spatial distribution of SWC, ET_a, K_c and K_s.

With reference to the capabilities of the model to estimate spatial distribution of SWC and ET_a, the results show a good predictive property with values consistent with the thermo-pluviometric boundary conditions.

The comparison between daily measured and estimated irrigation depth for the 2018 irrigation season, showed that the main differences in the estimated values are concentrated at beginning of July, when the irrigation season starts while for the remaining season, the simulated values were lower than of the real amount distributed, allowing a significative water saving. Except for the 2019 irrigation season, the absence of rainfall events causes a regular slightly overestimation in the simulated irrigation depth. When considering the cumulative irrigation depth, the differences between simulated and measured seasonal values was for the 2018 3%, while for the 2019 was 17%. The latter value suggests that the model performance is strongly conditioned

by the presence of the rainfall events. Despite for the 2019, the difference was considerable; the proposed methodology can be improved in order to minimizes the effect due to the absence of the precipitation. These results highlight that the proposed model, with opportune improvements, can be a useful tool for supporting the decision in the management of the irrigation water resources.

6.1 Future research line

In this thesis the possibility to assess CWR, in two typical Mediterranean orchards, using proximal and remotely sensed data was widely analysed. However, some research questions are still open.

Despite, the accurate estimations of *ETo* were obtained considering the ERA5-L climate variables. In this research, the U_{10} from ERA5-L climate database was used. Further analysis could be useful to investigate the effect on *ETo* estimation due to the application of logarithmic profile suggested by Allen et al. (1998) to retrieve the wind speed, obtained from ERA5-L database, at 2 m above the soil. Moreover, additional research activity could be needed to consider the possibility of downscaling the climate variables acquired from ERA5-L reanalysis database, using elevation information retrieved from Digital Elevation Model (DEM) to consider the intra-pixel spatial variability.

The applicability of GPR algorithm to predict ET_a was tested in two typical orchards (olives and citrus) of the Mediterranean basin. Nevertheless, the applicability of the proposed algorithm and methods could be extended, to assess the performances in different climatic areas. Furthermore, future studies could assess the performance in ET_a estimations associated with the introduction, as an input variable, of high-resolution satellite-based soil moisture products.

The performances of the FAO56 Agro-Hydrological model to estimate CWR at different spatial scale should be also tested on other sparse crops systems, as vineyards. Moreover, for application over large scales (irrigation district) information regarding the spatialization of the crops root depth and the real irrigated surface are essential. In this future perspective, data fusion between *in-situ* measurements and accurate field information are necessary to improve the knowledge in this research field.

References

Aboukhaled, A., Alfaro, A., Smith, M., 1982. Los Lisimetros. Irrigation and Drainage Paper 39, FAO, Roma.

Alam, M.S., Lamb, D.W., Rahman, M.M., 2018. A refined method for rapidly determining the relationship between canopy NDVI and the pasture evapotranspiration coefficient. Comput Electron Agric 147, 12–17. https://doi.org/10.1016/j.compag.2018.02.008

Allen, R., Pereira, L., Raes, D., Smith, M., 1998. FAO irrigation and drainage paper No. 56. Food and Agriculture Organization of the United Nations, Rome, 26–40.

Allen, R.G., Pereira, L.S., 2009. Estimating crop coefficients from fraction of ground cover and height. Irrig Sci 28, 17–34. https://doi.org/10.1007/s00271-009-0182-z

Amin, E., Verrelst, J., Rivera-Caicedo, J.P., Pipia, L., Ruiz-Verdú, A., Moreno, J., 2021. Prototyping Sentinel-2 green LAI and brown LAI products for cropland monitoring. Remote Sens Environ 255. https://doi.org/10.1016/j.rse.2020.112168

Anderton, S., Latron, J., Gallart, F., 2002. Sensitivity analysis and multi-response, multi-criteria evaluation of a physically based distributed model. Hydrol Process 16, 333–353. https://doi.org/10.1002/hyp.336

Araújo, C.S.P. de, Silva, I.A.C. e., Ippolito, M., Almeida, C.D.G.C. de, 2022. Evaluation of air temperature estimated by ERA5-Land reanalysis using surface data in Pernambuco, Brazil. Environ Monit Assess 194. https://doi.org/10.1007/s10661-022-10047-2

Asrar, G., Fuchs, M., Kanemasu, E.T., Hatfield, J.L., 1984. Estimating Absorbed Photosynthetic Radiation and Leaf Area Index from Spectral Reflectance in Wheat 1. Agron J 76, 300–306. https://doi.org/10.2134/agronj1984.00021962007600020029x

Autovino, D., Minacapilli, M., Provenzano, G., 2016. Modelling bulk surface resistance by MODIS data and assessment of MOD16A2 evapotranspiration product in an irrigation district of Southern Italy.

Agric Water Manag 167, 86–94. https://doi.org/10.1016/j.agwat.2016.01.006

Awad-Allah, E., 2020. Indispensable Measuring Techniques for Water Relations of Plants and Soils: A Review. Open Journal of Soil Science 10, 616–630. https://doi.org/10.4236/ojss.2020.1012030

Ayars, J.E., Fulton, A., Taylor, B., 2015. Subsurface drip irrigation in California-Here to stay? Agric Water Manag 157, 39–47. https://doi.org/10.1016/j.agwat.2015.01.001

Bal, S.K., Wakchaure, G.C., Potekar, S., Choudhury, B.U., Choudhary, R.L., Sahoo, R.N., 2021. Spectral Signature-Based Water Stress Characterization and Prediction of Wheat Yield under Varied Irrigation and Plant Bio-regulator Management Practices. Journal of the Indian Society of Remote Sensing 49, 1427–1438. https://doi.org/10.1007/s12524-021-01325-6

Bausch, W.C., 1993. Soil background effects on reflectance-based crop coefficients for corn. Remote Sens Environ 46, 213–222. https://doi.org/https://doi.org/10.1016/0034-4257(93)90096-G

Begg' And, J.E., Turner, N.C., 1970. Water Potential Gradients in Field Tobacco The Connecticui Agricultural Experiment Station, Plant Physiol.

Bellido-jiménez, J.A., Gualda, J.E., García-marín, A.P., 2021. Assessing machine learning models for gap filling daily rainfall series in a semiarid region of spain. Atmosphere (Basel) 12. https://doi.org/10.3390/atmos12091158

Beven, K., 1979. A sensitivity analysis of the penman-monteith actual evapotranspiration estimates, Journal of Hydrology.

Bono, 1998. Carta dei suoli dell"area Castelvetrano est: Contrada Seggio e limitrofe. Regione Siciliana.

Boyer, M., Miller, J., Belanger, M., Hare, E., Wu, J., 1988. Senescence and spectral reflectance in leaves of northern pin oak (Quercus palustris Muenchh.). Remote Sens Environ 25, 71–87. https://doi.org/10.1016/0034-4257(88)90042-9

Braden, H., 1985. Ein Energiehaushalts- uind verdunstungsmodell fur wasser- und Stoffhaushaltsuntersuchungen landwirttschaftlich geutzter Einzugsgebiete. Mitteilungen Deutsche Bodenkundliche Gesellschaft 22:, 294–299.

Calera, A., Campos, I., Osann, A., D'Urso, G., Menenti, M., 2017. Remote sensing for crop water management: From ET modelling to services for the end users. Sensors (Switzerland). https://doi.org/10.3390/s17051104

Cammalleri, C., Ciraolo, G., Minacapilli, M., Rallo, G., 2013a. Evapotranspiration from an Olive Orchard using Remote Sensing-Based Dual Crop Coefficient Approach. Water Resources Management 27, 4877–4895. https://doi.org/10.1007/s11269-013-0444-7

Cammalleri, C., Rallo, G., Agnese, C., Ciraolo, G., Minacapilli, M., Provenzano, G., 2013b. Combined use of eddy covariance and sap flow techniques for partition of et fluxes and water stress assessment in an irrigated olive orchard. Agric Water Manag 120, 89–97. https://doi.org/10.1016/j.agwat.2012.10.003

Campos, I., Neale, C.M.U., Suyker, A.E., Arkebauer, T.J., Gonçalves, I.Z., 2017. Reflectance-based crop coefficients REDUX: For operational evapotranspiration estimates in the age of high producing hybrid varieties. Agric Water Manag 187, 140–153. https://doi.org/10.1016/j.agwat.2017.03.022

Carlson, T.N., Ripley, D.A., 1997. On the relation between NDVI, fractional vegetation cover, and leaf area index. Remote Sens Environ 62, 241–252. https://doi.org/10.1016/S0034-4257(97)00104-1

Carter, C., Liang, S., 2019. Evaluation of ten machine learning methods for estimating terrestrial evapotranspiration from remote sensing. International Journal of Applied Earth Observation and Geoinformation 78, 86–92. https://doi.org/10.1016/j.jag.2019.01.020

Castel, J., 2000. Water use of developing citrus canopies in valencia, spain, in: Proceeding International Society Citriculture. IX Congress 223–226.

Ceccato, P., Flasse, S., Tarantola, S., Jacquemoud, S., Grégoire, J.-M., 2001. Detecting vegetation leaf water content using reflectance in the optical domain.

Chalmers, D.J., Mitchell, P.D., van Heek, L., 1981. Control of Peach Tree Growth and Productivity by Regulated Water Supply, Tree Density, and Summer Pruning1, J. Amer. Soc. Hort. Sci.

Chen, S., He, C., Huang, Z., Xu, X., Jiang, T., He, Z., Liu, J., Su, B., Feng, H., Yu, Q., He, J., 2022. Using support vector machine to deal with the missing of solar radiation data in daily reference evapotranspiration estimation in China. Agric For Meteorol 316. https://doi.org/10.1016/j.agrformet.2022.108864

Choudhury, B., Ahmed, N., Idso, S., Reginato, R., Daughtry, C., 1994. Relations between evaporation coefficients and vegetation indices studied by model simulations. Remote Sens Environ 50, 1–17. https://doi.org/10.1016/0034-4257(94)90090-6

Clarke Topp, G., Ferré, P.A.T., 2002. 3.1 Water Content. pp. 417–545. https://doi.org/10.2136/sssabookser5.4.c19

Dainese, R., Lopes, B. de C.F.L., Fourcaud, T., Tarantino, A., 2022. Evaluation of instruments for monitoring the soil–plant continuum. Geomechanics for Energy and the Environment 30. https://doi.org/10.1016/j.gete.2021.100256

De Marinis, P., Manfron, G., Sali, C., Provolo, G., Facchi, A., Sali, G., 2019. Integrating remote sensing and census information for land securing in nord kivu, drc.

Ding, Y., Zhang, H., Li, Z., Xin, X., Zheng, X., Zhao, K., 2016. Comparison of fractional vegetation cover estimations using dimidiate pixel models and look-up table inversions of the PROSAIL model from Landsat 8 OLI data. J Appl Remote Sens 10, 036022. https://doi.org/10.1117/1.jrs.10.036022

Djaman, K., Balde, A.B., Sow, A., Muller, B., Irmak, S., N'Diaye, M.K., Manneh, B., Moukoumbi, Y.D., Futakuchi, K., Saito, K., 2015. Evaluation of sixteen reference evapotranspiration methods under

sahelian conditions in the Senegal River Valley. J Hydrol Reg Stud 3, 139–159. https://doi.org/10.1016/j.ejrh.2015.02.002

D'Urso, G., 2001. Simulation and management of on-demand irrigation systems: a combined agrohydrological and remote sensing approach. Wageningen University and Research.

Eisenhauer, J.G., 2003. Regression through the Origin. Teach Stat 25, 76–80. https://doi.org/10.1111/1467-9639.00136

El Hachimi, J., el Harti, A., Lhissou, R., Ouzemou, J.-E., Chakouri, M., Jellouli, A., 2022. Combination of Sentinel-2 Satellite Images and Meteorological Data for Crop Water Requirements Estimation in Intensive Agriculture. Agriculture 12, 1168. https://doi.org/10.3390/agriculture12081168

Er-Raki, S., Chehbouni, A., Guemouria, N., Ezzahar, J., Khabba, S., Boulet, G., Hanich, L., 2009. Citrus orchard evapotranspiration: Comparison between eddy covariance measurements and the FAO-56 approach estimates. Plant Biosyst 143, 201–208. https://doi.org/10.1080/11263500802709897

Er-Raki, S., Rodriguez, J.C., Garatuza-Payan, J., Watts, C.J., Chehbouni, A., 2013. Determination of crop evapotranspiration of table grapes in a semi-arid region of Northwest Mexico using multi-spectral vegetation index. Agric Water Manag 122, 12–19. https://doi.org/10.1016/j.agwat.2013.02.007

Estévez, J., Gavilán, P., Berengena, J., 2009. Sensitivity analysis of a penman-monteith type equation to estimate reference evapotranspiration in Southern Spain. Hydrol Process 23, 3342–3353. https://doi.org/10.1002/hyp.7439

Faraminan, A.M.G., Degano, M.F., Carmona, F., Rodriguez, P.O., 2021. Estimation of actual evapotranspiration using NASA-POWER data and Support Vector Machine, in 2021 19th Workshop on Information Processing and Control, RPIC 2021. Institute of Electrical and Electronics Engineers Inc. https://doi.org/10.1109/RPIC53795.2021.9648425

Foken Thomas and Aubinet, M. and L.R., 2012. The Eddy Covariance Method, in: Aubinet Marc and Vesala, T. and P.D. (Ed.), Eddy Covariance: A Practical Guide to Measurement and Data Analysis. Springer Netherlands, Dordrecht, pp. 1–19. https://doi.org/10.1007/978-94-007-2351-1_1

Franco, L., Giardina, G., Tuker, J., Motisi, A., Provenzano, G., 2022. Subsurface drip irrigation and ICT for the innovative irrigation water management: application to a citrus crop (*C. reticulata* 'Tardivo di Ciaculli'). Acta Hortic 453–460. https://doi.org/10.17660/ActaHortic.2022.1335.56

French, A.N., Hunsaker, D.J., Sanchez, C.A., Saber, M., Gonzalez, J.R., Anderson, R., 2020. Satellite-based NDVI crop coefficients and evapotranspiration with eddy covariance validation for multiple durum wheat fields in the US Southwest. Agric Water Manag 239. https://doi.org/10.1016/j.agwat.2020.106266

Gao, B.-C., 1996. Naval Research Laboratory, 4555 Overlook Ave, Remote Sens. Environ. ©Elsevier Science Inc.

Gavilán, P., Lorite, I.J., Tornero, S., Berengena, J., 2006. Regional calibration of Hargreaves equation for estimating reference et in a semiarid environment. Agric Water Manag 81, 257–281. https://doi.org/10.1016/j.agwat.2005.05.001

Gong, L., Xu, C. yu, Chen, D., Halldin, S., Chen, Y.D., 2006a. Sensitivity of the Penman-Monteith reference evapotranspiration to key climatic variables in the Changjiang (Yangtze River) basin. J Hydrol (Amst) 329, 620–629. https://doi.org/10.1016/j.jhydrol.2006.03.027

Gontia, N.K., Tiwari, K.N., 2010. Estimation of crop coefficient and evapotranspiration of wheat (Triticum aestivum) in an irrigation command using remote sensing and GIS. Water Resources Management 24, 1399–1414. https://doi.org/10.1007/s11269-009-9505-3

GonzÁlez-Altozano, P., Castel, J.R., 2000. Regulated deficit irrigation in 'Clementina de Nules' citrus trees. II: Vegetative growth. J Hortic Sci Biotechnol 75, 388–392. https://doi.org/10.1080/14620316.2000.11511256

Granata, F., 2019. Evapotranspiration evaluation models based on machine learning algorithms—A comparative study. Agric Water Manag 217, 303–315. https://doi.org/10.1016/j.agwat.2019.03.015

Granata, F., Gargano, R., de Marinis, G., 2020. Artificial intelligence based approaches to evaluate actual evapotranspiration in wetlands. Science of the Total Environment 703. https://doi.org/10.1016/j.scitotenv.2019.135653

Gutman, G., Ignatov, A., 1998. The derivation of the green vegetation fraction from NOAA/AVHRR data for use in numerical weather prediction models. Int J Remote Sens 19, 1533–1543. https://doi.org/10.1080/014311698215333

Huete, A.R., Liu, H., van Leeuwen, W.J.D., 1997. The Use of Vegetation Indices in Forested Regions: Issues of Linearity and Saturation.

IPCC, 2022. IPCC, 2022: Climate Change 2022: Impacts, Adaptation, and Vulnerability. Contribution of Working Group II to the Sixth Assessment Report of the Intergovernmental Panel on Climate Change. Cambridge, UK and New York, NY, USA. https://doi.org/10.1017/9781009325844.002

Ippolito, M., De Caro, D., Ciraolo, G., Minacapilli, M., Provenzano, G., 2022. Estimating crop coefficients and actual evapotranspiration in citrus orchards with sporadic cover weeds based on ground and remote sensing data. Irrig Sci. https://doi.org/10.1007/s00271-022-00829-4

ISTAT, 2014. 6° Censimento Generale dell'Agricoltura Utilizzo della risorsa idrica a fini irrigui in agricoltura.

Izadifar, Z., Elshorbagy, A., 2010. Prediction of hourly actual evapotranspiration using neural networks, genetic programming, and statistical models. Hydrol Process 24, 3413–3425. https://doi.org/10.1002/hyp.7771

Jacquemoud, Stéphane, Ustin, Susan L, Jacquemoud, S, Ustin, S L, 2003. Application of radiative transfer models to moisture content estimation and burned land mapping NASA TE View project Gulf Deepwater Horizon oil spill View project Application of radiative transfer models to moisture content estimation and burned land mapping.

Jain, P., Liu, W., Yao-Yun Chang, C., Melkonian, J., Rockwell, F.E., Pauli, D., Sun, Y., Zipfel, W.R., Holbrook, N.M., Riha, S.J., Gore, M.A., Stroock, A.D., 2021. A minimally disruptive method for measuring water potential in planta using hydrogel nanoreporters. PNAS. https://doi.org/10.1073/pnas.2008276118/-/DCSupplemental.y

Jensen, M.E., Burman, R.D., Allen, R.G., 1990. Evapotranspiration and irrigation water requirements: ASCE manual No. 70. New York, NY.

John A. Garnon, Hong-lie Qiu, 1999. Handbook of functional plant ecology. M. Dekker.

Jones, H.G., 2004. Irrigation scheduling: Advantages and pitfalls of plant-based methods, in: Journal of Experimental Botany. pp. 2427–2436. https://doi.org/10.1093/jxb/erh213

Jones, H.G., 1990. FEATURE Physiological Aspects of the Control of Water Status in Horticultural Crops, in: Plant-Environment Interactions from Subcellular to Plant Community. Davis, pp. 19–25.

Kamble, B., Kilic, A., Hubbard, K., 2013. Estimating crop coefficients using remote sensing-based vegetation index. Remote Sens (Basel) 5, 1588–1602. https://doi.org/10.3390/rs5041588

Kang, M., Ichii, K., Kim, J., Indrawati, Y.M., Park, J., Moon, M., Lim, J.H., Chun, J.H., 2019. New gap-filling strategies for long-period flux data gaps using a data-driven approach. Atmosphere (Basel) 10. https://doi.org/10.3390/atmos10100568

Kennedy, J., Neville, A., 1986. asic statistical methods for engineers and scientists, 3rd edn. ed. Harper and Row Publishers, New York.

Kim, N., Kim, K., Lee, S., Cho, J., Lee, Y., 2020. Retrieval of daily reference evapotranspiration for croplands in south korea using machine learning with satellite images and numerical weather prediction data. Remote Sens (Basel) 12, 1–22. https://doi.org/10.3390/rs12213642

Kljun, N., Calanca, P., Rotach, M.W., Schmid, H.P., 2015. A simple two-dimensional parameterisation for Flux Footprint Prediction (FFP). Geosci Model Dev 8, 3695–3713. https://doi.org/10.5194/gmd-8-3695-2015

Koide, R.T., Robichaux, R.H., Morse, S.R., Smith, C.M., 1989. Plant water status, hydraulic resistance and capacitance.

Koudahe, K., Djaman, K., Adewumi, J.K., 2018. Evaluation of the Penman–Monteith reference evapotranspiration under limited data and its sensitivity to key climatic variables under humid and semiarid conditions. Model Earth Syst Environ 4, 1239–1257. https://doi.org/10.1007/s40808-018-0497-y

Kriegler, F., Malila, W., Nalepka, R., Richardson, W., 1969. Preprocessing transformations and their effect on multispectral recognition., in: Proceedings of the 6th International Symposium on Remote Sensing of Environment. . University of Michigan, Ann Arbor, MI, pp. 97–131.

Kustas, W.P., Zhan, X., Jackson, T.J., 1999. Mapping surface energy flux partitioning at large scales with optical and microwave remote sensing data from Washita '92. Water Resour Res 35, 265–277. https://doi.org/10.1029/98WR02094

Lamm, F.R., O'Brien, D.M., Rogers, D.H., 2015. Economic comparison of subsurface drip and center pivot sprinkler irrigation using spreadsheet software. Appl Eng Agric 31, 929–936. https://doi.org/10.13031/aea.31.11253

Lechi Giovanmaria, 2001. Dispense del corso di telerilevamento.

Lei, H., Yang, D., 2014. Combining the Crop Coefficient of Winter Wheat and Summer Maize with a Remotely Sensed Vegetation Index for Estimating Evapotranspiration in the North China Plain. J Hydrol Eng 19, 243–251. https://doi.org/10.1061/(ASCE)HE.1943-5584.0000765

Liang, L., Li, L., Zhang, L., Li, J., Li, B., 2008. Sensitivity of Penman-Monteith reference crop evapotranspiration in Tao' er River Basin of northeastern China. Chin Geogr Sci 18, 340–347. https://doi.org/10.1007/s11769-008-0340-x

Ma, X., Lu, L., Ding, J., Zhang, F., He, B., 2021. Estimating fractional vegetation cover of row crops from high spatial resolution image. Remote Sens (Basel) 13. https://doi.org/10.3390/rs13193874

Main-Knorn, M., Pflug, B., Louis, J.M.B., Debaecker, V., Müller-Wilm, U., Gascon, F., 2017. Sen2Cor for Sentinel-2, in: Remote Sensing.

Masseroni, D., Corbari, C., Ceppi, A., Gandolfi, C., Mancini, M., 2013. Operative Use of Eddy Covariance Measurements: Are High Frequency Data Indispensable? Procedia Environ Sci 19, 293–302. https://doi.org/10.1016/j.proenv.2013.06.034

Mateos, L., González-Dugo, M.P., Testi, L., Villalobos, F.J., 2013. Monitoring evapotranspiration of irrigated crops using crop coefficients derived from time series of satellite images. I. Method validation. Agric Water Manag 125, 81–91. https://doi.org/10.1016/j.agwat.2012.11.005

McCuen, R.H., 1974. A sensitivity and error analysis cf procedures used for estimating evaporation. J Am Water Resour Assoc 10, 486–497. https://doi.org/10.1111/j.1752-1688.1974.tb00590.x

Minacapilli, M., Iovino, M., D'Urso, G., 2008. A distributed agro-hydrological model for irrigation water demand assessment. Agric Water Manag 95, 123–132. https://doi.org/10.1016/j.agwat.2007.09.008

Monteith, J.L., 1965. Evaporation and environment. Symp Soc Exp Biol 19, 205–34.

Montgomery, R.B., 1948. Vertical eddy flux of heat in the atmosphere. Journal of meteorology 5, 265–274.

Moriondo, M., Maselli, F., Bindi, M., 2007. A simple model of regional wheat yield based on NDVI data. European Journal of Agronomy 26, 266–274. https://doi.org/10.1016/j.eja.2006.10.007

Moroni, M., Lupo, E., Marra, E., Cenedese, A., 2013. Hyperspectral Image Analysis in Environmental Monitoring: Setup of a New Tunable Filter Platform. Procedia Environ Sci 19, 885–894. https://doi.org/10.1016/j.proenv.2013.06.098

Moroni, M., Porti, M., Piro, P., 2019. Design of a remote-controlled platform for green roof plants monitoring via hyperspectral sensors. Water (Switzerland) 11. https://doi.org/10.3390/w11071368

Mosre, J., Suárez, F., 2021. Actual evapotranspiration estimates in arid cold regions using machine learning algorithms with in situ and remote

sensing data. Water (Switzerland) 13. https://doi.org/10.3390/w13060870

Mosteller, F., Tukey, J.W., 1968. Data analysis, including statistics, in: Lindzey, G., Aronson, E. (Eds.), Handbook of Social Psychology, Vol. 2. Addison-Wesley.

Murphy, K.P., 2012. Machine Learning A Probabilistic Perspective.

Nagai, M., Chen, T., Shibasaki, R., Kumagai, H., Ahmed, A., 2009. UAV-borne 3-D mapping system by multisensor integration. IEEE Transactions on Geoscience and Remote Sensing 47, 701–708. https://doi.org/10.1109/TGRS.2008.2010314

Namasudra, S., Dhamodharavadhani, S., Rathipriya, R., 2021. Nonlinear Neural Network Based Forecasting Model for Predicting COVID-19 Cases. Neural Process Lett. https://doi.org/10.1007/s11063-021-10495-w

Nash, J.E., Sutcliffe, J.V., 1970. River flow forecasting through conceptual models part I — A discussion of principles. J Hydrol (Amst) 10, 282–290. https://doi.org/10.1016/0022-1694(70)90255-6

Neale, C.M.U., Bausch, W.C., Heermann, D.F., 1989. Development of reflectance-based crop coefficients for corn. Transactions of the American Society of Agricultural Engineers 32, 1891–1899.

Negm, A., Jabro, J., Provenzano, G., 2017. Assessing the suitability of American National Aeronautics and Space Administration (NASA) agro-climatology archive to predict daily meteorological variables and reference evapotranspiration in Sicily, Italy. Agric For Meteorol 244–245, 111–121. https://doi.org/10.1016/j.agrformet.2017.05.022

Newman, J.F., Klein, P.M., 2014. The impacts of atmospheric stability on the accuracy of wind speed extrapolation methods. Resources 3, 81–105. https://doi.org/10.3390/resources3010081

Nguyen, X.C., Nguyen, T.T.H., La, D.D., Kumar, G., Rene, E.R., Nguyen, D.D., Chang, S.W., Chung, W.J., Nguyen, X.H., Nguyen, V.K., 2021. Development of machine learning - based models to forecast solid waste generation in residential areas: A case study from Vietnam.

Resour Conserv Recycl 167. https://doi.org/10.1016/j.resconrec.2020.105381

Obukhov, A.M., 1951. Charakteristiki mikrostruktury vetra v prizemnom sloje atmosfery (Characteristics of the micro-structure of the wind in the surface layer of the atmosphere). Izv AN SSSR, Ser Geofiz 3, 49–68.

Palacios-Díaz, M.P., Mendoza-Grimón, V., Fernández-Vera, J.R., Rodríguez-Rodríguez, F., Tejedor-Junco, M.T., Hernández-Moreno, J.M., 2009. Subsurface drip irrigation and reclaimed water quality effects on phosphorus and salinity distribution and forage production. Agric Water Manag 96, 1659–1666. https://doi.org/10.1016/j.agwat.2009.06.021

Palani, S., Liong, S.Y., Tkalich, P., 2008. An ANN application for water quality forecasting. Mar Pollut Bull 56, 1586–1597. https://doi.org/10.1016/j.marpolbul.2008.05.021

Pan, Z., Hu, Y., Cao, B., 2017. Construction of smooth daily remote sensing time series data: a higher spatiotemporal resolution perspective. Open Geospatial Data, Software and Standards 2. https://doi.org/10.1186/s40965-017-0038-z

Paparoditis, N., Papelard, J.-P., Cannelle, B., Devaux, A., Soheilian, B., David, N., Houzay, E., 2012. Stereopolis ii: a multi-purpose and multi-sensor 3d mobile mapping system for street visualisation and 3d metrology. Revue Française de Photogrammétrie et de Télédétection 69–79.

Parker, W.S., 2016a. Reanalyses and observations: What's the Difference? Bull Am Meteorol Soc. https://doi.org/10.1175/BAMS-D-14-00226.1

Pelosi, A., Chirico, G.B., 2021. Regional assessment of daily reference evapotranspiration: Can ground observations be replaced by blending ERA5-Land meteorological reanalysis and CM-SAF satellite-based radiation data? Agric Water Manag 258. https://doi.org/10.1016/j.agwat.2021.107169

Pelosi, A., Terribile, F., D'Urso, G., Chirico, G.B., 2020. Comparison of ERA5-Land and UERRA MESCAN-SURFEX reanalysis data with

spatially interpolated weather observations for the regional assessment of reference evapotranspiration. Water (Switzerland) 12. https://doi.org/10.3390/W12061669

Penman, H.L., 1956. Estimating evaporation. Transactions, American Geophysical Union 37, 43. https://doi.org/10.1029/TR037i001p00043

Penman, H.L., 1948. Natural evaporation from open water, bare soil and grass. Proc R Soc Lond A Math Phys Sci 193, 120–145. https://doi.org/10.1098/rspa.1948.0037

Pereira, L.S., Allen, R.G., Smith, M., Raes, D., 2015. Crop evapotranspiration estimation with FAO56: Past and future. Agric Water Manag. https://doi.org/10.1016/j.agwat.2014.07.031

Pereira, L.S., Paredes, P., Melton, F., Johnson, L., Wang, T., López-Urrea, R., Cancela, J.J., Allen, R.G., 2020. Prediction of crop coefficients from fraction of ground cover and height. Background and validation using ground and remote sensing data. Agric Water Manag. https://doi.org/10.1016/j.agwat.2020.106197

Petropoulos, G., Kalaitzidis, C., 2012. Environmental science, engineering and technology ecological modeling.

Philip, J.R., 1957. The physical principles of soil water movement during the irrigation cycle. Proceedings 3rd Congress International Communications Irrigation Drainage 8: 125–154.

Pôças, I., Calera, A., Campos, I., Cunha, M., 2020. Remote sensing for estimating and mapping single and basal crop coefficientes: A review on spectral vegetation indices approaches. Agric Water Manag. https://doi.org/10.1016/j.agwat.2020.106081

Prueger, J.H., Hatfield, J.L., Kustas, W.P., Hipps, L.E., Macpherson, J.I., Neale, C.M.U., Eichinger, W.E., Cooper, D.I., Parkin, T.B., 2005. NOTES AND CORRESPONDENCE Tower and Aircraft Eddy Covariance Measurements of Water Vapor, Energy, and Carbon Dioxide Fluxes during SMACEX.

Puig-Sirera, À., Provenzano, G., González-Altozano, P., Intrigliolo, D.S., Rallo, G., 2021. Irrigation water saving strategies in Citrus orchards: Analysis of the combined effects of timing and severity of soil water

deficit. Agric Water Manag 248. https://doi.org/10.1016/j.agwat.2021.106773

Rallo, G., González-Altozano, P., Manzano-Juárez, J., Provenzano, G., 2017. Using field measurements and FAO-56 model to assess the eco-physiological response of citrus orchards under regulated deficit irrigation. Agric Water Manag 180, 136–147. https://doi.org/10.1016/j.agwat.2016.11.011

Rallo, G., Minacapilli, M., Ciraolo, G., Provenzano, G., 2014. Detecting crop water status in mature olive groves using vegetation spectral measurements. Biosyst Eng 128, 52–68. https://doi.org/10.1016/j.biosystemseng.2014.08.012

Rallo, G., Paço, T.A., Paredes, P., Puig-Sirera, Massai, R., Provenzano, G., Pereira, L.S., 2021. Updated single and dual crop coefficients for tree and vine fruit crops. Agric Water Manag. https://doi.org/10.1016/j.agwat.2020.106645

Rallo, G., Provenzano, G., 2013. Modelling eco-physiological response of table olive trees (Olea europaea L.) To soil water deficit conditions. Agric Water Manag 120, 79–88. https://doi.org/10.1016/j.agwat.2012.10.005

Rallo, G., Pumo, D., Provenzano, G., Ciraolo, G., Iovino, M., Agnese, C., Minacapilli, M., Cammalleri, C., Blanda, F., 2008. Sviluppi recenti e nuove tecnologie per la stima dei fabbisogni irrigui in ambiente mediterraneo.

Ranghetti, L., Boschetti, M., Nutini, F., Busetto, L., 2020. "sen2r": An R toolbox for automatically downloading and preprocessing Sentinel-2 satellite data. Comput Geosci 139. https://doi.org/10.1016/j.cageo.2020.104473

Rasmussen, C.Edward., Williams, C.K.I., 2006. Gaussian processes for machine learning. MIT Press.

Ravelli, F., Rota, P., 1999. Carte frequenziali mensili dell' evapotraspirazione di riferimento (ETo) e dei deficit idrici delle colture del Mezzogiorno d'Italia. Rivista di Irrigazione.

Reyes Rojas, L.A., Moletto-Lobos, I., Corradini, F., Mattar, C., Fuster, R., Escobar-Avaria, C., 2021. Determining actual evapotranspiration based on machine learning and sinusoidal approaches applied to thermal high-resolution remote sensing imagery in a semi-arid ecosystem. Remote Sens (Basel) 13. https://doi.org/10.3390/rs13204105

Ric Baret, F., Clevers, J.G.P.W., Steven, M.D., 1995. The Robustness of Canopy Gap Fraction Estimates from Red and Near-Infrared Reflectances: A Comparison of Approaches. Remote sensing of environmental 54, 141–151.

Robinson, D.A., Campbell, C.S., Hopmans, J.W., Hornbuckle, B.K., Jones, S.B., Knight, R., Ogden, F., Selker, J., Wendroth, O., 2008. Soil Moisture Measurement for Ecological and Hydrological Watershed-Scale Observatories: A Review. Vadose Zone Journal 7, 358–389. https://doi.org/10.2136/vzj2007.0143

Roth, K., Schulin, R., Flühler, H., Attinger, W., 1990. Calibration of time domain reflectometry for water content measurement using a composite dielectric approach. Water Resour Res 26, 2267–2273. https://doi.org/10.1029/WR026i010p02267

Rouse, R.W.H., Haas, J.A.W., Deering, D.W., 1974. Monitoring vegetation systems in the great plains with erts.

Rozenstein, O., Haymann, N., Kaplan, G., Tanny, J., 2018. Estimating cotton water consumption using a time series of Sentinel-2 imagery. Agric Water Manag 207, 44–52. https://doi.org/10.1016/j.agwat.2018.05.017

Saitta, D., Vanella, D., Ramírez-Cuesta, J.M., Longo-Minnolo, G., Ferlito, F., Consoli, S., 2020. Comparison of Orange Orchard Evapotranspiration by Eddy Covariance, Sap Flow, and FAO-56 Methods under Different Irrigation Strategies. Journal of Irrigation and Drainage Engineering 146. https://doi.org/10.1061/(asce)ir.1943-4774.0001479

Schaap, M.G., Leij, F.J., van Genuchten, M.T., Brown, G.E., 2001. rosetta: a computer program for estimating soil hydraulic parameters with hierarchical pedotransfer functions. J Hydrol (Amst) 251, 163–176.

Segovia-Cardozo, D.A., Franco, L., Provenzano, G., 2022. Detecting crop water requirement indicators in irrigated agroecosystems from soil water content profiles: An application for a citrus orchard. Science of the Total Environment 806. https://doi.org/10.1016/j.scitotenv.2021.150492

Sellers, P.J., 1987. Canopy reflectance, photosynthesis, and transpiration, II. The role of biophysics in the linearity of their interdependence. Remote Sens Environ 21, 143–183. https://doi.org/https://doi.org/10.1016/0034-4257(87)90051-4

Sentek, 2001. Sentek Drill & Drop Manual.

Sentelhas, P.C., Gillespie, T.J., Santos, E.A., 2010. Evaluation of FAO Penman-Monteith and alternative methods for estimating reference evapotranspiration with missing data in Southern Ontario, Canada. Agric Water Manag 97, 635–644. https://doi.org/10.1016/j.agwat.2009.12.001

Shu'itleworth, W.J., Wallace, J.S., 1985. Evaporation from sparse crops-an energy combination theory, Quart. I. R. Met. SOC.

Sims, D.A., Gamon, J.A., 2003. Estimation of vegetation water content and photosynthetic tissue area from spectral reflectance: a comparison of indices based on liquid water and chlorophyll absorption features. Remote Sens Environ 84, 526–537.

Swinbank, W.C., 1951. The measurement of vertical transfer of heat and water vapor by eddies in the lower armosphere. Journal of meteorology 8, 135–145.

Tanner, C.B., 1967. Measurement of evapotranspiration, in: Irrigation of Agricultural Lands. wiley, pp. 534–574. https://doi.org/10.2134/agronmonogr11.c30

Topp, G.C., Reynolds, W.D., 1998. Time domain re¯ectometry: a seminal technique for measuring mass and energy in soil. Soil Tillage Res 47, 125–132.

Tuccio, L., lo Piccolo, E., Battelli, R., Matteoli, S., Massai, R., Scalabrelli, G., Remorini, D., 2019. Physiological indicators to assess water status

in potted grapevine (Vitis vinifera L.). Sci Hortic 255, 8–13. https://doi.org/10.1016/j.scienta.2019.05.017

Turner, D.W., Thomas, D.S., 1998. Measurements of plant and soil water status and their association with leaf gas exchange in banana (Musa spp.): a laticiferous plant. Sci Hortic 77, 177–193.

UN DESA/POP, 2022. United Nations Department of Economic and Social Affairs, Population Division (2022). World Population Prospects 2022: Summary of Results. UN DESA/POP/2022/TR/NO. 3.

UNESCO, 2021. United Nations, The United Nations World Water Development Report 2021: Valuing Water. UNESCO, Paris.

Vanella, D., Longo-Minnolo, G., Belfiore, O.R., Ramírez-Cuesta, J.M., Pappalardo, S., Consoli, S., D'Urso, G., Chirico, G.B., Coppola, A., Comegna, A., Toscano, A., Quarta, R., Provenzano, G., Ippolito, M., Castagna, A., Gandolfi, C., 2022. Comparing the use of ERA5 reanalysis dataset and ground-based agrometeorological data under different climates and topography in Italy. J Hydrol Reg Stud 42. https://doi.org/10.1016/j.ejrh.2022.101182

Vismara, R., 1992. Ecologia Applicata, 2nd ed.

Walls, S., Binns, A.D., Levison, J., MacRitchie, S., 2020. Prediction of actual evapotranspiration by artificial neural network models using data from a Bowen ratio energy balance station. Neural Comput Appl 32, 14001–14018. https://doi.org/10.1007/s00521-020-04800-2

Walter C. Bausch, Christopher M. U. Neale, 1987. Crop Coefficients Derived from Reflected Canopy Radiation: A Concept. Transactions of the ASAE 30, 0703–0709. https://doi.org/10.13031/2013.30463

Wang, X., Gao, B., Wang, X.S., 2022. Investigating the ability of deep learning on actual evapotranspiration estimation in the scarcely observed region. J Hydrol (Amst) 607. https://doi.org/10.1016/j.jhydrol.2022.127506

Wang, X., Zhong, L., Ma, Y., Fu, Y., Han, C., Li, P., Wang, Z., Qi, Y., 2023. Estimation of hourly actual evapotranspiration over the Tibetan Plateau from multi-source data. Atmos Res 281. https://doi.org/10.1016/j.atmosres.2022.106475

Williams, E.L., Walter, L.M., Ku, T.C.W., Kling, G.W., Zak, D.R., 2003. Effects of CO2 and nutrient availability on mineral weathering in controlled tree growth experiments. Global Biogeochem Cycles 17. https://doi.org/10.1029/2002gb001925

Wilson, K., Goldstein, A., Falge, E., Aubinet, M., Baldocchi, D., Berbigier, P., Bernhofer, C., Ceulemans, R., Dolman, H., Field, C., Grelle, A., Ibrom, A., Law, B.E., Kowalski, A., Meyers, T., Moncrieff, J., Monson, R., Oechel, W., Tenhunen, J., Valentini, R., Verma, S., 2002. Energy balance closure at FLUXNET sites, Agricultural and Forest Meteorology.

Xue, J., Su, B., 2017. Significant remote sensing vegetation indices: A review of developments and applications. J Sens. https://doi.org/10.1155/2017/1353691

Zhai, Z., Martínez, J.F., Beltran, V., Martínez, N.L., 2020. Decision support systems for agriculture 4.0: Survey and challenges. Comput Electron Agric. https://doi.org/10.1016/j.compag.2020.105256

Zhang, C., Luo, G., Hellwich, O., Chen, C., Zhang, W., Xie, M., He, H., Shi, H., Wang, Y., 2021. A framework for estimating actual evapotranspiration at weather stations without flux observations by combining data from MODIS and flux towers through a machine learning approach. J Hydrol (Amst) 603, 127047. https://doi.org/10.1016/j.jhydrol.2021.127047

Zhang, S., Chen, H., Fu, Y., Niu, H., Yang, Y., Zhang, B., 2019. Fractional vegetation cover estimation of different vegetation types in the Qaidam Basin. Sustainability (Switzerland) 11. https://doi.org/10.3390/su11030864

Zhao, M., Heinsch, F.A., Nemani, R.R., Running, S.W., 2005. Improvements of the MODIS terrestrial gross and net primary production global data set. Remote Sens Environ 95, 164–176. https://doi.org/10.1016/j.rse.2004.12.011

Sitography

Agenziaentrate.gov, web site
https://www.agenziaentrate.gov.it

Atmosphere.copernicus.eu, web site
https://atmosphere.copernicus.eu/copernicus-moves-forward-monitoring-human-carbon-dioxide-emissions

Campbellsci.de, web site
https://www.campbellsci.de/wxpro

Cds.climate.copernicus.eu, ERA5 database web site
https://cds.climate.copernicus.eu/cdsapp#!/dataset/reanalysis-era5-single-levels?tab=overview

Cds.climate.copernicus.eu, ERA5-Land database, web site
https://cds.climate.copernicus.eu/cdsapp#!/dataset/reanalysis-era5-land?tab=overview

Cds.climate.copernicus.eu, web site
https://cds.climate.copernicus.eu/#!/home

Copernicus.eu, web site
https://www.copernicus.eu

Directory.eoportal.org, web site
https://directory.eoportal.org/web/eoportal/home

Esa.int, web site
https://www.esa.int/Applications/Observing_the_Earth/Copernicus/The_Sentinel_missions

Esa.int, web site
https://www.esa.int/Enabling_Support/Space_Transportation/Types_of_orbits

Esa.int, web site
https://www.esa.int/ESA_Multimedia/Images/2020/03/Geostationary_orbit

Ibis.geog.ubc.ca, web site
https://ibis.geog.ubc.ca/~achristn/infrastructure/oakridge.html

landsat.gsfc.nasa.gov, web site
https://landsat.gsfc.nasa.gov/article/preliminary-spectral-response-of-the-operational-land-imager-in-band-band-average-relative-spectral-response/

Scihub.copernicus.eu, web site
https://scihub.copernicus.eu/dhus/#/home

Sentektechnologies.com, website
https://sentektechnologies.com/products/soil-data-probes/

Sias.regione.sicilia.it, web site
http://www.sias.regione.sicilia.it/

Skyeinstruments.com, web site
https://www.skyeinstruments.com/digital-system/

Annexes

Annex 1: Daily average wind speed registered on ground at 2 m vs the corresponding at 10 m height

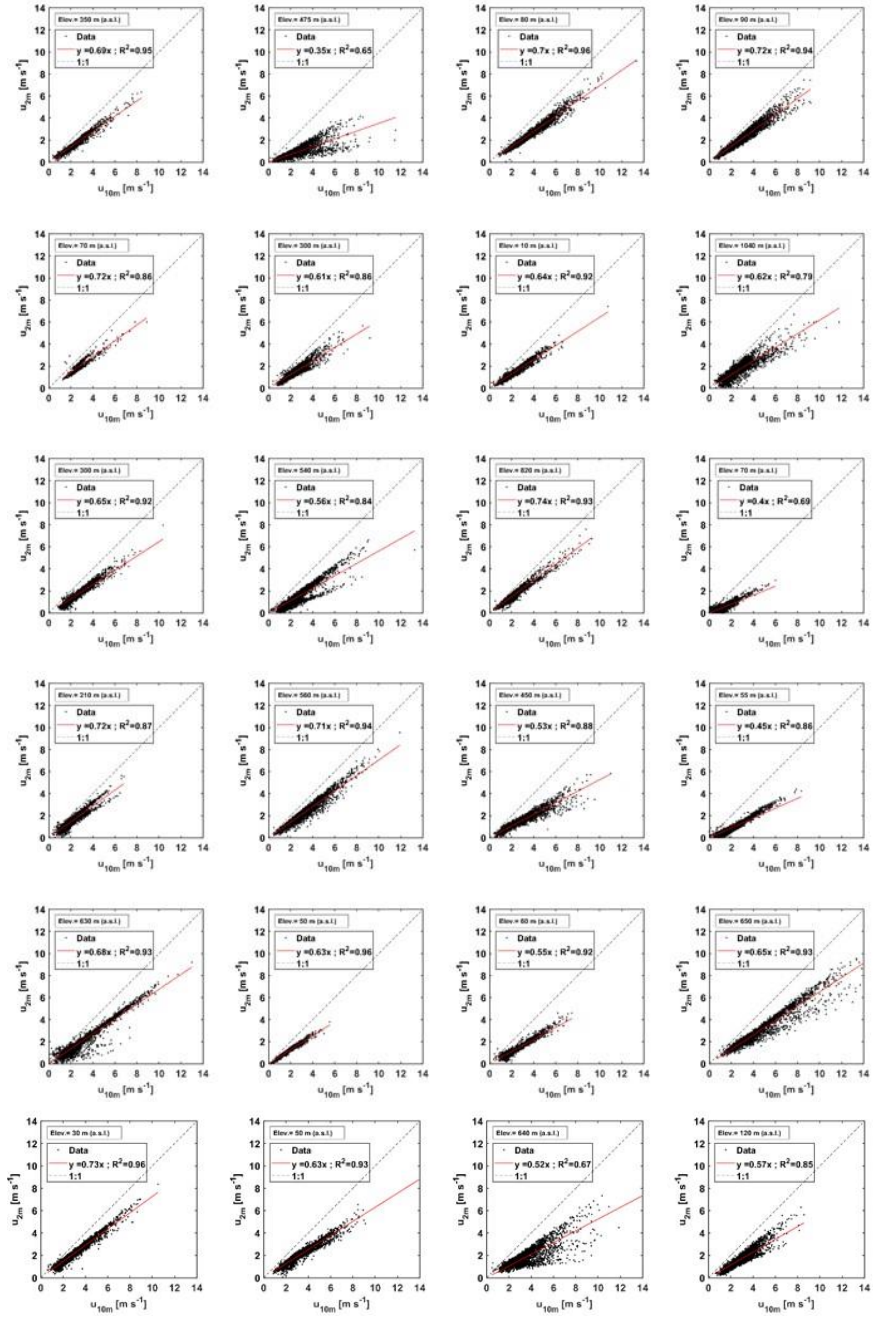

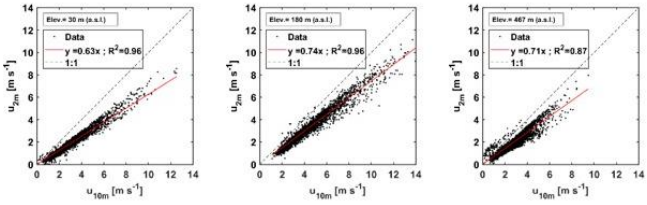

Annex 2: Pattern of RMSE and MBE values as a function of the elevation of the ground stations, for each examined variable

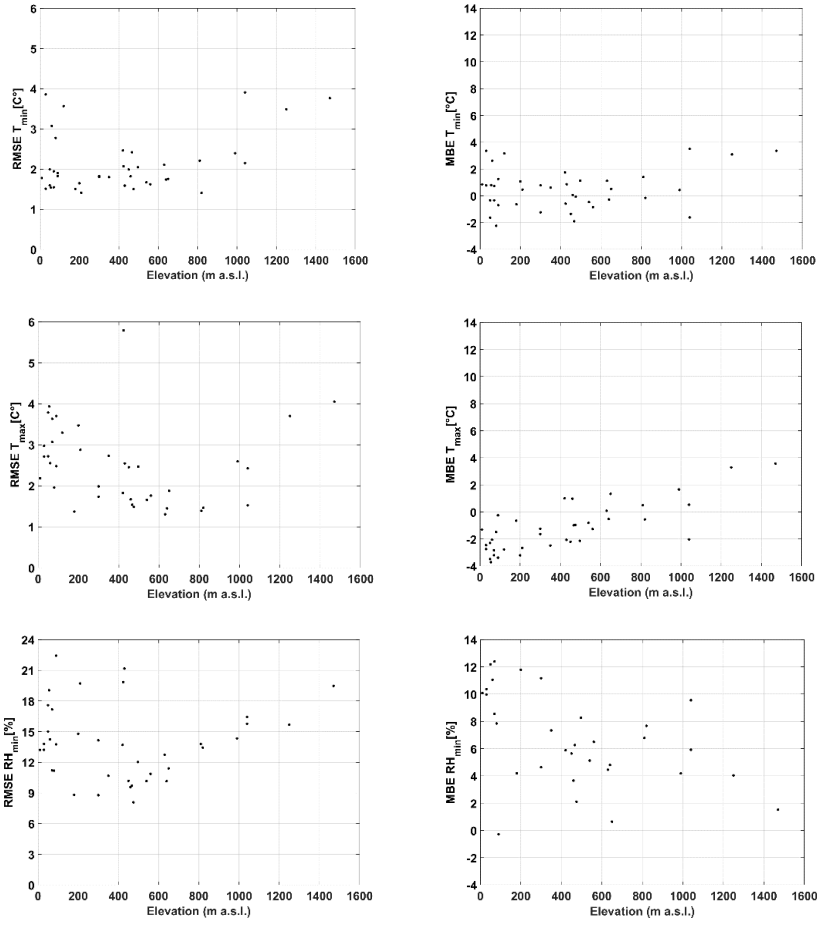

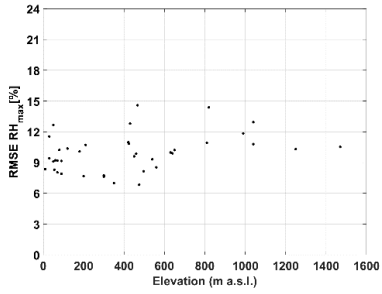
RMSE RH$_{max}$ [%]
Elevation (m a.s.l.)

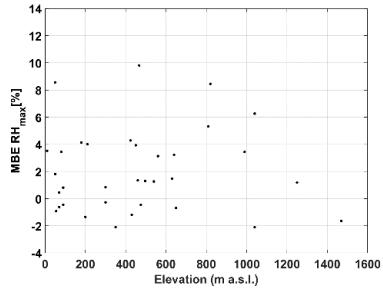
MBE RH$_{max}$ [%]
Elevation (m a.s.l.)

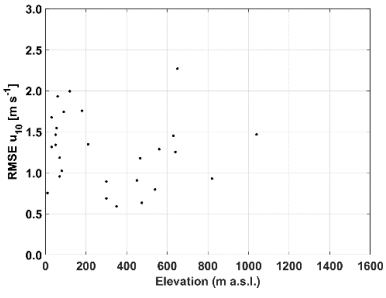
RMSE u$_{10}$ [m s^{-1}]
Elevation (m a.s.l.)

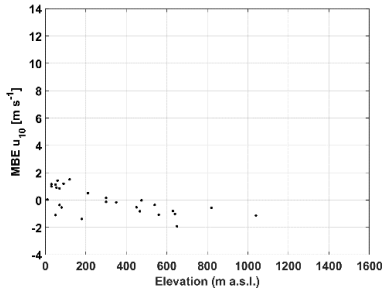
MBE u$_{10}$ [m s^{-1}]
Elevation (m a.s.l.)

Annex 3: Average values of slope regression line (b), sensitivity coefficient (S_{ci}), individual error (E_i) for the weather stations in which measurements of wind at 10 m above the ground are present.

	T_{min}			T_{max}			RH_{min}			RH_{max}			Rs			u_{10}		
ID	b	S_{vi} [-]	E_i	b	S_{vi} [-]	E_i	b	S_{vi} [-]	E_i	b	S_{vi} [-]	E_i	b	S_{vi} [-]	E_i	b	S_{vi} [-]	E_i
206	1.05	0.03	0.15	0.90	0.60	-6.21	1.12	-0.38	-4.42	0.98	-0.35	0.85	1.04	0.34	1.36	0.90	0.27	-2.72
208	1.00	0.04	0.00	0.96	0.58	-2.32	1.01	-0.48	-0.48	0.99	-0.43	0.43	1.04	0.35	1.40	0.92	0.25	-2.00
209	0.86	0.07	-0.95	0.95	0.66	-3.51	1.15	-0.40	-5.78	1.03	-0.45	-1.28	1.00	0.29	-0.05	0.84	0.31	-4.86
213	1.07	0.06	0.44	0.86	0.63	-9.11	1.37	-0.34	-12.61	1.00	-0.38	0.04	0.97	0.31	-0.84	1.33	0.30	9.95
216	1.02	0.04	0.08	0.89	0.69	-7.31	1.15	-0.35	-5.39	0.99	-0.35	0.44	1.02	0.32	0.54	0.87	0.31	-4.05
220	0.91	0.05	-0.43	0.95	0.61	-2.99	1.06	-0.39	-2.49	1.00	-0.39	-0.04	1.05	0.34	1.55	1.05	0.27	1.31
228	1.05	0.07	0.38	0.96	0.60	-2.67	1.20	-0.29	-5.72	1.03	-0.30	-1.05	1.00	0.34	-0.09	1.02	0.30	0.57
231	0.86	0.06	-0.76	0.89	0.45	-4.84	1.12	-0.43	-5.11	1.05	-0.44	-2.26	1.00	0.33	0.03	0.50	0.23	-11.59
232	1.05	0.04	0.21	0.93	0.62	-4.06	1.21	-0.35	-7.36	0.99	-0.37	0.32	1.00	0.32	0.10	0.96	0.29	-1.30
242	0.95	0.05	-0.22	0.96	0.56	-2.33	1.05	-0.46	-2.42	1.00	-0.45	-0.11	1.01	0.35	0.45	0.82	0.25	-4.52
246	0.99	0.05	-0.03	0.97	0.48	-1.38	1.09	-0.39	-3.56	1.08	-0.39	-2.97	1.03	0.34	0.89	0.68	0.24	-7.67
257	0.99	0.08	-0.11	0.88	0.52	-6.43	1.23	-0.22	-5.16	1.00	-0.24	0.09	1.03	0.42	1.43	1.54	0.23	12.31
258	1.03	0.09	0.25	0.88	0.53	-6.17	1.35	-0.30	-10.37	1.03	-0.34	-1.12	1.03	0.34	1.12	1.25	0.29	7.39
262	0.95	0.05	-0.24	0.94	0.58	-3.30	1.10	-0.46	-4.45	1.03	-0.47	-1.29	1.03	0.30	1.03	0.63	0.27	-10.00
268	0.91	0.06	-0.48	0.91	0.57	-5.31	1.09	-0.45	-4.19	1.03	-0.46	-1.59	1.02	0.33	0.74	0.76	0.26	-6.27
271	1.05	0.08	0.40	0.85	0.58	-8.84	1.32	-0.30	-9.66	0.98	-0.33	0.52	1.03	0.35	1.16	1.41	0.28	11.60
275	1.09	0.05	0.48	1.00	0.55	0.13	1.04	-0.52	-1.96	1.01	-0.52	-0.33	1.04	0.33	1.49	0.66	0.24	-8.00
276	0.90	0.10	-1.00	0.87	0.51	-6.86	1.33	-0.20	-6.71	1.09	-0.24	-2.20	1.06	0.36	2.09	1.73	0.29	20.91
282	1.15	0.06	0.95	0.92	0.64	-5.32	1.17	-0.41	-7.18	0.93	-0.40	2.70	1.00	0.38	0.05	1.61	0.24	14.75
286	1.02	0.06	0.11	1.06	0.58	3.21	0.96	-0.92	4.12	0.98	-0.88	1.82	0.98	0.32	-0.65	0.56	0.19	-8.38
288	1.04	0.08	0.32	0.89	0.62	-6.99	1.16	-0.46	-7.33	0.95	-0.47	2.43	1.01	0.37	0.23	1.43	0.24	10.50
292	0.98	0.03	-0.06	0.92	0.68	-5.58	1.25	-0.36	-9.00	1.01	-0.40	-0.39	0.99	0.26	-0.26	0.65	0.34	-11.90
298	0.98	0.06	-0.14	0.97	0.57	-1.66	1.06	-0.53	-3.23	1.02	-0.53	-1.24	1.01	0.31	0.37	0.70	0.26	-7.95
302	1.20	0.04	0.84	0.87	0.65	-8.13	1.40	-0.36	-14.54	0.94	-0.39	2.27	1.00	0.30	-0.03	1.53	0.30	16.12
305	1.22	0.04	0.86	0.90	0.68	-6.99	1.14	-0.48	-6.93	0.90	-0.46	4.38	1.03	0.34	1.05	1.24	0.26	6.21
308	0.96	0.07	-0.27	0.98	0.64	-1.59	1.06	-0.52	-3.03	1.04	-0.55	-2.08	1.03	0.27	0.86	0.66	0.29	-10.08
312	0.87	0.06	-0.81	0.95	0.56	-2.54	1.10	-0.38	-3.70	1.10	-0.40	-3.84	1.01	0.29	0.24	0.66	0.30	-10.26

Annex 4: Statistical indicators for mean, *m(x)*, and kernel covariance, *k(x,x')*, functions obtained by considering the entire database which includes all the examined variables (combination 1).

		Covariance kernel functions k(x,x')				
	Mean function m(x)	Rational Quadratic	Squared Exponential	Matern 5/2	Matern 3/2	Exponential
RMSE [mm d^{-1}]	Zero	0.39	0.44	0.42	0.40	0.38
	Constant	0.40	0.45	0.43	0.42	0.39
	Linear	0.41	0.40	0.41	0.41	0.40
MAE [mm d^{-1}]	Zero	0.28	0.33	0.31	0.29	0.28
	Constant	0.29	0.32	0.31	0.30	0.28
	Linear	0.29	0.29	0.30	0.29	0.29
R^2 [-]	Zero	0.87	0.84	0.85	0.86	0.88
	Constant	0.86	0.83	0.84	0.85	0.87
	Linear	0.86	0.87	0.86	0.86	0.87
b [-]	Zero	0.98	0.97	0.97	0.98	0.98
	Constant	0.97	0.97	0.97	0.98	0.98
	Linear	0.97	0.98	0.98	0.98	0.98
NSE [-]	Zero	0.87	0.84	0.85	0.86	0.88
	Constant	0.86	0.83	0.84	0.85	0.87
	Linear	0.86	0.87	0.86	0.86	0.87

Annex 5: Temporal dynamics of simulated (black line), $ET_{a\text{-}sim}$, and measured (red dots), $ET_{a\text{-}meas}$,. The corresponding scatterplots of estimated versus measured *ETa* are also shown.

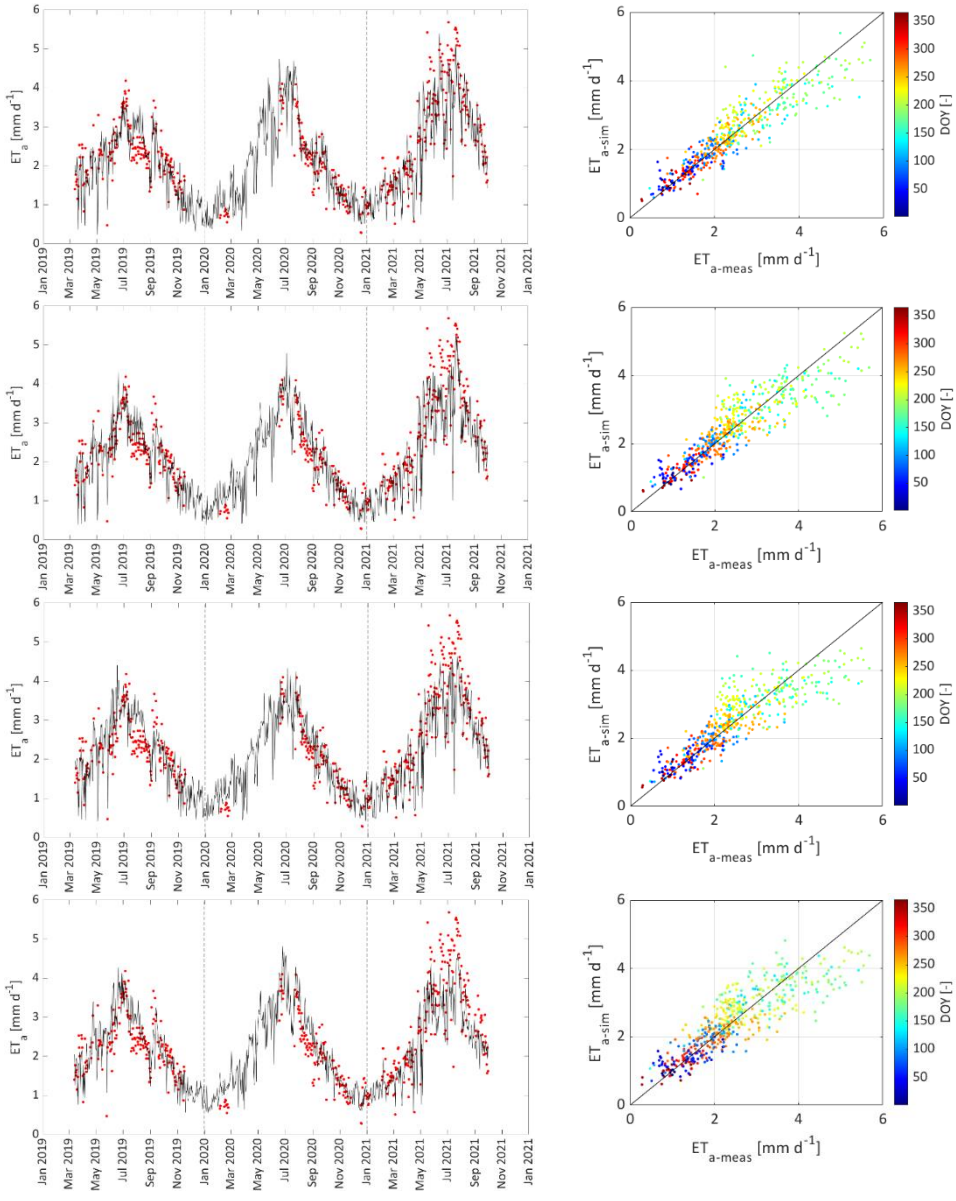

UNIVERSITA' DEGLI STUDI DI PALERMO

DIPARTIMENTO DI SCIENZE AGRARIE ALIMENTARI E FORESTALI

PALERMO
APRIL / 2023